Investigation of metal cluster production with the Matrix Assembly Cluster Source and chemical deposition of gold nanoparticles in porous silicon for optical studies

By

Thibaut Mathieu

Supervisor: **Dr. Andrey Kaplan**

Nanoscale Physics Research Laboratory
School of Physics and Astronomy
University of Birmingham

A thesis submitted to the University of Birmingham for the degree of
Doctor of Philosophy

November 2018

Abstract

The two main routes for the production of nanoparticles are the physical aggregation of single atoms in gas phase and the chemical reduction of colloidal solutions. In this thesis, we investigate a novel method in which metal clusters are formed from the sputtering of a cryogenic solidified gas loaded with metal atoms using the Matrix Assembly Cluster Source (MACS).

First of all, we address the possibility to modify the MACS, replacing the traditional argon matrix with dry ice at $20K$. The objective being the demonstration of the viability of the equipment when changing the physical nature of the matrix. The motivation for such a study lies in the fact that gases solidify at different temperatures and using CO_2 would open the path towards a cheaper and a more energy efficient cooling system. Using STEM images of the deposited silver clusters on TEM grids, we systematically study the size dependence of silver clusters as a function of both the metal loading in the CO_2 matrix and the energy of the sputtering beam used to extract them.

Second of all, a MACS2 system is built to welcome a new deposition chamber, which enables the deposition of clusters on a larger area. Silver, gold and binary gold-palladium clusters are produced with the MACS2 and deposited on pre-sputtered graphite tape. The top-most layers of the graphite tape are scrapped off and used in catalysis. We demonstrate that all samples show catalytic activity for the CO oxidation reaction.

Finally, gold nanoparticles are successfully embedded in porous silicon layers using electroless deposition in a tetrachloroauric acid solution as clusters produced through physical methods would saturate the surface and prevent the filling of the pores. Reflectometry measurements are used to determine the linear refractive index of the nanocomposites and estimate the amount of gold present in the layer with the $2D$ Maxwell-Garnett mixing approximation at a wavelength of $2.5\,\mu m$. Ultrafast time-resolved pump-probe spectroscopy measurements are also carried out on the samples, using a $800\,nm$ p-polarised pump and a $2.5\,\mu m$ s-polarised probe. Calculations based on the Drude model enable the quantification of the free carrier density in the porous silicon as a function of the pump intensity. An investigation into the nonlinear behaviour of the layers through varying the probe intensity demonstrates induced transparency and self focusing action of the light upon the medium. It has been found that samples containing gold display faster optical relaxation times and higher transient changes in reflectance.

Thesis structure

The first introductory chapter provides a general overview of the field of cluster production, a literature review on cluster sciences, alongside some theoretical background and experimental methods related to the production and characterisation of metal clusters. This will support the reader's understanding of the results developed in chapters 3 and 4, which are devoted to the production of clusters with the Matrix Assembly Cluster Source.

The second introductory chapter develops the theoretical background required for the final result chapter, which focuses on the linear and nonlinear optical properties of porous silicon layers embedded with gold nanoparticles in the near-infrared region.

As a variety of subjects are approached in this thesis, some experimental methods and more specific literature reviews are developed in the result chapters where they seem most in context, with the hope that it helps the reader to appreciate the scientific piece of research developed here.

Author's publications

Production of silver nanoclusters using a Matrix-Assembly Cluster Source with a solid CO2 matrix, Oiko V., Mathieu T., Cao L., Liu J. and Palmer R. The Journal of Chemical Physics, 145, 166101 (2016)

In preparation:

Linear and nonlinear response observed in porous silicon layers with embedded gold nanoparticles at $2.5\,\mu m$, Mathieu T., Wu R., Storey C., Canham L. and Kaplan A.

Acknowledgements

First, I thank the Leverhulme Trust and Prof. Martin Freer, Head of Physics and Astronomy, for their financial support and giving me the opportunity to study at the University of Birmingham. I particularly thank Dr. Ian Stevens who provided great moral support to me and others as a welfare tutor.

I especially thank Dr. Andrey Kaplan for giving me the chance to study the linear and nonlinear optical properties of nanomaterials, a field I have developed a growing interest for under his supervision. I also thank him for his constant availability, guidance and trust.

I thank Rihan Wu for her extreme sense of devotion to the laser system and to me. Her help throughout the entire project has been a great source of encouragement.

I thank Dr. Vitor Oiko for his supervision on the Matrix Assembly Cluster Source projects. His dedication and thoroughness to his work has been a source of inspiration. I thank Dr. William Terry for leading the design and construction of the Matrix Assembly Cluster Source 2 and introducing me to the opposite worlds of engineering equipments and nanoparticles.

I also thank Catherine Storey for teaching me the electroless deposition of gold; Prof. Leigh Canham for his help as second supervisor and his interesting feedbacks; Jack Collins for making the laser system efficiently computer-controlled; Dr. Dawn Forster and Dr. Jian Liu for their STEM work and Rongsheng Cai for his chemical work on my catalysts.

Last but not least, I thank my family, friends and colleagues for their constant support.

Table of contents

Chapter 1

Introduction to cluster science and the MACS

In this chapter, we give an experimental and theoretical introduction to the field of cluster science, from the discovery of magic numbers to key cluster applications. To describe agglomerate of atoms at the nanometric scale, we use the terms "cluster" and "nanoparticle". Clusters refer to well defined particles usually small enough to exhibit strong size-dependent properties, whereas nanoparticles refer to a wider range of size going from 1 to $100\,nm$. A review of clusters sources is given, putting the novel matrix assembly cluster source (MACS) thoroughly investigated in this work into context. Its design and modus operandi are detailed as well as some of important results previously achieved by colleagues. The two possible mechanisms of cluster formation in the matrix are introduced so that the reader can appreciate the working principle of the MACS and its ability to generate clusters. In order to quantify our study, it is crucial to know both the matrix composition and the cluster size distribution, which is why a brief description of the quartz crystal microbalance and the scanning transmission electron microscope is given.

1.1 Magic number clusters

The field of cluster science emerged in the early 80s with the discovery of nanoparticles showing "magic number" sizes[1]. The mass spectra of sodium clusters produced in a supersonic expansion showed peaks for clusters containing 8, 20, 40, 58 and 92 atoms, which suggests that these clusters are more likely to be formed or more stable than others. In fact, these peaks correspond to the closure of electronic shells specific to the clusters. In metallic clusters, valence electrons fill electronic shells and when all possible electronic states of a shell are occupied, the shell is closed and the cluster is at its most stable configuration. Hence, it is unlikely to gain or lose another atom, skewing the size distribution locally. In 1990, Martin et al. show the mass spectra of sodium clusters from a large range of sizes as seen in figure 1.1 [2]. The clusters were produced from a sodium vapour quenched in cold helium gas and were photoionised prior to entering the time of flight mass spectrometer. First of all, it should be mentioned that clusters with closed shells have higher ionisation energies than open shell clusters and therefore are expected to be less numerous going through the mass filter as many of them remain neutral. Hence, dips in the mass spectra correspond to magic number clusters. They observed that there is a period at which the magic clusters appeared and that it changes abruptly in the size region of around 1500 atoms. Whereas the sequence in smaller magic number clusters is due to the closure of electronic shells, the sequence in bigger magic number clusters appears to be due to a geometrical factor, i.e. the filling of atoms shells. For example, minima occurring in the mass spectra between 1500 to 22000 atom clusters correspond to either close-packed cuboctaedra or close-packed icosahedra. The crossover size from electronic shell dependence to atomic shell dependence is a function of both the material and the temperature [3]. The geometric factor was first predicted and observed for xenon clusters in 1981 by Echt et al., who showed that the mass spectrum of Xe clusters produced in gas phase exhibited peaks where icosahedra shells were completed [4]. We understand that, whereas a continuous range of energy states is available for electrons

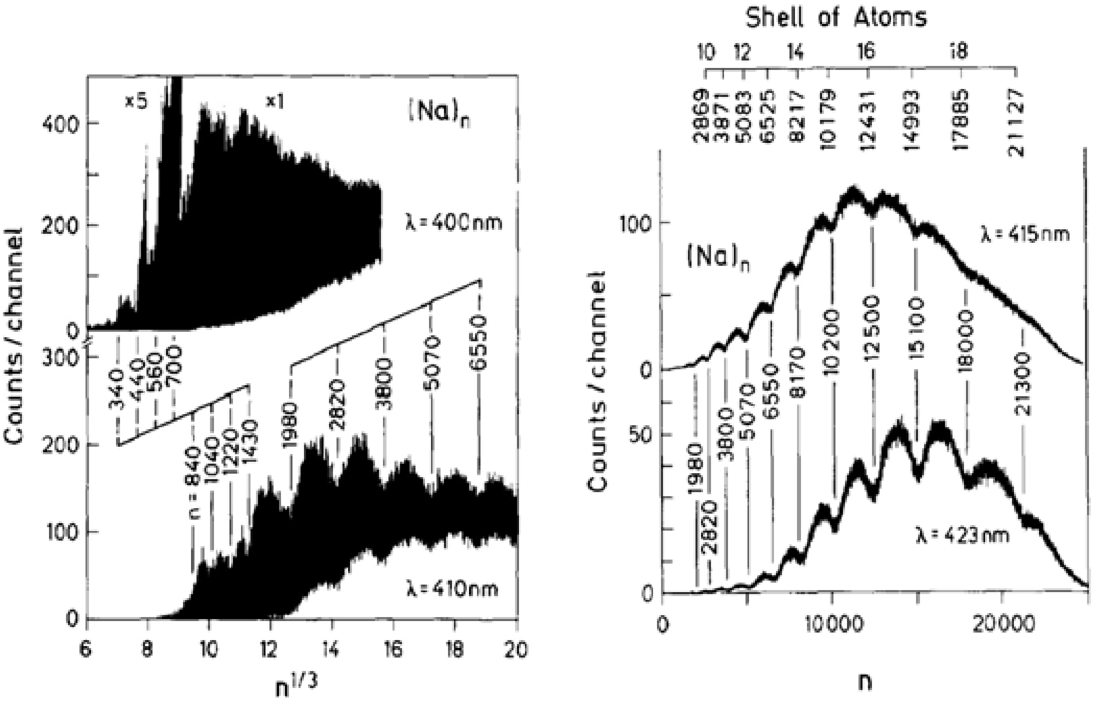

Fig. 1.1 Left: Mass spectra of Na clusters photoionized with 400nm and 410nm light. Two sequences of structure are observed at equally spaced intervals on the $n^{1/3}$ scale. Right: Averaged mass spectra of Na clusters photoionized with 415 and 423 nm light. Well defined minima occur at values of n corresponding to the total number of atoms in close-packed cuboctahedra and nearly close-packed icosahedra (listed at the top). Captions and figures reproduced from [2].

in the bulk structure, only a limited number of energy levels are available at a nanoscopic scale, similar to what happens in molecules. Thus clusters' electronic properties differ from that of both the bulk and the atom. This opens up a new dimension to the periodic table. The electronic properties of clusters are therefore size-dependent. For that reason, being able to filter clusters by their size (or their mass) became important, leading to various inventions such as the quadrupole mass selector and the time-of-flight mass filter [5].

Due to their tunable physical and chemical properties, shape and composition, applications for nanoparticles cover a vast spectrum of domains, such as medicine, environment, electronics, the food industry, cosmetics, catalysis, optical devices, etc. The latter two are discussed in this work.

1.2 Cluster catalysis

1.2.1 Pros and cons of the physical method

The main application for metal clusters produced in our laboratories is catalysis. In this context, we will be looking at metal clusters produced through physical methods, which offer two main advantages over those produced via colloidal routes: they do not have ligands and their size can be precisely tuned. The main drawback is that the quantities produced through physical methods are not enough for industrial applications and commercial use.

The atomic precision in cluster science is of great importance as explained in the previous section, and Heiz et al. [6] stressed it by demonstrating that CO oxidation activated by platinum clusters on thin MgO films is extremely size-dependent (see figure 1.2). We see that the number of CO_2 molecules catalytically produced triples when using Au_{15} instead of Au_{13} as catalysts. But, in the search for a perfect catalyst, many more parameters than the size must be considered, leading to an incredible amount of possible combinations of experimental conditions. An example of such a herculean work is given by Ellis et al. [7], who built a catalyst map for the 1-Pentyne hydrogenation of a variety of $PdSn$ and $PdTi$ catalysts deposited on alumina powder, varying the formation method, the metal ratio and the weight percentage of metal in the powder. They showed, as one can see in figure 1.3, that the best catalysts are the $PdTi$ clusters engineered with a cluster beam source, whereas other clusters produced via impregnation show either poor selectivity or poor conversation rate. They attributed the higher performance to the structure of the clusters as they form in flight in the vacuum chamber of the magnetron source, free from contaminations and ligands (see section 1.3.4 for details of the instrument). However, depending on what we want to achieve, ligands can either be desirable or not. For examples, to imitate enzymes, which are macromolecular catalysts existing in living organisms, bio-chemists could use ligands to limit the access to the active site solely to the appropriate molecules and emulate the desired reaction [8].

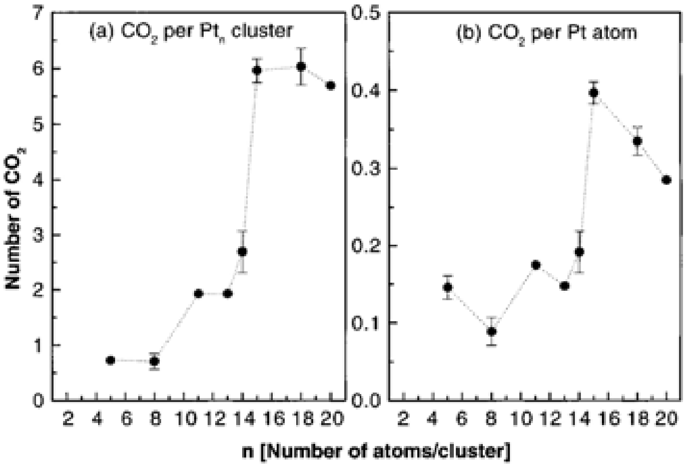

Fig. 1.2 (a) Total number of catalytically produced CO_2 molecules as a function of cluster size. (b) Total number of produced CO_2 molecules per atom as a function of cluster size. Caption and figure from [6].

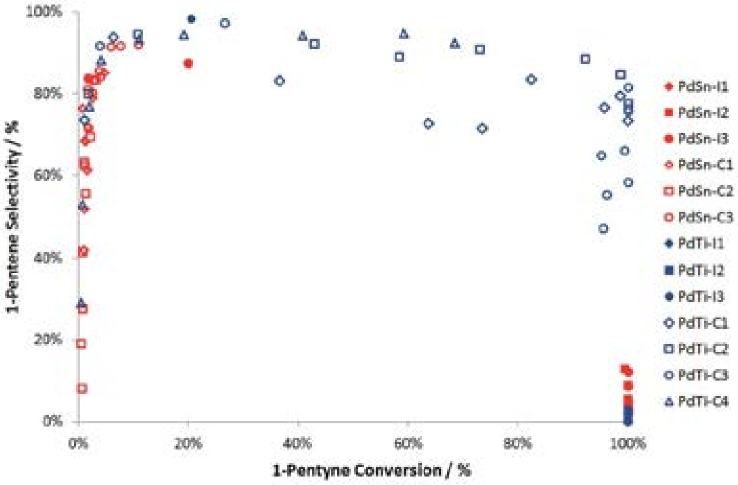

Fig. 1.3 Summary of 1-pentyne hydrogenation performance for *PdSn* and *PdTi* catalysts produced either via impregnation (I) or with a cluster beam source (C). The number following the letters I and C is the sample number and corresponds to its metal concentration (see Table 1 of [7] for specific values). Note that the data arises from experiments performed at a range of temperatures from room temperature to 250°C. The best catalysts are located on the top right corner of the graph as they have both good selectivity and conversion. Those were produced with a magnetron cluster source. Adapted caption and figure from [7].

1.2.2 The CO oxidation

CO oxidation is chosen in this work as a model catalytic reaction, which is most commonly applied to the transformation of the toxic carbon monoxide released by the motor of vehicles into CO_2. The reaction involves two reactants and one product and is written as: $CO + \frac{1}{2}O_2 \rightarrow CO_2$. Three mechanisms have been proposed to explain how and where the reaction takes place in the case of supported gold clusters [9].

- Although gold is expected to be quite inert, low-coordinated gold atoms present on the edges or corners of the nanoparticles are the centres for the adsorption of CO and O_2 molecules. These locations can act as the active catalyst sites, whether they are present on the surface of a cluster, randomly dispersed on a support in the form of single atoms, or defects at the surface of a gold film. This is valid regardless of the nature of the support. Theoretical studies suggest that gold particles are much more active than gold crystal surfaces due to their high step density. The steps are known to increase the binding energy between the reactants and the gold [10].

- Some supports induce change in the Au particle structure, increasing the number of sites or their quality. Moreover, the support can charge the particle. It was found that the partial transfer of an electron from the support plays an essential role in the activation of gold single atoms and subnanometric clusters [11].

- Gold nanoparticles supported on transition metal oxides[1] have their activity enhanced due to the ability of the support to provide reactive oxygen. More importantly, the high adsorption and surface mobility of the oxygen species on the support improves the transport of reactants to the catalyst sites located on Au clusters [12].

Gold nanoparticles deposited on inert supports and transition metal supports have shown interesting experimental catalytic activity [12]. The formers are not very active and their

---

[1] Compounds made of oxygen and metal atoms from the d-block of the periodic table.

activity is very size-dependent, vanishing rapidly for increasing diameter above $2\,nm$, whereas the latters still exhibit high catalytic activity for the CO oxidation for nanoparticles with a diameter of a few tens of nanometres. The reason is that small clusters have a higher dissociative adsorption of oxygen than bigger clusters due their higher step density. However, whereas many sites are being used for the dissociation of diatomic molecules of oxygen as this step cannot occur on the inert support, the transition metal supports act as a reservoir of oxygen atoms, freeing important active sites on the gold clusters for the oxidation of CO molecules to take place. The turnover frequency[2] over different Au/MeO_x catalysts has been extensively investigated for the CO oxidation [13]. The results of this study are shown in figure 1.4 and are differentiated by the ability of the support to dissociate oxygen molecules and supply them to the gold clusters. To stress the importance of the support, we report that the conversion rate in the catalytic CO oxidation reaction as a function of the temperature was previously studied for unsupported gold particles and gold particles on Al_2O_3 [14]. They show that whereas the reaction starts at around $100°C$ in the case of the supported particles, it only starts at around $290°C$ for the unsupported one. Ag nanoparticles on TiO_2 demonstrated activity at room temperature with increasing conversion rate as the concentration of particles goes up (up to 10%) [15].

Therefore, in the case of inert supports, the structure, the dimension and the shape of the metal clusters are of great importance in the quality of the catalytic response as they alone influence the yield of the reaction. Those geometrical aspects of the clusters have been studied both experimentally [16] [17] and theoretically [18] [19]. Theoretical studies have demonstrated that the planar Au_9 cluster ($< 1\,nm$ of diameter) is the optimal configuration for CO oxidation whereas Au_{79} (between $1-2\,nm$ of diameter) shows the best results in the case of a three-dimensional spherical cluster [20]. Smaller particles of Pd of $2.5\,nm$ diameter have also shown better results than those having 10 times their diameter, as the activation

---

[2] Definition: the turnover frequency quantifies the specific activity of a catalyst by the number of catalytic cycles occurring per second per site.

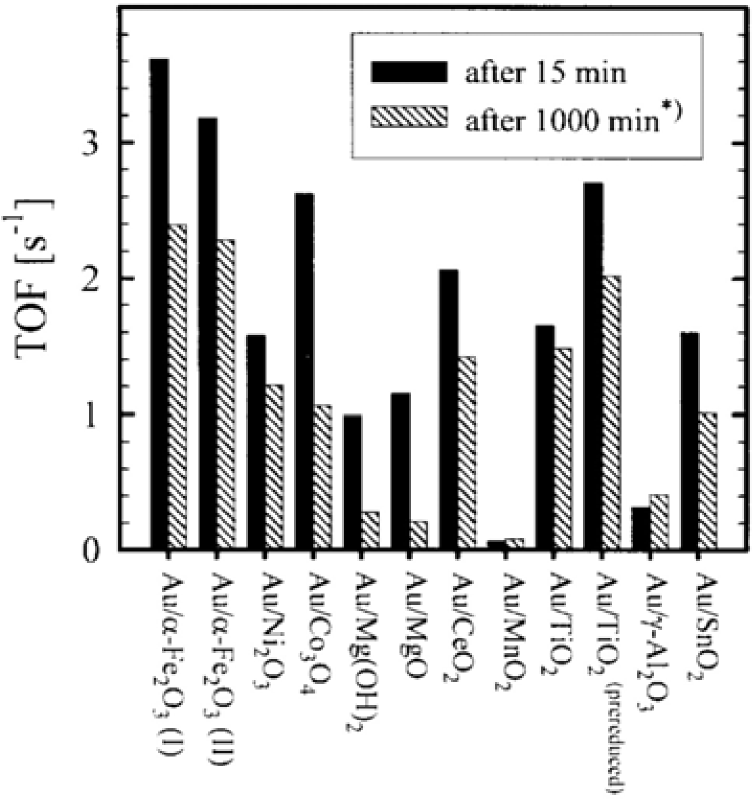

Fig. 1.4 Turnover frequencies over different Au/MeO_x catalysts after 15 minutes and 1000 minutes on stream. Caption and figure from [13].

energy is halved for the former [21]. Experimental studies on silver particles pre-treated with oxygen whose diameters vary between $4.5\,nm$ to $16.7\,nm$ on SiO_2 showed that the smaller nanoparticles are the best catalysts for CO oxidation at low temperatures, as they reach 100% conversion at $65°C$ [22].

1.3 Cluster sources

To put into context the novel cluster source developed in our laboratories and studied in this work, we first provide a description of the mechanism of some major cluster sources and discuss their specificities.

1.3.1 Seeded supersonic nozzle source

In a large furnace, metals are heated to high temperature in order to yield a metal vapour pressure in the range of $10-100\,mbar$. Due to the size of the oven, the maximum temperature achievable is $1600\,K$. This restricts its use to low melting point metals (e.g. alkali metals). A rare gas is also introduced in the furnace at a pressure of several bars. The hot mixture passes through a nozzle and expands in the vacuum (see figure 1.5). As it exits the nozzle, the metal vapour becomes colder and supersaturated. Therefore, it condenses and a clustering process occurs. While the mixture expands, dimers are formed as a result of three-body collisions between two metal atoms and one rare gas atom. The latter takes away the excess of vibrational energy and permits the two metal atoms to form a dimer [23]. Clusters can be formed with or without the rare gas. Whereas pure vapour jets lead to the formation of small clusters due to the contradictory role that the metallic atoms have to play by being both the cooling agent and the original material of the future particles, the introduction of a carrier rare gas boosts the production of bigger clusters by absorbing most of the heat generated at the collision. Experimental studies have shown that the heavier the rare gas, the higher the cluster production and the bigger the cluster [24]. In pure vapour jets some clusters have to lose one or several atoms in order to cool down and stabilise. In mixed phases where rare gas has a much higher density than that of the seeds, the seed-seed collisions cease before seed-rare gas ones. Therefore, in this case, the rare gas stabilises the clusters by taking away their extra vibrational energy. This source can produce 10^{16} clusters per second [25], although the material consumption is 10 times greater, which makes the waste significant. The clustering process occurs shortly after the nozzle where seed-seed collisions take place. The clusters produced are small with a size distribution from one to a hundred of atoms. Under very specific experimental conditions, such as larger amount of cooling gases and longer cooling distance, few thousands of atoms per clusters have been reported [26].

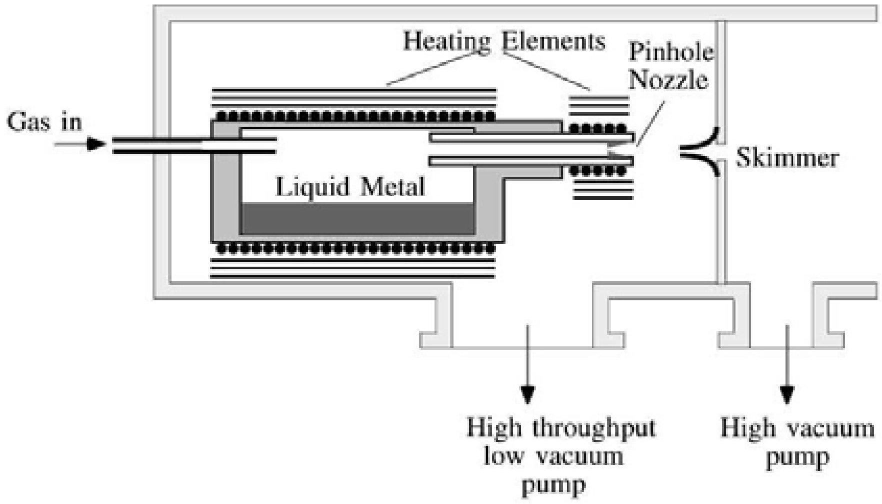

Fig. 1.5 Schematic of the seeded supersonic nozzle source. Figure from [27].

1.3.2 Gas-aggregation cluster source

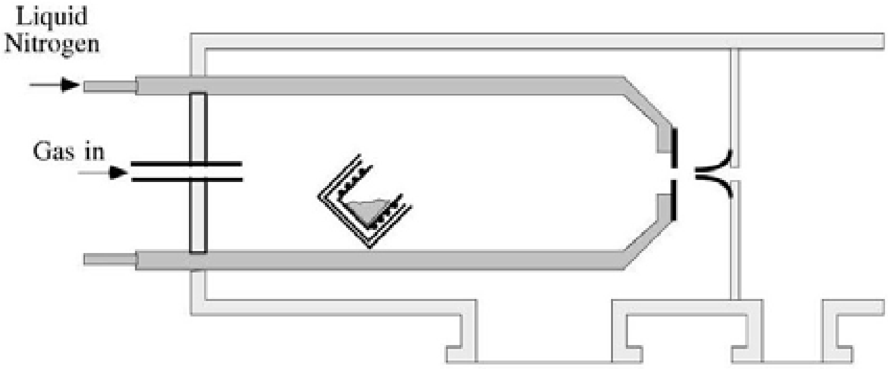

Fig. 1.6 Schematic of the gas-aggregation cluster source. Figure from [27].

A thermally isolated crucible releases a metal vapour into a flow of low-pressure inert helium gas (see figure 1.6). The mixture of hot metal vapour and cold helium gas in the condensation region exhibits a pressure that can reach up to $20 mbar$, which is significantly lower than reported in the seeded supersonic nozzle source. Therefore, the cluster production is much lower in this case. As soon as the hot metal vapour exits the crucible, the cold rare gas cools it down and clusters are formed by nucleation. In the case of gas-aggregation cluster source, the distance during which the cluster formation occurs is much greater than previously in the seeded supersonic cluster source where the cluster formation occurs at the exit of the nozzle and rapidly stops as the gas expands in the second chamber. Therefore, bigger clusters are formed in the present case. Sattler reported a systematic study of the production of Sb clusters. The bare Sb vapour exhibits clusters containing up to 4 atoms. Once the helium is introduced the abundance of clusters drops until it vanishes for a pressure of $0.5\,mbar$. While increasing the helium pressure above $5\,mbar$, the cluster beam rises greatly and also contains bigger clusters of around a few hundred atoms [28]. More recent studies report the use of a gas-aggregation cluster source coupled with first an ioniser and secondly a quadrupole mass filter. This has the advantage that it deposits clusters with a narrower size distribution. In this cluster source, the deposition chamber can be returned under ultra high vacuum in a few minutes post deposition [29]. Therefore, this technology is perfectly suited for in-situ studies.

1.3.3 Laser vaporisation cluster source

Whereas the two first sources discussed are continuous, the laser vaporisation cluster source is pulsed. First developed by Smalley in 1981, it consists of a laser light focused on a rod of the chosen material that will form the clusters further down in the process (see figure 1.7) [31]. The rod is mounted on a screw that rotates in order to present a fresh surface for each new laser pulse. These pulses extract vaporised material that spreads in a high-pressure flow of cold helium gas. The gas is injected in the chamber through a pulsed valve whose frequency is tuned with the laser. As in the gas aggregation cluster source, the gas cools down the metal vapour, which initiates the clustering process. Then the cluster growth continues while the mixture passes through a cold nozzle and expands as it does in the seeded supersonic nozzle source. Here the cluster formation process is a combination of both the sources previously discussed. Despite the fact that the cluster formation occurs by pulses, the amount of vaporised material is high enough for this source to compete with others due

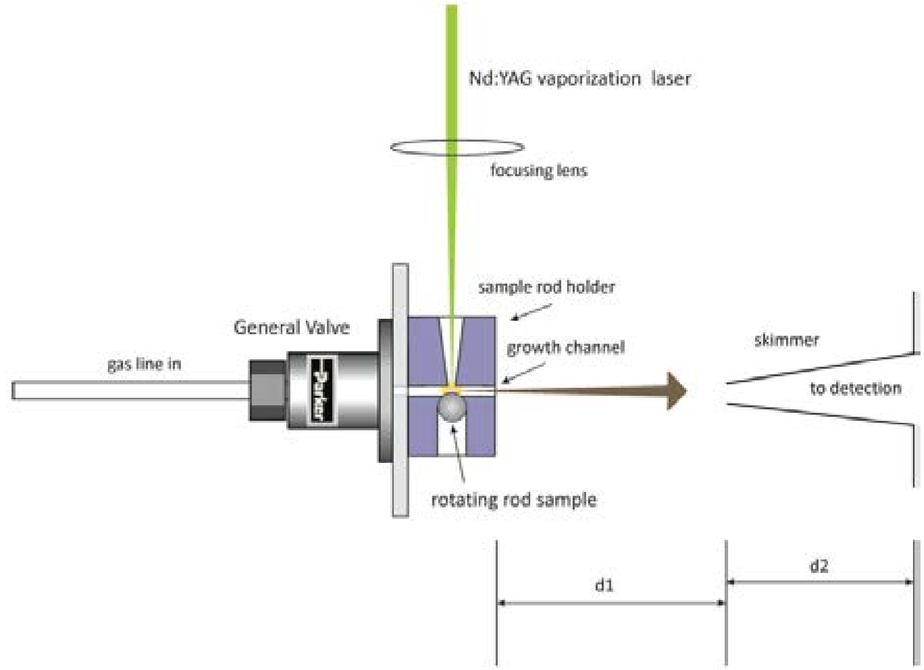

Fig. 1.7 Schematic of the laser vaporisation cluster source. Figure from [30].

to the high intensity of the laser. A cheaper alternative to the laser vaporisation cluster source but very similar in its design and in its working is the pulsed arc cluster ion source. Here the clusters are produced from the ablation due to spark discharges between metallic rods that act as electrodes. Although it produces a large quantity of clusters, the size distribution is wider in this case than other cluster sources. Around ten percent of the clusters are charged. Recent studies show that grams of metal nanoparticles per hour using laser ablation can be achieved. However, they have a large size distribution with an average cluster diameter of 30*nm* [32].

1.3.4 Magnetron sputtering source

In 1991, Haberland first reported the innovation of a new type of cluster ion source based on a magnetron sputter discharge combined with the gas aggregation technique discussed before [34]. Many years and technical improvements later, Pratontep et al. reported a detailed account of the magnetron sputtering source that we are using in our group as seen in figure

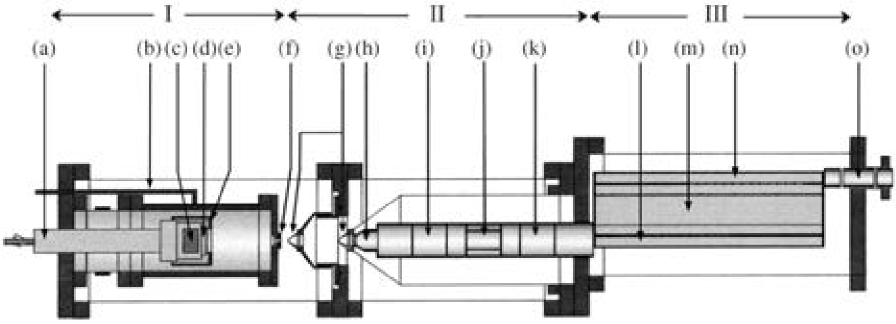

Fig. 1.8 Schematic of the experimental set-up for production of size-selected metal clusters. Clusters are produced in section I, shaped into a beam in section II and mass-selected prior to deposition in section III. Some of the key components are labelled: (a) magnetron axial mount; (b) liquid nitrogen (lN_2) cooling; (c) magnet; (d) metal target; (e) a grounded shield called the 'dark space shield' to confine the plasma in front of the target; (f) nozzle; (g) skimmers; (h) extraction lens; (i) lens; (j) deflection plates; (k) second einzel lens; (l) acceleration region; (m) field-free region; (n) deceleration region; (o) lens to focus the cluster beam for deposition into a high-vacuum chamber (not shown). Caption and figure from [33].

1.8 [35]. The cluster source is composed of three different sections. The formation of clusters takes place in the first chamber, liquid nitrogen cooled. A radio frequency (or DC) high voltage is applied to the target, which ignites argon gas in front of it. The argon plasma sputters the target made of the desired cluster material (for example Ag) and creates a dense vapour of atomic ions. Helium gas is introduced in the back of the chamber and induces the condensation of small clusters because it acts as the cooling agent of the three-body collision. Bigger clusters are formed through cluster-cluster collisions. The target is mounted at the end of a long movable arm, which allows control of the condensation length. For example, an increase of two to three centimetres in the condensation length gives birth to clusters about 20 percent heavier. The gas and cluster mixture exits through a nozzle, expands rapidly and condenses. In order to prevent large beam scattering, the gas jet passes through two skimmers that exhibit a particular conical shape. These skimmers extract the cluster beam and select its central portion before it enters in the next chamber, ensuring a relative uniform beam direction to optimise the mass selection process. Since about thirty percent of the cluster beam created by this method is ionized [34], clusters can be focused and accelerated without any further ionization. The second chamber is composed of lenses and plates with negative voltages that collimate the positive charged clusters. Then, the beam is size-selected by the lateral time-of-flight mass filter placed in the third chamber [5]. Once the cluster beam enters the mass filter, its initially horizontal trajectory is deviated by a pulsed electric field generated between the lower and upper plates. The perpendicular acceleration of each cluster is inversely proportional to its mass and therefore, by choosing the right vertical drifting time between the accelerating pulse occurring on the lower plate and the decelerating pulse from the upper plate, one can select the desired mass-range of clusters to exit the system. The kinetic energy of charged clusters can be tuned before deposition to allow implantation, pinning or soft-landing. In summary, the radio frequency power applied, the gas flow rates and pressures and the aggregation distance are all very important parameters that must be tuned carefully in order to reach optimal working conditions. Thanks to this system, it is possible to produce around $100\,pA$ of size-selected clusters spanning the range of a few atoms to several tens of thousands. Moreover, the advantage of working with differentially pumped sections is that the source can be connected to a deposition chamber kept in ultra-high vacuum, which can be useful for clean and accurate chemical and structural analysis [36].

1.4 The matrix assembly cluster source (MACS)

A precise description of the Matrix Assembly Cluster Source 1 (MACS 1) is given here as this instrument supports the work presented in chapter 3 and inspired the design of the MACS 2 described in chapter 4.

The MACS requires high level of purity and vacuum to function. In order to achieve ultra-high vacuum in the chamber (10^{-9} Torr to 10^{-11} Torr when baked), the system is equipped with two different pumps. First, a rotary vane pump traps air between its rotating elements and the wall of the cavity, and extracts it at each cycle. This enables the system to go from

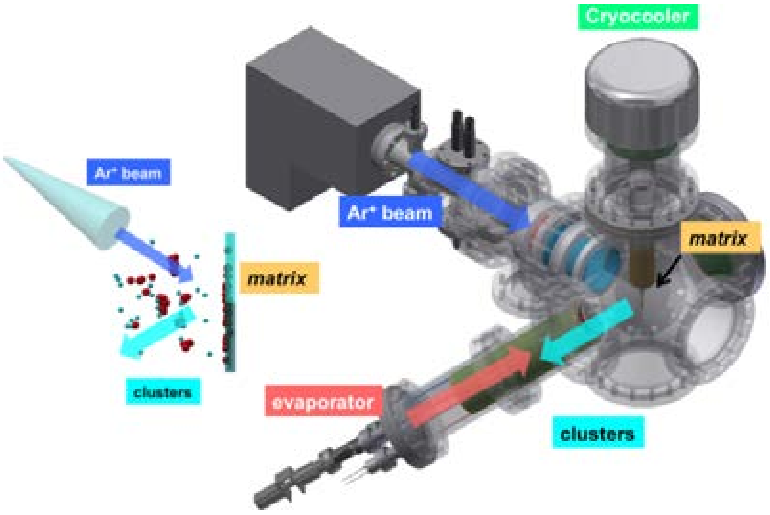

Fig. 1.9 The cluster source presented here is the matrix assembly cluster source one (MACS1) in reflection mode. (Picture from Lu Cao's thesis [37])

atmospheric pressure to around 10^{-2} Torr. Then a turbomolecular pump permits it to reach vacuum around 10^{-7} Torr to 10^{-10} Torr. This pump is made of a stack of metallic rotors each of them composed of angled blades oriented in such a direction that the gas molecules are given momentum towards the exhaust when they repeatedly collide the rotating blades. In order to quantify the quality of the vacuum, the chamber is equipped with an ionisation gauge that can read pressures below 10^{-3} Torr. Therefore, to avoid any damage or failure, this gauge can only be switched on once the turbomolecular pump is running at full speed. It is made of a heated filament that emits electrons encircled by a positively charged helical grid. The grid attracts these electrons, which gain kinetic energy and collide with the gas molecules present in the chamber. These collisions ionise the molecules. A negatively charged wire catches the generated cations, inducing a current that is proportional to the number of cations collected and therefore proportional to the amount of gas that composes the vacuum.

In the MACS1 shown on the figure 1.9, clusters are produced in the reflection mode. A transmission mode using a grid instead of a plain support for the matrix permits the collection of clusters in the original direction of the ion beam. The cluster formation occurs in two stages.

The first stage is the formation of the matrix. The matrix support is a one inch by one inch copper plate. It is cooled down to cryogenic temperatures by the means of a closed cycle cryocooler from Sumitomo Heavy Industries (SHI). The model CH-204 is composed of a compressor and a cooling head connected to each other by two transfer lines used for the supply and the return of the helium gas. The compressor delivers cold helium gas to the cooling head and pumps back the hot helium gas and compresses it again in a similar way to a refrigerator. Previous studies carried on the MACS 1 showed that this cooler can cool down the matrix support clamped on the head of the cryocooler to temperatures below $20K$ [38]. Once the matrix support temperature is stable, metal atoms are evaporated as some argon gas is introduced in the chamber through a leak valve. The pressure is measured via an ionisation gauge. Both the metal atoms and the rare gas stick to the copper plate and form a matrix. The metal atoms are therefore embedded in the rare gas solid. The metal is evaporated from a Createc high temperature effusion cell. It can go up to 2000 °C but is limited to 1600 °C due to the ceramic crucible that contains the metal. The cell is mounted inside a water cooled tube and monitored through a proportional-integral-derivative controller with $0.1K$ accuracy. The second stage consists of sputtering the matrix to generate and free the clusters out of the rare gas solid. The matrix support is insulated from the cooling head by a thin sapphire plate. This enables the operator to monitor the beam current that hits the matrix when sputtered with high energy argon ions. The ion source used in the MACS 1 is the ion sputter gun from Tectra that has a maximum output current of $4mA$. The working principle of this source is that microwaves with a $2.45GHz$ frequency generate a gas plasma. Ions are extracted from the plasma and accelerated to the desired energy (up to $5keV$) thanks to a series of charged apertures at different potential. The beam is then focused by a set of ion optics before it reaches the matrix. The voltages applied to each lens have been calibrated for different beam energies in previous studies [37] and these settings are kept the same in the frame of our research. The rotating deposition stage has twelve positions. Six of them host TEM grids where clusters are deposited and are separated by blank positions to avoid contamination between each experiment.

1.5 Previous achievements with the MACS

Studies led by Lu Cao and William Terry have been previously carried out on the MACS 1 using an argon matrix with embedded silver or gold atoms. They successfully demonstrated the possibility of forming metal clusters, deposited them on TEM grids and investigated both their structure and their size-distribution. Terry perfected the routine and, finding the ideal parameters to operate, showed that he could produce cluster beam currents reaching up to $100\,nA$, which is currently similar to non size-selected gas-aggregation magnetron sources, or 2 to 3 orders of magnitude higher when the clusters are size-selected [38]. Simultaneously generating clusters and replenishing the matrix while sputtering was proven to be possible over a period of $500\,s$. They showed that the size of the silver clusters collected in transmission mode increases with the doping of silver atoms in the matrix [39] as one can see on the figure 1.10. Mass spectra of clusters produced in reflection mode also showed a net increase in size as a function of the metal loading in the matrix using a time of flight mass filter [37], though mass-spectra are noisy due to the small fraction of charged clusters. Also, increasing the energy of the argon beam contributes to the production of bigger clusters (see figure 1.11), whereas increasing the temperature leads to the production of smaller clusters and narrower size distributions [37].

1.6 Cluster formation in solidified gas matrices

In the matrix assembly cluster source, the clusters are formed from the sputtering of a cryogenic matrix made of condensed argon or carbon dioxide loaded with metal atoms in small ratio. Their formation can occur through two different mechanisms.

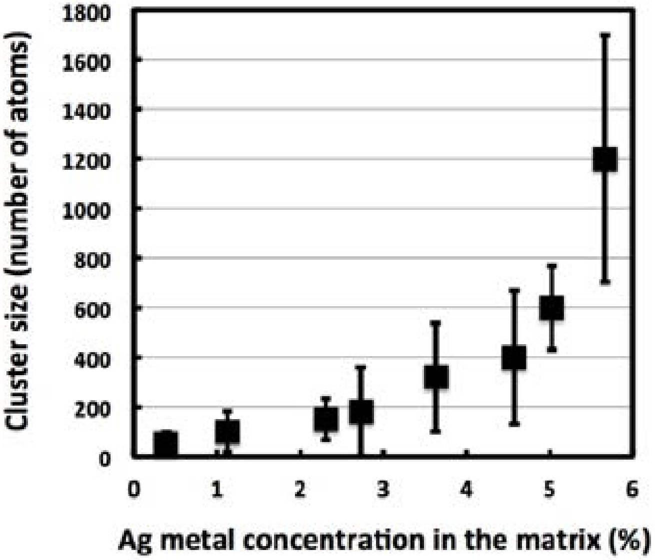

Fig. 1.10 Cluster size as a function of metal concentration in the matrix. The size of each cluster is measured from the integrated high angle annular dark field (HAADF) STEM intensity compared with that of single atoms. Error bars are the standard deviations of the size distributions (HAADF intensities). Caption and figure reproduced from [39].

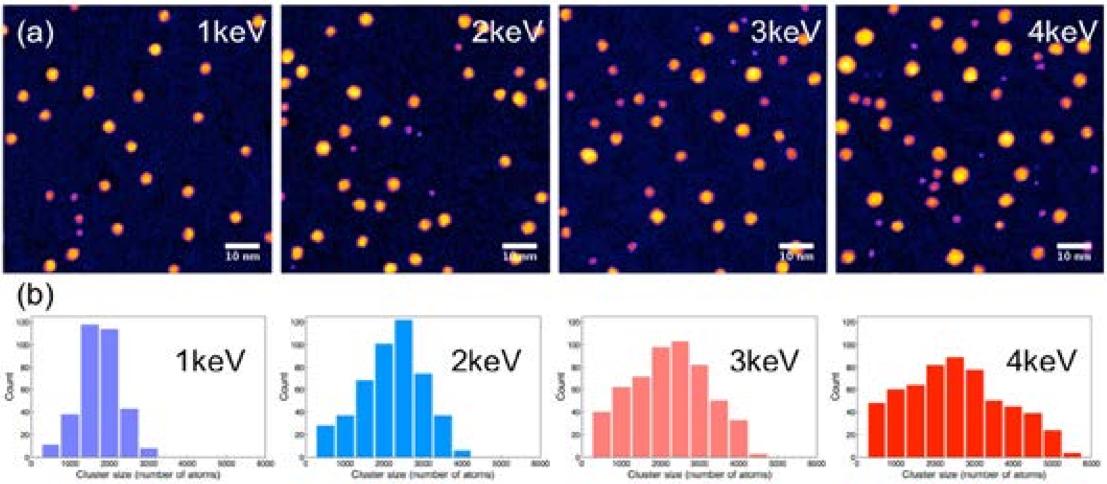

Fig. 1.11 HAADF STEM images (a) and respective size distribution diagrams (b) for four different incident beam energy. Figure reproduced from [37].

First, single metal atoms aggregate during matrix formation, co-condensed with the gas atoms or molecules onto the cold matrix support. Studies carried out on the deposition of gold atoms onto rare gas thin films show the formation of clusters around $2nm$, demonstrating the migration of atoms onto a rare gas film [40]. More interestingly, a study investigating light emission during the aggregation of silver clusters in rare gas matrices has demonstrated the migration and coalescence of silver clusters in matrices when these are warmed up but also at rest, pending that the temperature is high enough to allow a certain degree of mobility [41]. Figure 1.12 illustrates the existence of small dimers and trimers in the matrix in increasing numbers as the matrix warms up. As metal atoms are likely to migrate a few Å and aggregate to minimise their energy, small preformed metal clusters must exist in the matrix prior to argon ion bombardment, even more so as the concentration of metal is increased in the matrix. Secondly, the bombardment of the matrix with keV argon ions enhance the formation of bigger clusters and enables their extraction. As the ions hit the matrix, they transfer their kinetic energy to the system. Molecular dynamic simulations, which consider a keV argon ion hitting a frozen argon target, show that the energy transfer from the incident ion to the medium can be described in two successive modes [42] as one can see in figure 1.13. Basically, the bombarding ion collides with some atoms in the matrix, which in turn, collide with others leading eventually to a collision cascade. This knock on effect, however, isn't a linear exchange of kinetic energy between atoms. A local increase in pressure and temperature called a thermal spike is recorded, weakening the bonds between the argon atoms in the volume targeted. This leads to a flow of hot atoms into the vacuum and the formation of a big crater in the relaxing rare gas matrix. It has been shown that rare gas clusters in the range of $2-20$ atoms are sputtered out from the matrix through this process [43] but also that a large number of gas atoms or molecules are ejected per incident ion in both argon [44] and carbon dioxide [45] matrices supporting the thermal spike theory. As our matrix also contain metal atoms, an increase of temperature in the matrix would

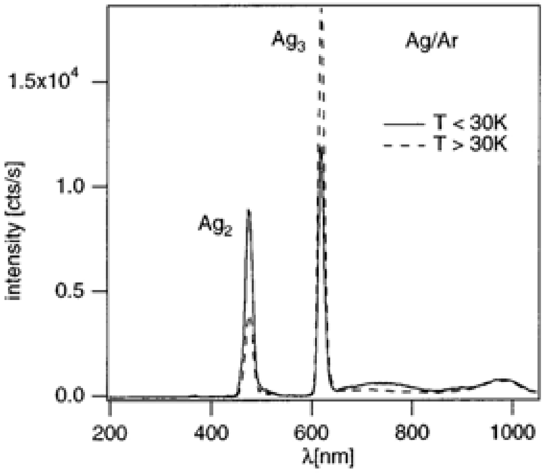

Fig. 1.12 Luminescence spectra during the condensation of silver atoms and dimers at matrix temperatures below and above 30 K. Caption and figure from [41].

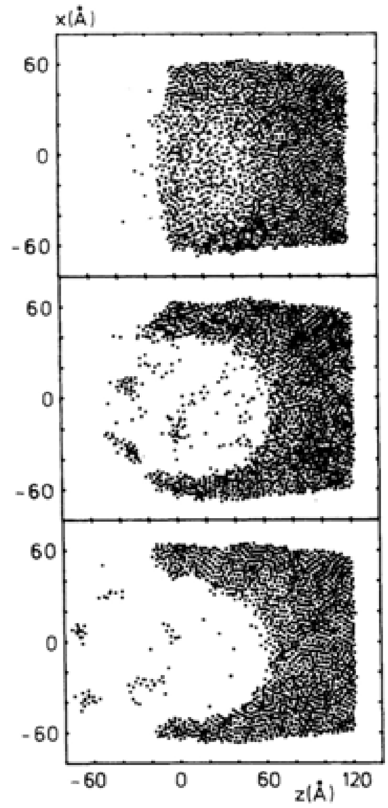

Fig. 1.13 Time evolution of an argon matrix hit by a $1keV$ Ar ion. From top to bottom: snapshots of the system are taken at $3.2ps$, $14.8ps$ and $24.7ps$ respectively after collision. Figure from [42].

promote the formation of bigger metal clusters as explained previously and the explosion-like phenomenon resulting from the thermal spike would participate to their ejection. Other evidence of the cluster formation happening solely in the matrix is shown alongside the experimental results later in the text.

1.7 Determination of the metal concentration in the matrix

In order to comprehend the link between the size distribution of clusters produced with the MACS and the composition of the matrix prior sputtering, the determination of the amount of metal embedded in the rare gas is of great importance. To do so, we show here how we estimate the number of atoms of rare gas (or CO_2 molecules) and the number of metal atoms there are per unit of volume, using the film thickness of the condensed gas and the mass of metal deposited over a certain period of time.

1.7.1 Thickness of the deposited film

A small quantity of gas introduced in a vacuum environment can be considered as an ideal gas, assuming that the major part of the energy is the kinetic energy of translation. Such a gas of pressure $P(Pa)$, contained in a volume $V(m^3)$ and made of N particles has a temperature $T(K)$ given by the perfect gas equation:

$$PV = NkT \Rightarrow \frac{N}{V} = \frac{P}{kT} \tag{1.1}$$

where k is the Boltzmann constant $1.38 \cdot 10^{-23} J/K$. Under these conditions, we must consider a Maxwell-Boltzmann speed distribution for the gas particles and determine the number of particles N_g hitting a matrix support per unit area and per unit time [46]. The average x-component velocity $< v_x >$ of particles moving in the positive direction is given by the following expression:

$$\begin{aligned} < v_x > &= \int_0^{+\infty} v_x \cdot f(v_x) dv_x \\ &= \int_0^{+\infty} v_x \cdot \sqrt{\frac{m}{2\pi kT}} \cdot \exp\left(\frac{mv_x^2}{2kT}\right) dv_x \\ &= \sqrt{\frac{kT}{2\pi m}} \end{aligned} \tag{1.2}$$

Therefore, particles that are within a distance $< v_x > \cdot \Delta t$ of the matrix support will hit it, i.e. particles that are included in the volume $A \cdot < v_x > \cdot \Delta t$ adjacent to the support. The number of gas particles N_g hitting a matrix support per unit area and per unit time is given by:

$$\begin{aligned} N_g &= \frac{N}{V} \cdot \frac{A \cdot < v_x > \cdot \Delta t}{A \cdot \Delta t} \\ &= \frac{P}{kT} \cdot \sqrt{\frac{kT}{2\pi m}} \\ &= P \sqrt{\frac{1}{2\pi kTm}} \end{aligned} \tag{1.3}$$

Here, we assume that the matrix support is cold enough so that all the particles that collide with it stick on it. Therefore, a film grows on it and its thickness can be determined. Indeed, knowing the lattice parameter and the crystal structure of the solidified gas permits the calculation of the volume of an atom of argon or a molecule of CO_2. In the following table 1.1, one reports the lattice parameter, the crystal structure and the volume of one particle V_p of both solid argon and dry ice. The film thickness per second is given by $(N_g \cdot V_p)^{1/3}$.

Gas	Structure	Lattice parameter (Å)	Volume of one particle $V_p(\text{Å}^3)$
Argon [47]	FCC	5.256	36.29
CO_2 [48]	Cubic	5.583	174.02

Table 1.1 This table shows the values for the lattice parameter for solid argon and dry ice (solid carbon dioxide). The crystal structure of solid argon is face-centred cubic whereas the dry ice is cubic.

1.7.2 Quartz crystal microbalance

The quartz crystal microbalances (QCM) used in this work are from MDC vacuum and Sycon Instruments. The working principle is the same in both cases and is described here. The quartz crystal (SiO_2) is placed so that it faces the evaporator. Once the shutter of the evaporator is open, the evaporated metal atoms build up at the surface of the quartz crystal, making a thin film. The QCM is computer-controlled and the software provided with the equipment gives the film thickness in real time, as metal atoms are deposited. In 1959, the equation 1.4 developed by Sauerbrey [49] links the mass increase Δm of such a film with the change in frequency of the sensor crystal $\Delta f = f_f - f_0$:

$$\Delta f = -\frac{2f_0^2}{A\sqrt{\rho_q \mu_q}} \cdot \Delta m \tag{1.4}$$

where A is the active area of the quartz crystal on to which the metal atoms are deposited, ρ_q is the density of the quartz and μ_q its shear modulus, which characterises its stiffness. This equation only applies under certains specific conditions as the film needs to be even and rigid and the change in frequency quite small. It is why a more general equation is used by Sycon where the film thickness Δs is obtained using the density of the material ρ_m and its Z-factor Z_f as expressed in the equation 1.5 [50]:

$$\Delta s = \frac{N_q \cdot \rho_q}{\pi \cdot \rho_m \cdot Z_f \cdot f_f} \cdot \arctan\left(Z_f \cdot \tan\left(\frac{\pi \cdot \Delta f}{f_f}\right)\right) \tag{1.5}$$

where N_q is the frequency constant for the crystal. The values for the density and Z-factor for the metals of interest in this work are listed in the table 1.2. The Z-factor is a parameter that depends of the shear modulus and the density of both the quartz and the material deposited. Using the bulk density is suggested as it provides sufficient accuracy. All the other constants are already implemented in the software as they are inherent to the quartz crystal provided by the company.

The number of metal atoms N_m per unit area and per unit time is given by:

$$N_m = \Delta s \cdot \left(\frac{N_A \cdot \rho_m}{A_w} \right) \tag{1.6}$$

where $N_A = 6.02 \cdot 10^{23} mol^{-1}$ is the Avogadro constant and represents the number of particles per mole.

Metal	A_w (g/mol)	ρ_m (g/cm^3) [50]	Z_f [50]
Silver	107.87	10.5	0.529
Gold	196.97	19.32	0.318
Palladium	106.42	12.02	0.357

Table 1.2 This table lists the atomic weight (A_w), the density (ρ_m) and the Z-factor (Z_f) for silver, gold and palladium.

1.7.3 Metal concentration

The metal concentration, which represents the proportion of metal atoms in the solidified gas matrix, is simply determined by the following relation:

$$Metal\ fraction = \frac{N_m}{N_m + N_g} \tag{1.7}$$

1.8 The scanning transmission electron microscope

In order to study the size and the structure of metal clusters, atomic resolution is required. Over the last 200 years, the performance of microscopes has gone up by almost five orders of magnitude, with an increasing resolution from tens of microns to the angstrom [51]. This was made possible by the invention of the electron microscope by Ruska in 1931. It is known that the resolution of a microscope is limited by diffraction effects and is proportional to the wavelength of the light used to probe the sample. The de Broglie's wavelength is given by $\lambda = \frac{hc}{pc}$ where $hc = 1240\ eV\,nm$, $pc = \sqrt{KE^2 + 2KE\, m_0\, c^2}$ and KE is the kinetic energy of the electrons. Accelerating electrons to $200\,keV$ reduces their wavelength to $\approx 2.5pm$. Due to presence of aberrations, the resolution of such a transmission microscope is in the order of 1 Å [52]. In this work, the clusters produced with the MACS and deposited on to TEM grids were analysed via high-angle annular dark field (HAADF) imaging under an aberration-corrected scanning transmission electron microscope (STEM). The model used in this work is the JEM-2100F (Jeol) and it was operated at $200\,kV$ with an HAADF detector inner collection angle of $62\,mrad$. A schematic of a typical STEM is presented on the figure 1.14. Its principle consists of focusing a high-energy electron beam to a small point and rastering the beam across a thin sample. Aberrations are corrected in various ways. We speak of spherical aberration when the electrons entering the edge of the lens are overfocused. Chromatic aberration happens when electrons of various energies are refracted differently when passing through the lenses and can be avoided using a more monochromatic electron gun. The transmitted beam is then either collected directly by a bright field detector or at high angles by a high angle annular dark field (HAADF) detector. Images presented in this work are taken with the HAADF detector, offering good Z-contrast for our analysis. Briefly, as the scattering of the electrons at high angle is a process dominated by Rutherford scattering,

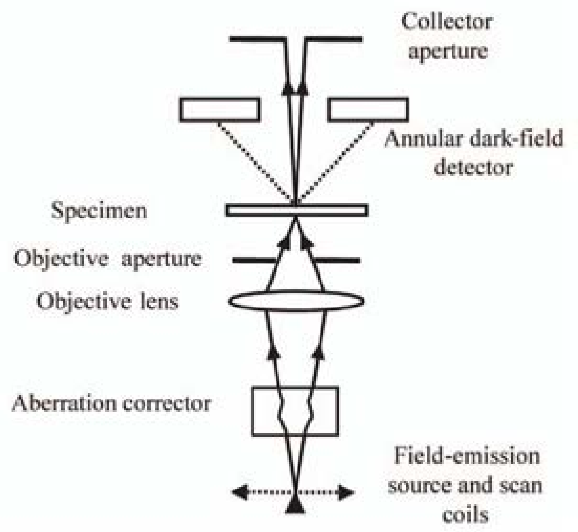

Fig. 1.14 Schematic of the STEM and its different elements. Figure from [51].

which describes the incoherent elastic scattering of the electrons with the nucleus of an atom, the intensity of the beam collected by the detector is proportional to the charge of the nuclei it encountered in the sample, and therefore proportional to its mass. The relation between the intensity I and the atomic number Z in an aberration-corrected $200\,keV$ microscope was reported by Wang and Palmer [53] and is given by $I = Z^{\alpha}$, with the exponent $\alpha = 1.46 \pm 0.18$ for an inner collection angle of 62 mrad. They reported that α can be around 1.8 when the inner collection angle is 103 mrad. Hence, in all cases, the metal atoms appear brighter than the support as they scatter more the incident beam than the carbon atoms making the support.

Chapter 2

Theoretical background for optical studies

Inspired by the work of his predecessors such as Gauss, Faraday and Ampere, Maxwell joined together a set of four equations and built the foundation of a theory capable of describing all classical electromagnetic phenomena [54]. Maxwell predicted the existence of electromagnetic waves and proposed that light is a type of electromagnetic radiation as seen in Appendix A. Based on this physical model, the behaviour of a polarised monochromatic beam incident upon a substrate or a thin film between two semi-infinite media is developed in this chapter and is of great importance when determining the refractive index of a material through reflectometry. However, when a medium is composed of materials of different nature, it is interesting to be able to describe the material's effective optical constants as a combination of the optical constants of each of its constituents. For that purpose, we introduce the Maxwell-Garnett mixing approximation theory. Using mixing rules allows the determination of the effective optical constant of the medium as a whole or, if the effective dielectric constant is known, it becomes possible to estimate the volume fraction of each of its constituents. When a light is shone upon a material, depending on its energy and intensity, linear and nonlinear optical behaviours can occur in the material and are discussed here.

In the linear case, as light excites electrons from the valence band to the conduction band, a population of free carriers is generated. This contributes to the change of the material's optical properties. In this context, the Drude model is introduced and relaxation processes are briefly listed to describe the material's response over time when the excitation has stopped. However, sometimes, linear equations cannot describe the optical behaviour of a material and perturbations need to be considered. In the last section of this chapter, second and third order nonlinear perturbations are added to the polarisation of the material and new optical constants are defined to characterise and quantify the nonlinear properties of the material.

2.1 Mathematical formalism for reflectometry

2.1.1 Principle

When light encounters matter, it can be reflected, refracted, absorbed, scattered and transmitted. Sometimes, a study of the reflected beam can provide sufficient information to characterise the material. The principle of reflectometry consists of the measurement of a polarised monochromatic light before and after its reflection onto a sample. The ratio between the reflected light intensity and the incident light intensity is called the reflectance. Once measured at various incident angles, the reflectance of the sample is used to determine physical properties such as refractive index and thickness.

2.1.2 Mathematical treatment considering one interface

Light can be seen as an electromagnetic wave obeying Maxwell's set of equations and boundaries conditions when passing through the interface between two media. Indeed the tangential component of both the electric field $\vec{E}$ and the magnetic field $\vec{H}$ must be continuous across the surface in the absence of surface current (see Appendix B) [56]. These equations

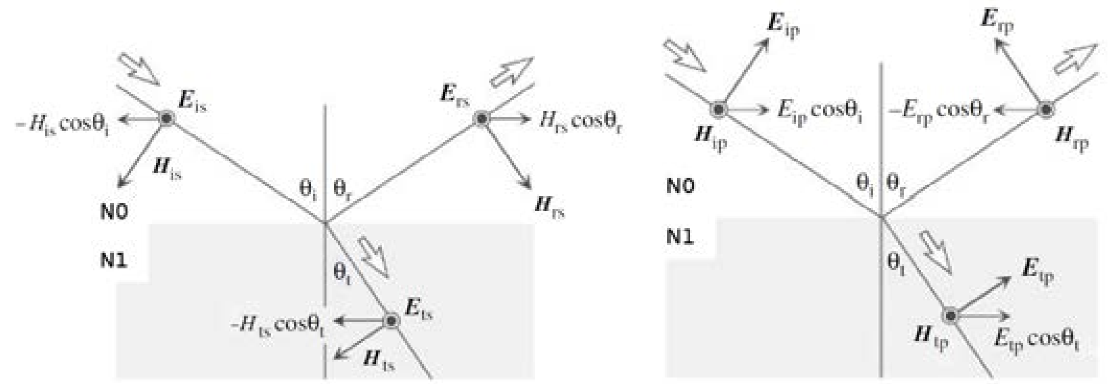

Fig. 2.1 Electric field $\vec{E}$ and magnetic field $\vec{H}$ for s-polarization (left) and p-polarization (right). Fields perpendicular to the plane of the paper are pointing to the reader. (Figures and captions from the book "Spectroscopic Ellipsometry Principles and Applications" [55])

and conditions lead to the determination of Fresnel coefficients expressed as followed [54]:

$$r_s = \frac{E_{rs}}{E_{is}} = \frac{N_0 \cos(\theta_i) - N_1 \cos(\theta_t)}{N_0 \cos(\theta_i) + N_1 \cos(\theta_t)} \qquad r_p = \frac{E_{rp}}{E_{ip}} = \frac{N_1 \cos(\theta_i) - N_0 \cos(\theta_t)}{N_1 \cos(\theta_i) + N_0 \cos(\theta_t)} \tag{2.1}$$

where $N_0 = n_0 - i \cdot k_0$ and $N_1 = n_1 - i \cdot k_1$ are the complex refractive indexes of the ambient medium and the substrate, respectively. Using Snell's law describing the passage of a light through the boundary between two media $N_0 \sin(\theta_i) = N_1 \sin(\theta_t)$, all Fresnel coefficients can be written as a function of θ_i:

$$r_s = \frac{N_0 \cos(\theta_i) - N_1 \sqrt{1 - (\frac{N_0}{N_1} \sin(\theta_i))^2}}{N_0 \cos(\theta_i) + N_1 \sqrt{1 - (\frac{N_0}{N_1} \sin(\theta_i))^2}} \qquad r_p = \frac{N_1 \cos(\theta_i) - N_0 \sqrt{1 - (\frac{N_0}{N_1} \sin(\theta_i))^2}}{N_1 \cos(\theta_i) + N_0 \sqrt{1 - (\frac{N_0}{N_1} \sin(\theta_i))^2}} \tag{2.2}$$

As the intensity of the light is proportional to the square of the magnitude of its electric field, the reflectance R can be expressed as a function of Fresnel coefficients:

$$R = \frac{I_r}{I_i} = \frac{|E_r|^2}{|E_i|^2} = |r|^2 \quad \Rightarrow \quad R_s = |r_s|^2 \quad , \quad R_p = |r_p|^2 \tag{2.3}$$

and therefore as a function of the refractive indexes of the two media and the incident angle of the light on the substrate.

2.1.3 Mathematical treatment considering two interfaces

(a) S-polarisation

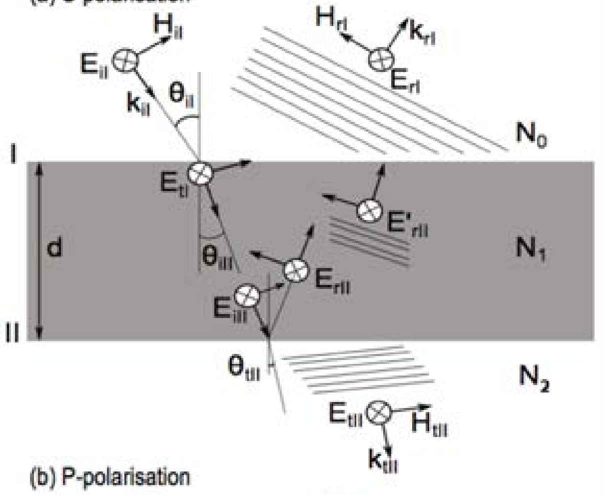

(b) P-polarisation

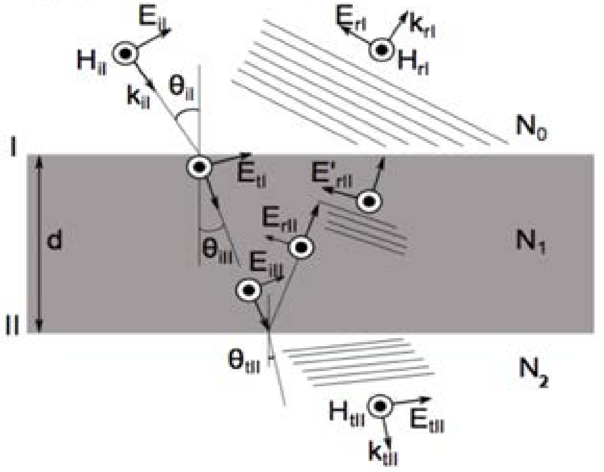

Fig. 2.2 Schematics of a ambient/film/substrate system for both s and p polarisations (Schematics from [57]).

The case of a s-polarised light passing through a thin film deposited on a semi-infinite substrate as depicted in figure 2.2 is treated here. Although both the thin film and the substrate can potentially be of similar nature and structure, it is important to treat them mathematically as two distinct entities. Indeed, their thickness difference is such that the waves reflected at the interfaces *I* and *II* can interfere with each other in the thin film, whereas the interference can be ignored in the substrate as the thickness is large enough for the wave to fade and vanish while propagating through. As discussed previously, an electromagnetic wave crossing the interface between two media must respect a couple of boundary conditions (see Appendix B), which gives rise to the following equations at the interface I:

$$\begin{aligned} E_I &= E_{iI} + E_{rI} = E_{tI} + E'_{rII} \\ H_I &= (H_{iI} + H_{rI}) \cdot \cos(\theta_{iI}) = (H_{tI} + H'_{rII}) \cdot \cos(\theta_{iII}) \end{aligned} \tag{2.4}$$

and at the interface II:

$$\begin{aligned} E_{II} &= E_{iII} + E_{rII} = E_{tII} \\ H_{II} &= (H_{iII} + H_{rII}) \cdot \cos(\theta_{iII}) = H_{tII} \cdot \cos(\theta_{tII}) \end{aligned} \tag{2.5}$$

All these equations can be expressed in terms of the electric field E considering that $H = \sqrt{\frac{\varepsilon_0}{\mu_0}} N \cdot E$, which gives for the interface I:

$$\begin{aligned} E_I &= E_{iI} + E_{rI} = E_{tI} + E'_{rII} \\ H_I &= \sqrt{\frac{\varepsilon_0}{\mu_0}} N_0 (E_{iI} + E_{rI}) \cdot \cos(\theta_{iI}) = \sqrt{\frac{\varepsilon_0}{\mu_0}} N_1 (E_{tI} + E'_{rII}) \cdot \cos(\theta_{iII}) \end{aligned} \tag{2.6}$$

and for the interface II:

$$\begin{aligned} E_{II} &= E_{iII} + E_{rII} = E_{tII} \\ H_{II} &= \sqrt{\frac{\varepsilon_0}{\mu_0}} N_1 (E_{iII} + E_{rII}) \cdot \cos(\theta_{iII}) = \sqrt{\frac{\varepsilon_0}{\mu_0}} N_2 E_{tII} \cdot \cos(\theta_{tII}) \end{aligned} \tag{2.7}$$

Considering the phase difference $k_0 h = k_0 N_1 d \cos(\theta_{iI})$ between the interfaces I and II, we have:

$$\begin{aligned} E_{iII} &= E_{tI} \cdot e^{-i \cdot k_0 h} \\ E_{rII} &= E'_{rII} \cdot e^{+i \cdot k_0 h} \end{aligned} \tag{2.8}$$

with $k_0 = \frac{2\pi}{\lambda}$ being the wavenumber in vacuum. Therefore equations 2.7 can be re-written as:

$$\begin{aligned} E_{II} &= E_{tI} \cdot e^{-i \cdot k_0 h} + E'_{rII} \cdot e^{+i \cdot k_0 h} \\ H_{II} &= \sqrt{\frac{\varepsilon_0}{\mu_0}} N_1 (E_{tI} \cdot e^{-i \cdot k_0 h} + E'_{rII} \cdot e^{+i \cdot k_0 h}) \cdot \cos(\theta_{iII}) \end{aligned} \tag{2.9}$$

After a series of mathematical rearrangements of equations 2.6 and 2.9, one can express the electric and magnetic fields at interface *I* as a function of those at interface *II*, leading to the following matrix form:

$$\begin{bmatrix} E_I \\ H_I \end{bmatrix} = \begin{bmatrix} \cos(k_0 h) & i \sin(k_0 h)/\Upsilon_1 \\ i \sin(k_0 h) \cdot \Upsilon_1 & \cos(k_0 h) \end{bmatrix} \cdot \begin{bmatrix} E_{II} \\ H_{II} \end{bmatrix} \tag{2.10}$$

with $\Upsilon_1 = \sqrt{\frac{\varepsilon_0}{\mu_0}} N_1 \cos\theta_{iII}$. In a more complex stratified sample, it is easy to see how the fields at the first interface could be expressed as a function of those from the last interface using multiple matrices to describe each layer. Replacing E_I and E_{II} by the right part of equations 2.6 and 2.7 gives:

$$\begin{bmatrix} E_{iI} + E_{rI} \\ (E_{iI} - E_{rI})\Upsilon_0 \end{bmatrix} = \mathbf{M} \cdot \begin{bmatrix} E_{tII} \\ E_{tII}\Upsilon_2 \end{bmatrix} \tag{2.11}$$

with $= \mathbf{M}$ the characteristic matrix and:

$$\Upsilon_0 = \sqrt{\frac{\varepsilon_0}{\mu_0}} N_0 \cos\theta_{iI} \qquad \Upsilon_1 = \sqrt{\frac{\varepsilon_0}{\mu_0}} N_1 \cos\theta_{iII} \qquad \Upsilon_2 = \sqrt{\frac{\varepsilon_0}{\mu_0}} N_2 \cos\theta_{tII} \tag{2.12}$$

where all angles can be expressed as a function of the incident angle using Snell's law:

$$\cos\theta_{tII} = \sqrt{1 - \frac{N_0^2}{N_2^2}(\sin\theta_{iI})^2} \qquad \cos\theta_{iII} = \sqrt{1 - \frac{N_0^2}{N_1^2}(\sin\theta_{iI})^2} \tag{2.13}$$

Once we divide both sides of the matrix system by E_{iI}, we have [54]:

$$\begin{bmatrix} 1+r_s \\ (1-r_s)\Upsilon_0 \end{bmatrix} = \mathbf{M} \cdot \begin{bmatrix} t_s \\ t_s\Upsilon_2 \end{bmatrix} \tag{2.14}$$

as $r_s = \frac{E_{rI}}{E_{iI}}$, $t_s = \frac{E_{tII}}{E_{iI}}$. After expanding the matrix, r_s and t_s are given by:

$$r_s = \frac{\Upsilon_0 m_{11} + \Upsilon_0\Upsilon_2 m_{12} - m_{12} - \Upsilon_2 m_{22}}{\Upsilon_0 m_{11} + \Upsilon_0\Upsilon_2 m_{12} + m_{12} + \Upsilon_2 m_{22}} \tag{2.15}$$

$$t_s = \frac{2\Upsilon_0}{\Upsilon_0 m_{11} + \Upsilon_0\Upsilon_2 m_{12} + m_{12} + \Upsilon_2 m_{22}} \tag{2.16}$$

with the different elements of the matrix $\mathbf{M}$ noted m_{xy}. A similar mathematical treatment can be done for the p-polarised wave [54] and leads to the same expression for r except for Υ_0, Υ_1 and Υ_2 now given by:

$$\Upsilon_0 = \sqrt{\frac{\varepsilon_0}{\mu_0}} N_0/\cos\theta_{iI} \qquad \Upsilon_1 = \sqrt{\frac{\varepsilon_0}{\mu_0}} N_1/\cos\theta_{iII} \qquad \Upsilon_2 = \sqrt{\frac{\varepsilon_0}{\mu_0}} N_2/\cos\theta_{tII} \tag{2.17}$$

This mathematical description of an ambient/film/substrate system is useful to simulate the behaviour of the reflectance, $R = |r_s|^2$, and the transmittance, $T = |t_s|^2$, of a particular wavelength impinging a supported thin film or to fit reflectometry data and estimate physical constants such as the complex refractive index of the film and its thickness.

2.2 Maxwell Garnett mixing rule

The way light propagates through and interacts with a material is characterised by its complex refractive index N or its corresponding dielectric function ε_r. The relationship between these two physical quantities is given by $N = \sqrt{\varepsilon_r \mu_r}$ where μ_r is the relative permeability, which quantifies the ability of a material to response to an external magnetic field. In this section, we will treat the case of non-magnetic materials where μ_r is taken as 1, hence $N = \sqrt{\varepsilon_r}$. The dielectric constant of the material can be retrieved from reflectometry or other methods such as ellipsometry. When the medium is made of various materials, the physical quantity quantifying the response of the material to an external electric field obtained from the fitting is called 'effective' and encompasses the macroscopic response to the electric field emerging from the microscopic inclusions in a host and the host itself. The effective dielectric constant of the material can be estimated using a mixing approximation theory. Its choice depends on the nature of the material, the fractional quantity of inclusions, their size, their shape and the wavelength at which the medium is probed. Many theories have been built and are very briefly named here to justify our choice to reduce our study to a specific one. The Maxwell-Garnett mixing rule considers a host in which inclusions are embedded. This approach, inherently non-symmetrical in its mathematical formalism, is famous for predicting the colour of spherical gold inclusions in solution [58]. Alternatively, Bruggeman's effective medium approximation is, in its very essence, a symmetric theory and treats the material as an equal mixture of various phases and different volume fractions.

Because of its success in predicting the optical behaviour of gold inclusions in solution and the fact that it predicts well the absorption peaks experimentally observed from samples containing gold particles [59], the Maxwell Garnett mixing rule is considered in the present study and developed here. Let's consider randomly dispersed embedded spherical dielectric inclusions into a host as shown on the figure 2.3. By definition, the proportional constant between the average electric flux density and electric field is given by:

$$< D >= \varepsilon_{eff} < E > \tag{2.18}$$

The average electric flux density and electric field can be described by weighting fields corresponding to the volume fractions of the inclusions (subscript *i*) and host (subscript *e*)

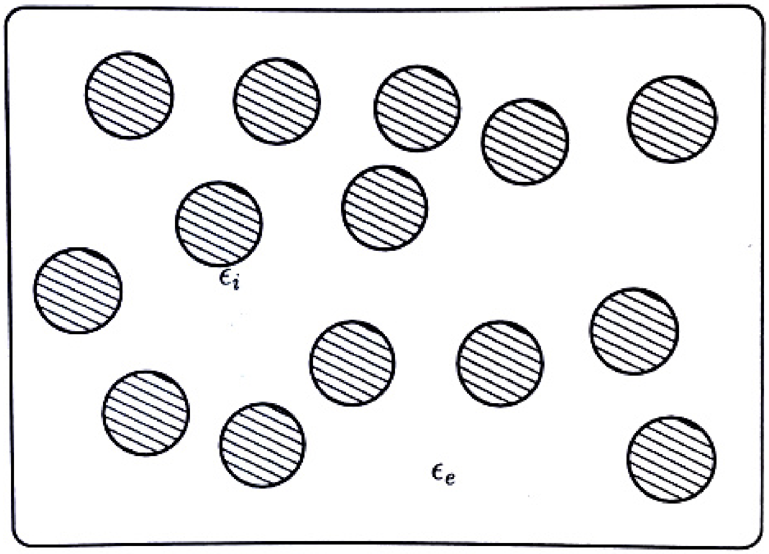

Fig. 2.3 Spherical dielectric inclusions randomly dispersed in a dielectric host (Figure from [60]).

such as:

$$< D > = f\varepsilon_i E_i + (1-f)\varepsilon_e E_e \tag{2.19}$$

$$< E > = fE_i + (1-f)E_e \tag{2.20}$$

where f is the volume fraction of the inclusions. Assigning that $E_i = AE_e$, the effective dielectric constant can be expressed as:

$$\varepsilon_{eff} = \frac{f\varepsilon_i A + (1-f)\varepsilon_e}{fA + (1-f)} \tag{2.21}$$

The following mathematical development demonstrates that the field ratio $A = 3\varepsilon_e/(\varepsilon_i + 2\varepsilon_e)$ in the context of dielectric spheres randomly embedded in a dielectric matrix [56]. As we consider spheres, it is more practical to express the electric field and electric potential in polar coordinates. By definition, these two physical quantities are related by $\vec{E} = -\nabla\Phi$. Let's take the example of an electrical sphere of radius R immersed in an initially uniform external electric field E_e and the coordinate system placed at its centre. The electric potentials inside and outside the sphere are given by:

$$\Phi_i = Br\cos\theta \tag{2.22}$$

$$\Phi_e = Cr\cos\theta + \frac{D}{r^2}\cos\theta \tag{2.23}$$

where θ is the angular coordinate starting at 0° from the reference direction of $\vec{E_e}$. The second term in the expression of Φ_e is the correction to the electric potential induced by the spherical inclusion. In order to determine what are the constants B, C and D, we will rewrite the boundary conditions I and II (see Appendix B) in polar coordinates:

$$\frac{1}{R}\frac{\partial\Phi_i}{\partial\theta}\bigg|_{r=R} = \frac{1}{R}\frac{\partial\Phi_e}{\partial\theta}\bigg|_{r=R} \quad (Tangential\,condition) \tag{2.24}$$

$$\varepsilon_i\frac{\partial\Phi_i}{\partial r}\bigg|_{r=R} = \varepsilon_e\frac{\partial\Phi_e}{\partial r}\bigg|_{r=R} \quad (Normal\,condition) \tag{2.25}$$

Simply by definition of E_e, we know that $C = -E_e$ in equation 2.23. We now have a system of two equations with two unknowns such as:

$$B = -E_e + \frac{D}{R^3} \tag{2.26}$$

$$\varepsilon_i B = -\varepsilon_e E_e - \frac{2\varepsilon_e D}{R^3} \tag{2.27}$$

This system can be easily resolved, given:

$$B = E_e\left(\frac{-3\varepsilon_e}{\varepsilon_i + 2\varepsilon_e}\right) \tag{2.28}$$

$$D = E_e R^3\left(\frac{\varepsilon_i - \varepsilon_e}{\varepsilon_i + 2\varepsilon_e}\right) \tag{2.29}$$

Therefore:

$$\Phi_i = \frac{-3\varepsilon_e}{\varepsilon_i + 2\varepsilon_e} E_e r \cos\theta \tag{2.30}$$

$$\Leftrightarrow E_i = \frac{-3\varepsilon_e}{\varepsilon_i + 2\varepsilon_e} E_e \tag{2.31}$$

One can easily demonstrate that for cylindrical inclusions, we must express the external electric potential such as [56]:

$$\Phi_e = Cr\cos\theta + \frac{D}{r}\cos\theta \tag{2.32}$$

as we reduce the dimension of the system from $3D$ to $2D$. We have therefore:

$$E_i = \frac{-2\varepsilon_e}{\varepsilon_i + \varepsilon_e} E_e \tag{2.33}$$

Now that it has been shown that the field ratio is indeed given by $A = 3\varepsilon_e/(\varepsilon_i + 2\varepsilon_e)$ in the context of dielectric spheres randomly embedded in a dielectric matrix, we can rewrite ε_{eff} in equation 2.21 such as:

$$\varepsilon_{eff} = \varepsilon_e + 3f\varepsilon_e \frac{\varepsilon_i - \varepsilon_e}{\varepsilon_i + 2\varepsilon_e - f(\varepsilon_i - \varepsilon_e)} \tag{2.34}$$

This important result is mathematically identical when written like the following:

$$\frac{\varepsilon_{eff} - \varepsilon_e}{\varepsilon_{eff} + 2\varepsilon_e} = f\frac{\varepsilon_i - \varepsilon_e}{\varepsilon_i + 2\varepsilon_e} \tag{2.35}$$

and it can be generalised for the case of multiples inclusions of different nature:

$$\frac{\varepsilon_{eff} - \varepsilon_e}{\varepsilon_{eff} + 2\varepsilon_e} = \sum_{k=1}^{K} f_k \frac{\varepsilon_k - \varepsilon_e}{\varepsilon_k + 2\varepsilon_e} \tag{2.36}$$

where f_k is the volume fraction of the k_{th} inclusion having ε_k for dielectric constant. In the case where all the randomly dispersed inclusions are cylindrical, the generalised expression for the effective dielectric constant becomes [60]:

$$\frac{\varepsilon_{eff} - \varepsilon_e}{\varepsilon_{eff} + \varepsilon_e} = \sum_{k=1}^{K} f_k \frac{\varepsilon_k - \varepsilon_e}{\varepsilon_k + \varepsilon_e} \tag{2.37}$$

2.3 Semiconductors in excited states

In this section, the nature of various dynamic processes occurring when a population of free carriers is generated in semiconductors are explored. The Drude model is discussed as it enables the determination of the dielectric constant of the material as a function of the carrier density, which is of interest when pumping the sample with a high intensity light beam.

2.3.1 Excited carrier dynamics in semiconductors

Over the last three decades, interest in ultrafast carrier dynamics in semiconductors has greatly increased due to the growing need for faster processing of information by microelectronic devices. To address this need, ultrashort pulse lasers have been developed enabling pump-probe spectroscopy measurements and therefore the investigation of the dynamics of processes involved when pumping. The energy of pump photons is first transferred to the electron, generating electron-hole pairs. This gives rise to a modification of the optical properties of the material, which can be studied by looking at the optical response of the probe signal when reflected, absorbed and transmitted by the excited material. After the photoexcitation, the whole system goes back to its original ground state through a series of relaxation processes between the electrons, between the electrons and the lattice and finally through various possible recombination events [61]. Four stages can be distinguished and can be seen in figure 2.4 [62]. First of all, all stages form a continuous chain of events with some significant overlaps occurring in the range from femtoseconds to microseconds. To generate a large population of free carriers, light is shone onto a semiconductor with an energy greater than its electronic bandgap and single photon absorption takes place (figure 2.5a), exciting electrons from the valence band to the conduction band. In the case of an indirect bandgap, such as silicon, a phonon is emitted or absorbed to provide the momentum needed to change the electron's k-vector. Multiphoton absorption (a) and free carrier absorption (b) can also take place. Sometimes energetic carriers give away some of their energy and momentum, which excite an additional carrier. This process is called impact ionisation (c). After the excitation, carrier-carrier scattering (e) and carrier-phonon scattering (f) redistribute the energy and the momentum, and eventually thermalises the carriers[1]. No change in the number of carriers is induced through thermalisation, but some energy is transferred to the lattice as phonons are emitted. When thermal equilibrium is achieved in a semiconductor, the material will gradually go back it its ground state and the electron-hole pairs start to recombine. There are several paths by which the electrons fall from the conduction band to unoccupied sites in the valence band. For materials allowing direct transitions (g), the electron makes a transition to a lower-energy state and releases its excess energy in the form of a photon. This can be visualised as the opposite phenomenon of the single photon absorption and luminescence is observed. In the case of indirect transitions, radiative recombination is insignificant, but the recombination can still occur, giving away the energy through the means of a phonon. Auger recombination (h) occurs when an electron recombine with a hole and gives its energy and momentum to a carrier, exciting it higher in the conduction band. Recombination can also arise from the presence of defects in the lattice or chemical impurities in the material. This creates energy levels in the bandgap, which capture electrons in the vicinity and assist the recombination. This mechanism is called the Shockley-Read-Hall process [63]. Unlike recombination processes, carrier diffusion doesn't reduce the number of free carriers as it

---

[1] Thermalisation means that the different bodies involved in the elastic and inelastic scattering processes reach thermal equilibrium. Elastic scattering occurs solely between carriers where no transfer of energy is involved, only momentum.

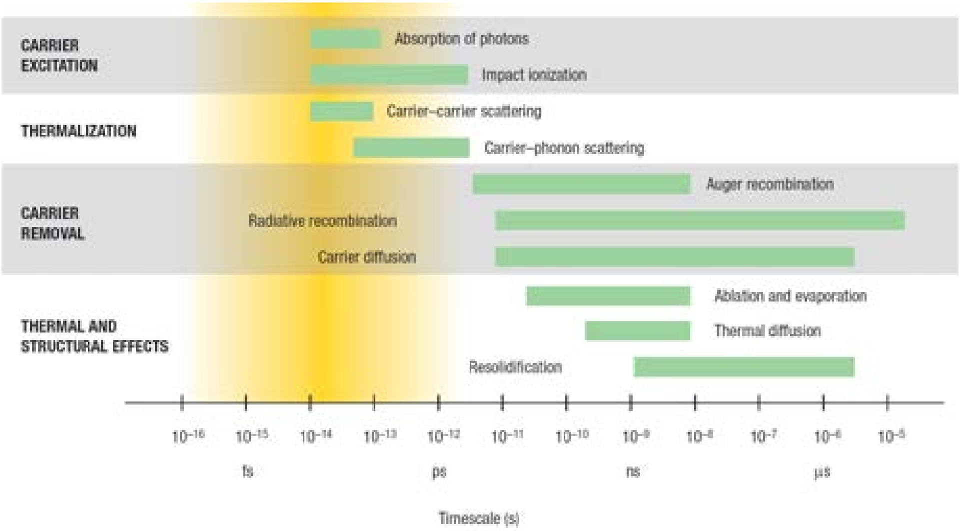

Fig. 2.4 Timescales of various electron and lattice processes in laser-excited solids. Each green bar represents an approximate range of characteristic times over a range of carrier densities from 10^{17} to $10^{22}\,cm^{-3}$ (Figure and caption from [62]).

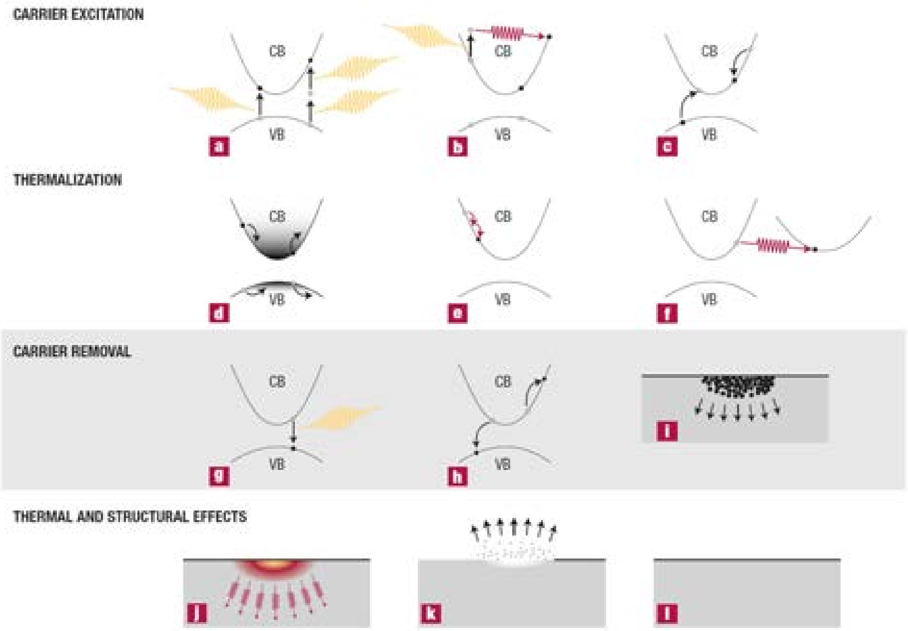

Fig. 2.5 Electron and lattice excitation and relaxation processes in a laser-excited direct gap semiconductor. CB is the conduction band and VB the valence band. a) Multiphoton absorption. b) Free-carrier absorption. c) Impact ionization. d) Carrier distribution before scattering. e) Carrier–carrier scattering. f) Intervalley phonon scattering. g) Radiative recombination. h) Auger recombination. i) Diffusion of excited carriers. j) Thermal diffusion. k) Ablation. l) Resolidification or condensation. (Figure and adapted caption from [62]).

only displaces them from the region where they were originally excited to another location in the material. When the pump intensity is very high and some of its energy has been deposited into the lattice through the previous processes developed above, the material heats up (j) to the point where liquid or gas phases nucleate, leading to the ejection of material out of the surface (k). Over time, the material cools down and solidifies back.

2.3.2 The Drude model

Metals, doped-semiconductors and pumped semiconductors all exhibit optical properties associated with their free carriers and these can be determined using the Drude model [64]. First of all, we ignore the restoring force when the electrons are in the presence of an external oscillating electric field as they are not bound to the atoms [65]. In this context, we write the following equation of motion:

$$m_e\frac{d^2x}{dt^2}+m_e\Gamma\frac{dx}{dt}=-eE(t)=-eE_0e^{i\omega t} \tag{2.38}$$

where the first term describes the acceleration of the electrons and the second term characterises the friction of the electrons in the medium with a damping rate Γ. The mass m_e is the mass of the electron in vacuum. In semiconductors, we must use the effective mass m^*, which accounts for the band structure since the motion of an electron in a periodic potential is different from its motion in vacuum. In metals, the effect can be ignored as the sheer number of free electrons screens the crystal potential. The solution of the equation of motion provides [64]:

$$x=\frac{eE(t)}{m^*(\omega^2-i\Gamma\omega)} \tag{2.39}$$

The polarisability of free electrons is $P_{fc} = -N_{eh}ex$, where N_{eh} is the carrier density. The electric displacement field D is therefore given by:

$$\begin{aligned} D &= \varepsilon\varepsilon_0 E \\ &= \varepsilon_0 E + P_{back} + P_{fc} \\ &= \varepsilon_{back}\varepsilon_0 E - \frac{N_{eh}e^2 E}{m^*(\omega^2 - i\Gamma\omega)} \end{aligned} \tag{2.40}$$

where P_{back} accounts for the polarisability of the bound electrons and ε_{back} is the dielectric constant of the material prior pumping. We now have an expression for the dielectric constant as a function of the carrier density:

$$\varepsilon = \varepsilon_{back} - \frac{\omega_p^2}{(\omega^2 - i\Gamma\omega)} \tag{2.41}$$

where ω_p is called the plasma frequency and is defined by $\omega_p^2 = \frac{N_{eh}e^2}{m^*\varepsilon_0}$. In the case of a metal, one can consider $\varepsilon_{back} = 1$ [66]. The contribution of the free carriers to the dielectric constant can be written as $\Delta\varepsilon_{fc} = \Delta\varepsilon_{fc,r} - i\Delta\varepsilon_{fc,i}$, with :

$$\Delta\varepsilon_{fc,r} = -\frac{\omega_p^2}{(\Gamma^2 + \omega^2)}, \quad \Delta\varepsilon_{fc,i} = \frac{\omega_p^2\Gamma}{\omega(\Gamma^2 + \omega^2)} \tag{2.42}$$

where $\Delta\varepsilon_{fc,r}$ and $\Delta\varepsilon_{fc,i}$ are the real part and imaginary part of the contribution of the free carriers to the dielectric constant respectively. Therefore, the free carrier density affects both the way the light propagates and is absorbed in the material. The two important parameters are the plasma frequency, ω_p, and the damping rate, Γ, or the damping time, $\tau = 1/\Gamma$. The former depends on the free carrier density and the effective mass whereas the latter characterises carrier-carrier and carrier-phonon scattering processes. The success of the Drude model in time-resolved pump-probe reflectometry measurements was established in 1983, when experiments were carried on silicon with $90\,fs$ excitation pulse to demonstrate for the first time that the transfer of energy occurs from the excited carriers to the lattice in the first few picoseconds of the relaxation [67]. This was achieved using a very simple expression of the dielectric constant depending on the number of free carriers such as $\varepsilon = \varepsilon_{back} - \frac{\omega_p^2}{\omega^2}$. In their work, Shank et al. ignored the damping time and attributed the slow decay of the reflectance after excitation to the diffusion of the carriers in the bulk material and to the change of state of the material as it melted. Two more mechanisms responsible for change in the dielectric constant ε^* of the excited material can be added, such as the excited dielectric constant is written [68]:

$$\varepsilon^* = \varepsilon_g + \Delta\varepsilon_{pop} + \Delta\varepsilon_{bgs} + \Delta\varepsilon_{fc} \tag{2.43}$$

where ε_g is the ground state dielectric constant and $\Delta\varepsilon_{fc}$ is the contribution to the dielectric constant from the free carrier as shown previously. The first contribution is the effect of state and band filling, which corresponds to the saturation of interband absorption at high pumping powers [69]. Its contribution to the dielectric constant is written $\Delta\varepsilon_{pop}$ and is a function of N_e/N_0, where $N_0 = 2 \cdot 10^{23} cm^{-3}$ is the total electron density in the valence band. It can be easily ignored for pumping levels up to 10^{21}. The second one is the renormalisation of the band structure and occurs due to electron-electron interactions. In the presence of newly excited carriers, the potential is slightly modified. This also happens when impurities, defects or dopants are present in the material. It is denoted in the expression of the dielectric constant by $\Delta\varepsilon_{bgs}$. Sabbah and Riffe reported that there is a critical number of free carriers $6 \cdot 10^{18} cm^{-3}$ below which the renormalisation of the band structure is absent and also that, at higher excitation densities, this effect can be ignored as previous experiments showed no sign of it and it varies slowly with N, as $N^{1/3}$ [70]. Even up to a $10^{22} cm^{-3}$ free carrier density, Sokolowski et al. concluded that the reflectivity of the pumped silicon follows a Drude-like response and that using equation 2.41 is valid [68].

2.4 Nonlinear optics applied to the case of centrosymmetric material

The developments found in this section are inspired and adapted from the references [71] (In particular chapters 1 and 4 are of main interest here) and [72], where an extensive study of the field is presented. Nonlinear phenomena occur in media in which the induced polarisation, P, responds nonlinearly to the strength of the applied electric field, E. In this section, we confine our discussion to a one dimensional problem as we will ignore any possible anisotropy of our samples further in the text. Hence, all parameters defined in this section are scalars. Conventionally, we consider a linear relationship between P and E:

$$P = \varepsilon_0 \chi^{(1)} E \tag{2.44}$$

where $\chi^{(1)}$ is known as the linear susceptibility of the material. In nonlinear optics, we use a power series in the electric field strength, E, to expression the induced polarisation, P:

$$P = \varepsilon_0 (\chi^{(1)} E + \chi^{(2)} E^2 + \chi^{(3)} E^3 + ...) \tag{2.45}$$

where $\chi^{(2)}$ and $\chi^{(3)}$ are the second and third order nonlinear susceptibilities and refer to the second and third order nonlinear polarisation, such as:

$$P = P^{(1)} + P^{(2)} + P^{(3)} + ... \tag{2.46}$$

In this work, we will look at a composite made of silicon and gold that have a diamond and fcc lattice respectively, which are centrosymmetrical crystalline forms. This means that the crystalline structure is indistinguishable before and after applying the inversion operation on its inversion centre. We consider the case where the nonlinear polarisation is limited to the second order in a centrosymmetric medium, such as:

$$P^{NL} = \varepsilon_0 \chi^{(2)} E^2 \tag{2.47}$$

If we change the sign of the electric field, the sign of the polarisation changes automatically as the material possesses a centre of inversion. Hence,

$$-P^{NL} = \varepsilon_0 \chi^{(2)} (-E)^2 \tag{2.48}$$

$$\Leftrightarrow -P^{NL} = \varepsilon_0 \chi^{(2)} E^2 \tag{2.49}$$

The only way for $-P^{NL}$ and P^{NL} to be equal is for the nonlinear polarisation to vanish. Consequently, $\chi^{(2)} = 0$ in centrosymmetric media. Physically, this means that perturbations in the waveform of the atomic response to the incident electromagnetic wave characterised by even harmonics[2] are forbidden in a material that possesses a centre of inversion. Therefore, we focus our attention on third-order nonlinear optical processes described by $P^{(3)}(t) = \varepsilon_0 \chi^{(3)} E(t)^3$. Let's consider the simplest case where the applied field is monochromatic and its electric field is expressed by:

$$E(t) = E_0\, cos(\omega t) \tag{2.50}$$

where, E_0 is the amplitude of the field and ω its frequency. When raised to the cubic, we can use the following trigonometric identity $cos^3(\omega t) = \frac{1}{4} cos(3\omega t) + \frac{3}{4} cos(\omega t)$ and write:

$$P^{(3)}(t) = \frac{1}{4} \varepsilon_0 \chi^{(3)} E_0^3 cos(3\omega t) + \frac{3}{4} \varepsilon_0 \chi^{(3)} E_0^3 cos(\omega t) \tag{2.51}$$

The first term describes the process in which a photon of frequency 3ω is generated from three photons of frequency ω and is called third harmonic generation. The second term is

---

[2] Harmonics are whole number multiples of the frequency of the incident light.

the nonlinear contribution to the polarisation at the frequency of the applied field, i.e. a nonlinear contribution to the refractive index experienced by the incident light. In the latter, the refractive index of the material is intensity dependent and can be written as:

$$n = n_0 + n_2 I \tag{2.52}$$

where n_2 is the optical constant characterising the rate at which the refractive index is modified by the light intensity and is called the nonlinear refractive index. The total polarisation considering its nonlinear contribution affecting the probe beam is given by:

$$P(t) = \varepsilon_0 \chi^{(1)} E(t) + \frac{3}{4} \varepsilon_0 \chi^{(3)} E_0^2 E(t) \equiv \varepsilon_0 \chi_{eff} E(t) \tag{2.53}$$

where $\chi_{eff} = \chi^{(1)} + \frac{3}{4}\chi^{(3)} E_0^2$ is the effective susceptibility of the nonlinear material. We can now establish the relationship between n_2 and $\chi^{(3)}$ as $n^2 = 1 + \chi_{eff}$. We have:

$$(n_0 + n_2 I)^2 = 1 + \chi^{(1)} + \frac{3}{4}\chi^{(3)} E_0^2 \tag{2.54}$$

Since the time average intensity of the field is given by $I = \frac{\varepsilon_0 n_0 c}{2} E_0^2$, we write:

$$(n_0 + n_2 \frac{\varepsilon_0 n_0 c}{2} E_0^2)^2 = 1 + \chi^{(1)} + \frac{3}{4}\chi^{(3)} E_0^2 \tag{2.55}$$

$$\Leftrightarrow n_2 = \frac{3}{4 n_0^2 \varepsilon_0 c} \chi^{(3)} \tag{2.56}$$

The change in the real part of refractive index, sometimes referred to as the optical Kerr effect, can be positive and negative. When the Kerr coefficient n_2 is positive, the material acts as a converging lens. Indeed, as the Gaussian beam enters the material, the refractive index increases. But the change is more intense in the central part than it is at the edges of the beam profile. Therefore this is equivalent to say that the centre of the beam passes through a longer distance of a uniform material, like it does in a converging lens. Another way of representing this is that the central part of the Gaussian beam travels more slowly than the light at the edge of the beam profile as the refractive index is higher in the central area of the beam. Therefore the wave front is distorted and the beam focuses as shown in figure 2.6. By opposition, when n_2 is negative, the beam is defocused while propagating in the medium. When the light is nonlinearly absorbed while propagating in the material, $\chi^{(3)}$ is complex. In literature, the nonlinear absorption coefficient is represented by β such as $\alpha = \alpha_0 + \beta I$, where $\alpha_0 = 4\pi k/\lambda$ is the linear coefficient of absorption and k is the imaginary part of the linear refractive index. Induced absorption ($\beta > 0$) and induced transparency ($\beta < 0$) are both possible nonlinear properties associated with the change of imaginary part of the refractive index. These two coefficients describe the light self action upon a material and are of great interest in technologies such as optical limiting [73], modulating and switching devices [74].

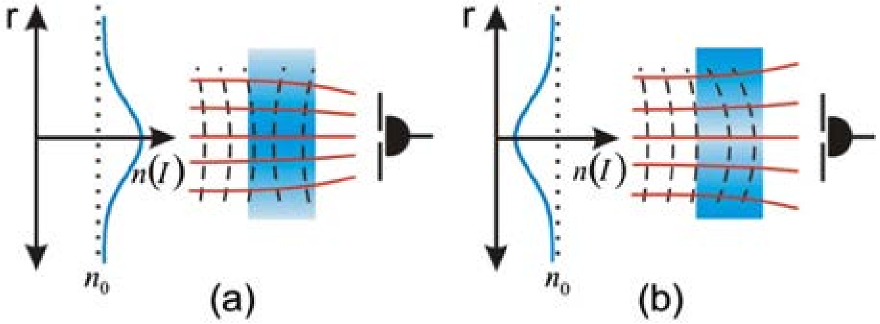

Fig. 2.6 Illustration of the effect of positive (a) and negative (b) increment in the nonlinear refractive index. Positive increment (a) results in self-focusing of a Gaussian beam, while negative increment (b) induces self-defocusing. (Figure and caption from [75]).

Chapter 3

Production of silver nanoclusters using the MACS with a solid CO_2 matrix

3.1 Introduction

In this chapter, we demonstrate the possibility of producing silver clusters from a CO_2 matrix instead of using an Ar matrix. It is of great importance to address the many challenges further scaling up the MACS to industrials levels induces. One practical limitation is the temperature required to condense the gas matrix, which is around $20K$ for argon, hence the desire to work with a gas that is solid at liquid nitrogen temperature. Here, we introduce the experimental set up and develop an extensive study of the changes in the cluster size-distribution as function of both the metal loading in the CO_2 matrix and the sputtering beam energy using liquid helium as the cooling agent (at $20K$) for comparison with previous studies led on the MACS. The cluster flux is also calculated for each experiment. Results are explained and compared with previous work led on Ar matrices. A brief study at $80K$ is presented using liquid nitrogen, demonstrating the possibility to produce clusters with a much cheaper cooling system.

3.2 Production of silver clusters at $20K$

3.2.1 The experimental setup

The experiments detailed in this section are carried out with the MACS 1 as described in section 1.4. The leak valve previously connected to an argon line is now fed by a bottle of carbon dioxide. The MACS 1 is set up in reflection mode as shown on the figure 3.1. The copper plate makes a 45° angle with both the ion beam and the sample. Once the copper plate is at cryogenic temperature (which takes approximately 90 minutes) and the pressure in the vacuum chamber is below $5 \cdot 10^{-8} mbar$, the production and deposition of silver clusters can take place. This is a two step process. First the matrix is built up by co-depositing Ag and CO_2. Secondly it is sputtered by a high energy argon beam while the clusters are collected on to a TEM grid.

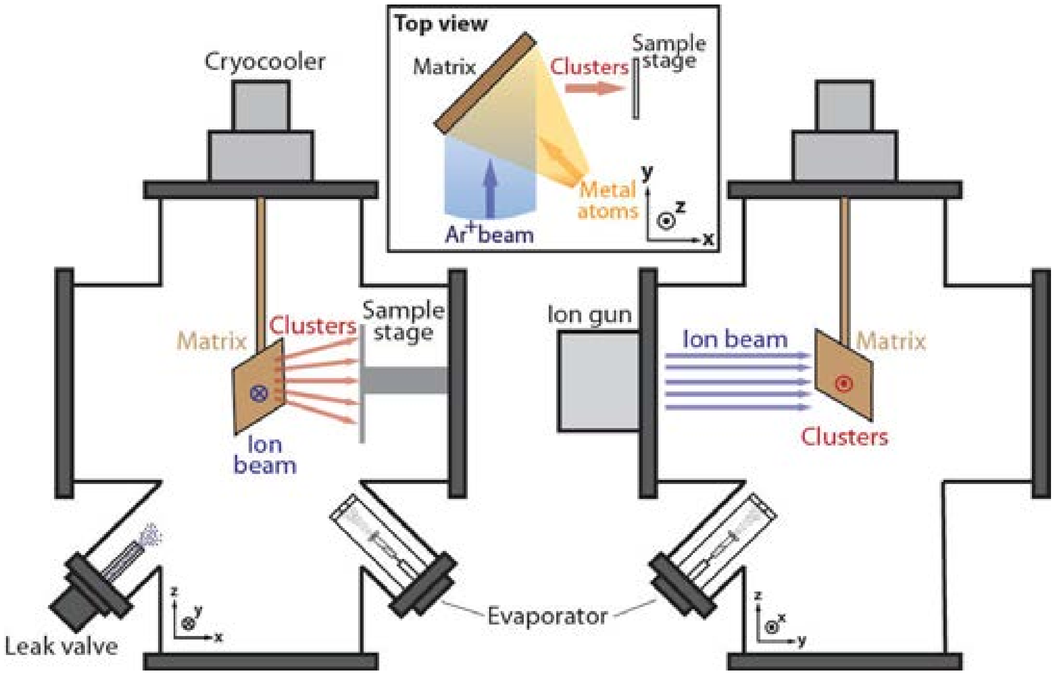

Fig. 3.1 This diagram depicts the geometry of the system as used for the production of silver clusters from a carbon dioxide matrix.

3.2.1.1 Formation of the matrix

The matrix is built up by simultaneously introducing some CO_2 gas in the chamber through the leak valve and evaporating silver atoms on to the copper plate. The pressure of CO_2 is chosen to be equal to $8 \cdot 10^{-6} mbar$. Chosen parameters found empirically are based on previous investigations of the system led by Lu Cao [37]. The temperature of the effusion cell in the evaporator can be chosen according to the desired metal concentration in the dry ice matrix. Based on the developments introduced in section 1.7, one can determine the nominal proportion of silver atoms in the solid carbon dioxide matrix for each temperature of the effusion cell (Table 3.1). In our calculations, we assume a sticking coefficient of one. This assumption is supported by Heald and Brown [76] who showed that the reflected fraction of a CO_2 beam upon a $70K$ surface is insignificant. The major source of error on the metal concentration is most likely to arise from the fact that the gauge is calibrated for nitrogen. Therefore the pressure provided by the gauge requires a correction factor of 1.42 for measurements on CO_2[1]. The nominal Ag concentration is considered and kept throughout the work for consistency of comparison as previous measurements on argon matrices were done ignoring the 1.29 correction factor specific to argon [37] [38]. After 5 minutes of deposition, the shutter of the evaporator and the leak valve are closed and the matrix is built. Its thickness is around $1 \mu m$.

Temperature($^\circ C$)	Nominal (corrected) Ag concentration($\%$)
1150	4 (5.5)
1200	8 (11)
1250	14 (19)
1300	23 (30)

Table 3.1 This table shows the nominal and corrected proportion of silver atoms that there is per hundred molecules of CO_2 for four different temperatures of the crucible inside the evaporator.

---

[1] The correction factor for ionization vacuum gauges for a wide range of gases can be found on commercial websites such as www.mksinst.com. The gauge reading must be divided by the correction factor to obtain the corrected pressure.

3.2.1.2 Sputtering of the matrix

The argon pressure in the Ion Gun is chosen to be equal to $8 \cdot 10^{-6} mbar$ and its current is set to $10 - 15mA$. The beam energy can be tuned and vary between $1keV$ to $4keV$. Recording the current of the ion beam hitting the copper plate is made possible by insulating the plate from the cold finger with a thin piece of sapphire. For a period of 2 minutes, the beam sputters the matrix, inducing the formation of clusters and their extraction without depleting the entire matrix [77].

3.2.1.3 Experimental conditions

The eight different experiments detailed here are performed three times each for statistical purpose and to guarantee the reproducibility. The table 3.2 lists the conditions for each one of them. The four first experiments called A are carried out changing the metal concentration in the dry ice matrix from 4% to 23% keeping the beam energy at $1keV$. The four last ones called B consider a matrix with 14% of metal atoms while changing the sputtering beam energy from $1keV$ to $4keV$. For all these experiments, the clusters are deposited on TEM grids and imaged through STEM.

Experiment type	Beam energy (keV)	Ag concentration(%)
$A1$	1	4
$A2$	1	8
$A3$	1	14
$A4$	1	23
$B1$	1	14
$B2$	2	14
$B3$	3	14
$B4$	4	14

Table 3.2 This table lists the eights different experiments sorted in two categories A and B. The experiments A are carried out for various metal concentrations in the matrix while keeping the sputtering beam energy constant whereas the category B describes the opposite situation. $A3$ and $B1$ are one single experiment.

3.2.2 Analysis of the STEM images

The interest of observing the clusters through aberration-corrected scanning transmission electron microscope is that it enables the determination of their size. Studies investigating the three-dimensional structure of size-selected gold clusters have been successfully carried out using the STEM [78]. Young et al. [79] showed in detail that the image intensity of a cluster is correlated to its mass. They demonstrated that the integrated high-angle annular dark-field (HAADF) intensity I of size-selected gold clusters follows a monotonic dependence on the number of atoms N in clusters for clusters containing up to 6500 atoms. Prior to this, Li et al. [80] showed that the relationship between the integrated HAADF intensity and the size of gold clusters exhibits a linear trend for clusters up to 1500 atoms. Based on those observations, it is valid to consider a linear relationship between the integrated HAADF intensity of small silver clusters and their size expressed in number of atoms as the vast majority of the clusters generated in the MACS1 with a CO_2 matrix contain less than 500 atoms. Therefore the first part of our analysis consists of quantifying the intensity of a single atom. Then, the mass of the cluster can easily be derived considering a linear relation between I and N.

3.2.2.1 Single atom intensity

The single atom intensity is determined from images at a magnification of $10Mx$. While imaging the TEM grid with the STEM, the electron beam sputters some atoms out of the clusters and these land a few nanometers away from the cluster on the bare graphite film (see section 1.8). By drawing two circles around these individual atoms, one can quantify their intensity. Indeed, the single atom intensity is measured by subtracting the background obtained from the area delimiting the two circles from the intensity measured inside the inner circle which contains the atom. Ideally, the area included between the two circles should be twice as large as the area of the inner circle. A smaller area would lead to a poorly average background intensity and a bigger area could potentially include neighbouring single atoms or reach zones where the background is slightly different due to small variations in the film thickness. The figure 3.2 shows a selection of a few single atoms resting on the graphite film and the two circles used for the single atom intensity quantification. Two gaussian distributions of the single atom intensity are shown in the figure 3.3. These distributions are based on a selection of isolated atoms from $5-10$ images each, taken by two different microscopists on different days. In total, the intensity of more than 250 atoms has been estimated. The only parameter that changes between the two sets of data despite the operator and the day is the pixel time, i.e. the time set to record a pixel. On the left graph, the pixel time is $76\mu s/px$ while it is $38\mu s/px$ on the right. In the table 3.3 are listed the values of the mean and the standard deviation for each gaussian distribution. One can see that doubling the pixel time doubles the single atom intensity as expected. This shows that the measurements are consistent with each other.

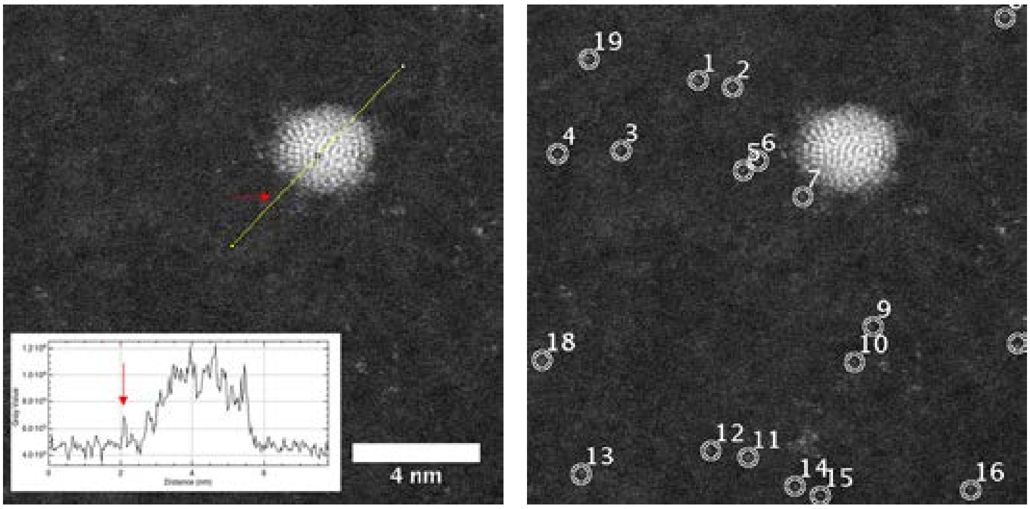

Fig. 3.2 STEM captures at a $10M$ magnification of silver clusters on a thin film of graphite. On the left, a line profile of a silver cluster and a single atom (red arrow) in its vicinity is taking. The image on the right shows the two circles surrounding isolated single atoms used to determine their intensity.

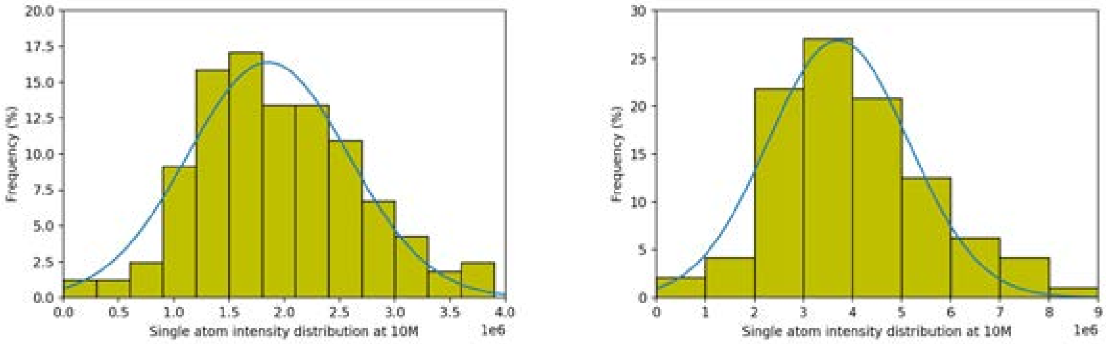

Fig. 3.3 The two graphs presented here show the gaussian distribution of the single atom intensity from a pixel time of $38\mu s/px$ (left) and $76\mu s/px$ (right). The values of the mean and standard deviation for each fitted blue curve are listed in the table 3.3.

Pixel time ($\mu s/px$)	38	76
Mean single atom intensity (10^6 arbitrary unit)	1.8 ± 0.1	3.7 ± 0.2
Standard deviation (10^6 arbitrary unit)	0.7	1.4

Table 3.3 This table lists the fitted mean single atom intensity and their respective standard deviation for gaussian distributions at different pixel times.

3.2.2.2 Cluster size estimation

A similar method to the one presented in the previous section is applied to STEM images (figure 3.4) at a lower magnification ($2Mx$), in which many clusters can be seen. Dividing the intensity of each cluster by the single atom intensity gives the cluster size in number of silver atoms. To convert the single atom intensity I_a from one magnification Mx_a to another magnification Mx_b, we use the following relation:

$$I_b = I_a \cdot \left(\frac{Mx_b}{Mx_a}\right)^2 \tag{3.1}$$

This method has been performed for all the samples listed in the table 3.2 and the results are detailed in the next sections. Prior to this, and in order to establish the validity of this technique and the single atom intensity value, we estimate the diameters of clusters randomly

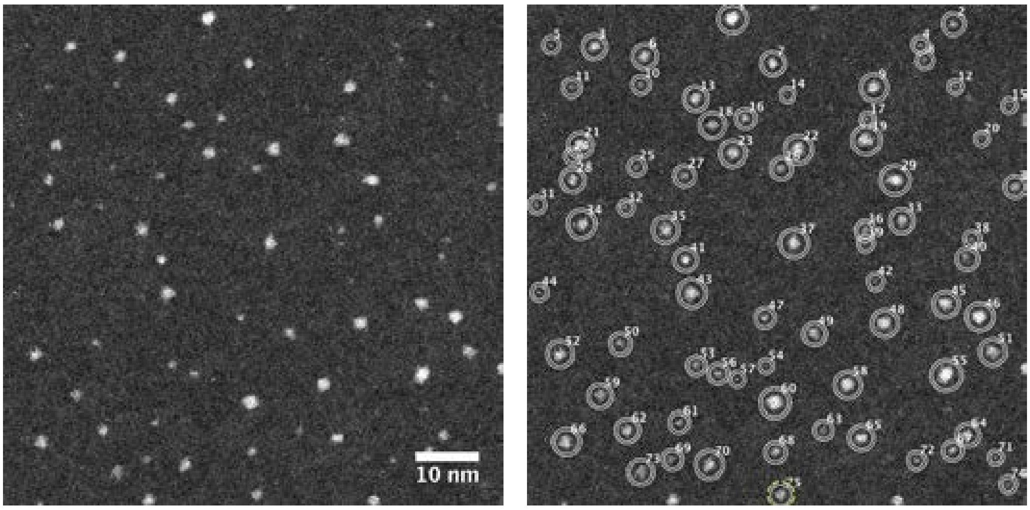

Fig. 3.4 STEM images at a $2Mx$ magnification of silver clusters on a thin film of graphite. The image on the right shows the two circles surrounding silver clusters in order to determine their respective intensity, hence size.

chosen in all samples and compared them to the number of silver atoms the clusters contain, which is determined by dividing the intensity of the cluster with the single atom intensity. To estimate the diameter, a perimeter around the cluster is drawn as depicted in the figure 3.5. The STEM image is first smoothed using a low-pass filter on the image (b) in order to remove the high frequency noise and simplify the selection of a the cluster's perimeter. An intensity threshold is applied to the image (c), which creates areas where the intensity is above the threshold and corresponds to the clusters (in black, figure 3.5c) and areas where the intensity is below the threshold and correspond to the background (in white, figure 3.5c). The perimeter of the area above the threshold is copied on to the original image (d) to confirm that it maps correctly the cluster. The area inside the yellow perimeter is converted into a diameter. We consider here that the cluster has a spherical shape. This assumption is valid for soft landed clusters [81]. By definition, soft landed clusters have a kinetic energy per atom of $E_a \approx 0.1eV$, which prevents them from fragmenting or impinging the substrate when they land. Therefore the conditions of soft landing depend on the cluster size. The bigger the cluster, the lower the energy per atom. Also, bigger clusters are more likely to keep their in-flight properties as they are more stable and less inclined to have their morphology changed by the substrate. In the case of the clusters generated with the MACS, it is considered that they are soft landed as the kinetic energy of the incident argon ion (in the keV range) is dissipated in the matrix at the impact. Therefore the assumption that the clusters are spherical is reasonable. One by one, the diameter of 150 clusters within the whole size-range are determined. The figure 3.6 presents the diameter versus the number of atoms the silver clusters (yellow dots) contain. The following relation:

$$N = \frac{1}{V_a}\left(\frac{4\pi}{3}\left(\frac{D}{2}\right)^3\right) \tag{3.2}$$

expresses the number of metal atoms per clusters N as a function of their diameter D. The fitted parameter is the volume of an atom and its fitted value is $V_a = 17.0 \pm 0.3\mathring{A}^3$. The theoretical volume of the atom V_t (expressed in $\mathring{A}^3$) in bulk silver is given by:

$$V_t = \frac{A_w}{N_A \cdot \rho_m} \cdot 10^{24} = \frac{107.87}{6.02 \cdot 10^{23} \cdot 10.5} \cdot 10^{24} = 17.1\mathring{A}^3$$

From the literature, it is known that silver clusters exhibit various structures with different nearest neighbour distances. Schmidt et al. [82] show that clusters made of less than 10 atoms have slightly smaller nearest neighbour distance between the atoms than the value for bulk silver. It is expected that the bond length between atoms in clusters increases with their size, getting closer to the bulk structure as the clusters get bigger. The fact that the fitted volume for the silver atom in the cluster is close to that of bulk silver is a good indicator that our single atom intensity value is correct.

3.2.3 Experimental results

The size distributions and fluxes of the silver clusters produced from the sputtering of the dry ice matrix with an argon ion beam depends on both the metal loading in the matrix and the

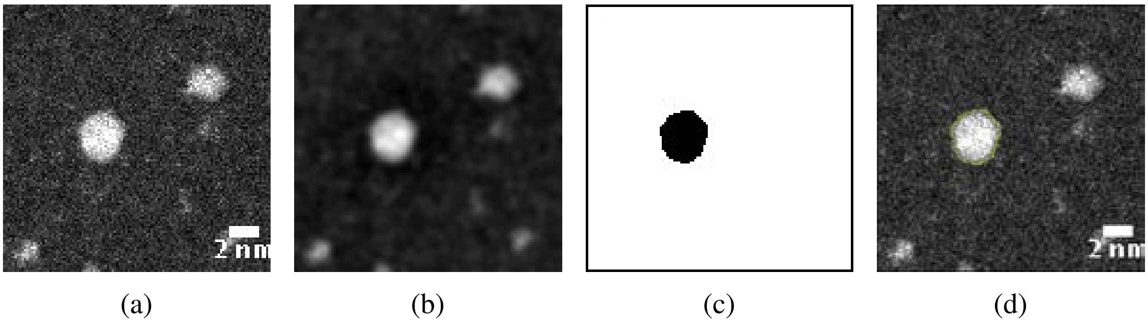

(a) (b) (c) (d)

Fig. 3.5 The sequence of images represents how the diameter of a cluster is estimated. The STEM image (a) of a cluster is smoothed on (b) in order to reduce to noise when applying a threshold (c). The yellow perimeter in (d) surrounds an area that is converted into a equivalent sphere diameter.

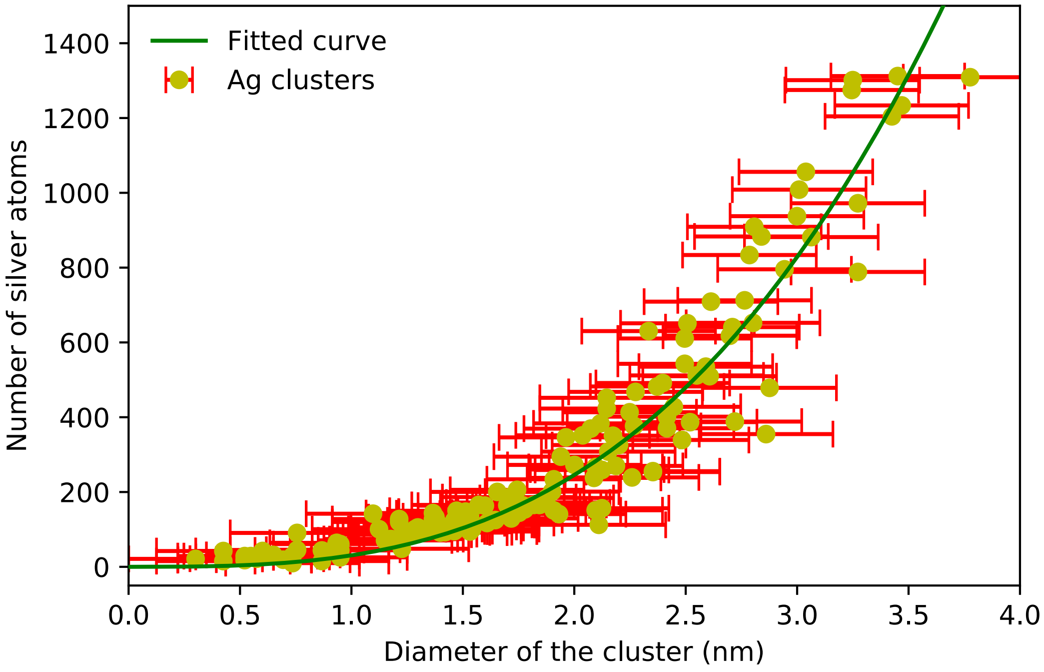

Fig. 3.6 The number of atoms per cluster as a function of the cluster diameter. It is reasonable to assume an error of one pixel when drawing the circumference of the cluster area, which leads to an error on the diameter of 2 pixels ($0.3\,nm$). It is represented by the red horizontal error bars on the graph. The green line is the data fit considering the equation 3.2, which enables to deduce the volume of a silver atom.

energy of the argon ion beam. Here are presented the quantitative results of that study and compared with previous results obtained from an argon matrix.

3.2.3.1 Cluster size-dependence on the metal loading in the matrix

The conditions for this study are presented in the section 3.2.1. The results are based on the analysis of over 12000 clusters. STEM images are shown on the figure 3.7 for each different metal loading investigated. The histograms presented in the figure 3.8 show the size distribution of silver clusters for four different metal loadings from 4% to 23%. The cluster size follows a log-normal distribution. Once the data fitted, values of the mean and mode can be extracted to characterised the lognormal trend observed. The mean sizes of the clusters of increasing metal concentration are 79, 83, 86 and 175 atoms respectively. The peaks of the distributions are 25, 27, 25 and 28 atoms respectively. While the peak's position barely varies, the distribution broadens with increasing metal loading.

3.2.3.2 Cluster size-dependence on the argon ion beam energy

STEM images of the clusters produced for four different energies ($1\,keV$ to $4\,keV$) are shown in the figure 3.9. The histograms shown in the figure 3.10 present the size distribution of silver clusters for the four different argon ion beam energies. As previously, the fitted lognormal curve enables to determine the mean and the mode of the distribution. The mean sizes for increasing energies are respectively 86, 160, 155 and 230. The peaks of the distributions are at 25, 32, 32 and 58 atoms. In this case, the peak's position moves towards bigger clusters as the distribution broadens with increasing ion beam energy.

3.2.3.3 Cluster flux

As the matrix support is isolated from the cold finger, it is possible to record the current of argon ions exiting the ion source and reaching the matrix. It is of interest to study the cluster

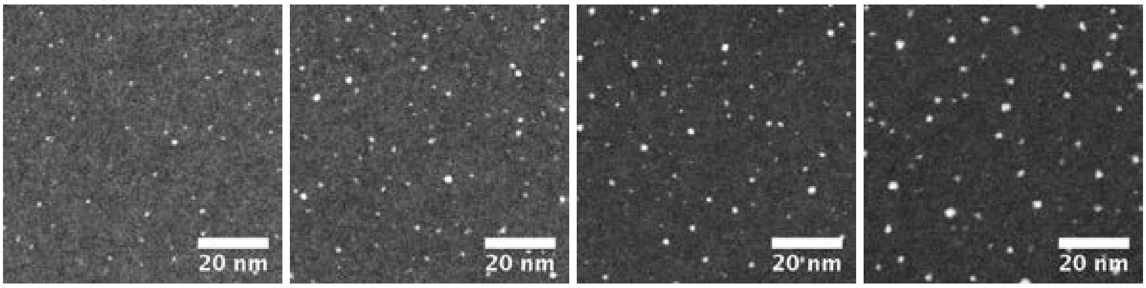

(a) 4% (b) 8% (c) 14% (d) 23%

Fig. 3.7 STEM images of silver clusters produced from different metal loading in the dry ice matrix.

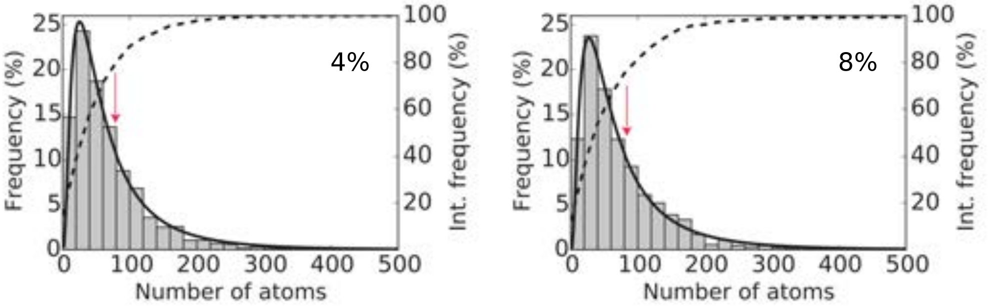

(a) 4% metal concentration (b) 8% metal concentration

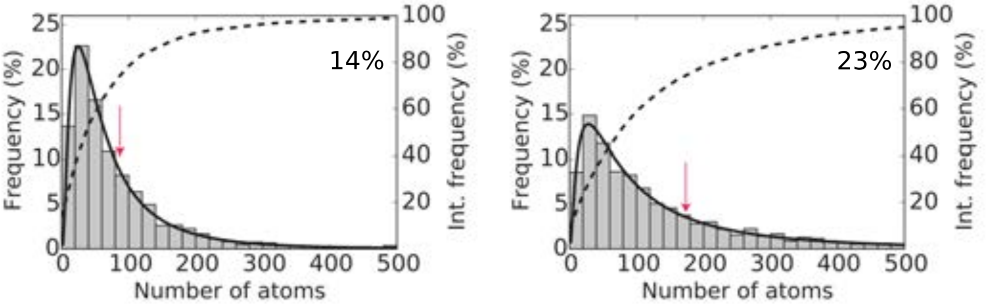

(c) 14% metal concentration (d) 23% metal concentration

Fig. 3.8 The size distribution of silver clusters are shown for four different metal concentrations. The black line is the lognormal fitted curve of the data whereas dotted line shows the cumulative frequencies as labelled on the right y-axis. The red arrow points at the mean size particle.

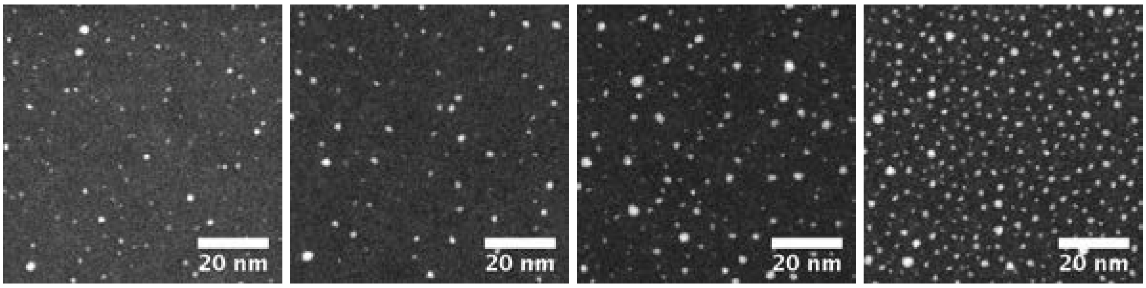

(a) $1keV$ (b) $2keV$ (c) $3keV$ (d) $4keV$

Fig. 3.9 STEM images of clusters produced from a dry ice matrix sputtered by different argon ion beam energies.

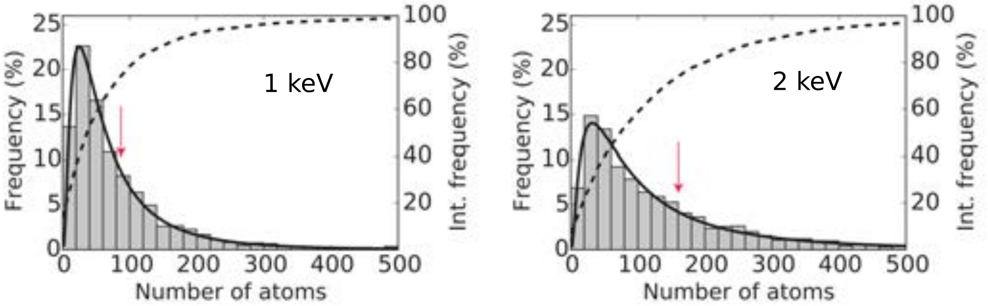

(a) $1keV$ beam energy (b) $2keV$ beam energy

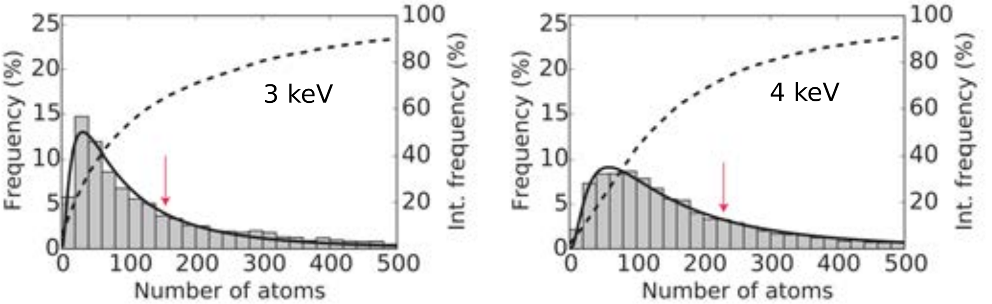

(c) $3keV$ beam energy (d) $4keV$ beam energy

Fig. 3.10 The size distribution of silver clusters are shown for four different argon ion beam energies. The black line is the lognormal fitted curve of the data whereas dotted line shows the cumulative frequencies as labelled on the right y-axis. The red arrow points at the mean size particle.

production per ion impact in order to determine whether higher metal loadings and higher energies of the incident ion contribute not only to the production of bigger clusters but also to the production of more clusters. The currents are listed in the table 3.4 and they show that higher energies lead to higher current. This can be explained by the fact that more argon atoms are ionised when their energy is increased in the gun. We observed that fluctuations of the ion beam current during the experiment were more important at higher energies, hence the larger errors on the average current value. The graph 3.11a shows the number of clusters produced per unit area (μm^2), per μA of argon ion hitting the matrix and per second as a function of the metal concentration and the ion beam energy. One can see that the cluster flux is relatively constant for various metal loading in the matrix. The black line represents the average value, which is around 2.5 clusters per unit area. On the other hand, the graph 3.11b shows the cluster flux produced from incident argon ion beam having different energies and it demonstrates that higher energies lead to an increase in the cluster flux. The green dot on this graph represents the average value over the four experiments using a $1keV$ argon ion beam while changing the metal concentration. By changing the energy of the incident beam from $1keV$ to $4keV$, one can almost double the cluster flux. If we consider that each cluster is charged, we can expressed the cluster flux as a current. The current of clusters, which correspond to the collection of clusters on to the area of a TEM grid (around $7mm^2$) per second, goes from $0.15nA$ at $1keV$ to $0.6nA$ at $4keV$. Depending on the argon ion beam current and its energy, the cluster flux quadruples.

	Metal loading				Ion beam energy			
	4%	8%	14%	23%	$1keV$	$2keV$	$3keV$	$4keV$
Mean ion beam current (μA)	55 ± 5	50 ± 5	55 ± 5	50 ± 5	55 ± 5	45 ± 5	95 ± 25	110 ± 25

Table 3.4 This table lists the mean incident argon ion beam current over the three repeats for each experiment.

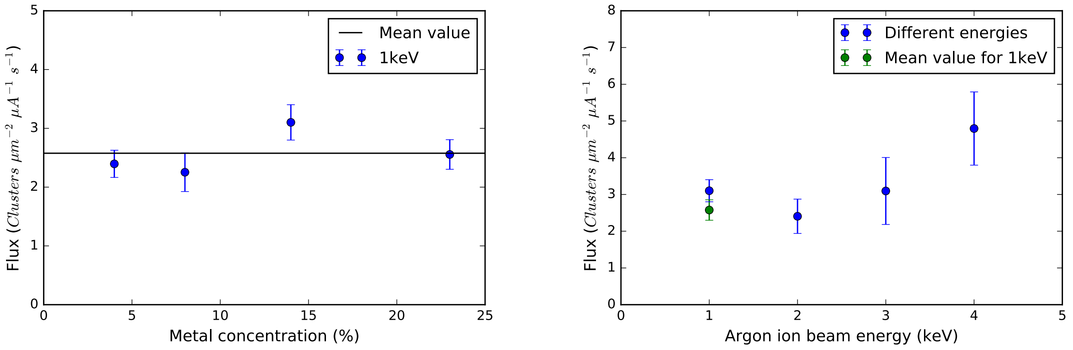

(a) (b)

Fig. 3.11 On this figure are shown the cluster fluxes for various metal concentrations (a) and for various energies (b). The green dot in (b) refers to the average value represented by the black line in (a).

3.2.4 Discussion

3.2.4.1 The log-normal distribution and its implications

The graphs from both figures 3.8 and 3.10 have an asymmetric bell shape and a long tail toward larger clusters, which are features of the log-normal distribution represented by the following probability density function:

$$f(x) = \frac{c}{\sigma x\sqrt{2\pi}} \cdot \exp\left(\frac{-(\ln x - \mu)^2}{2\sigma^2}\right) \tag{3.3}$$

where $\exp(\mu + \sigma^2/2)$ is the mean and $\exp(\mu - \sigma^2)$ is the mode of the distribution. This distribution is well known and often observed in natural sciences (e.g. human's body weights) and in social sciences (e.g. income) [83]. In cluster sciences, the log-normal size distribution of ultrafine particles (around 10nm) was first observed in 1976 by Granqvist and Burhman when they produced nanoparticles from the evaporation of a metal in an oven containing an inert gas [84]. Later on, this inert gas condensation method led to the production of much smaller clusters with a log-normal size distribution as reported in 1991 by Pocsik [85]. Similar trends were observed for clusters produced via laser ablation [86] and radio frequency magnetron plasma sputtering combined with gas condensation [35]. Wang et al. [86] not only show that high precision mass spectrometry of laser generated clusters have such a size distribution but they demonstrate that each type of cluster structure can be associated to different lognormal functions. Moreover, some clusters, which are more stable than others, seem to break locally the distribution form because they are unlikely to undergo further modification. These are called magic number clusters. However, not all nanoparticle size distributions are log-normal. In chemistry [87], the growth of nanocrystals in solution can exhibit a Lifshitz-Slyosov-Wagner (LSW) shape which, unlike the log-normal, has a bell shape towards bigger clusters and a small tail for smaller clusters. This is due to the process called Ostwald ripening which consists in atoms moving from the surface of small clusters where they are weakly bond to join big clusters. Through this process, small clusters disappear in favour of bigger ones.

The cluster size distribution is a characteristic of the growth mechanism. Whereas the normal distribution emerges from a random additive process as it happens for the final position of a N steps one-dimensional random walk, the log-normal distribution finds its origin in the occurrence of a random multiplicative process. A simple example of this is the successive fragmentation of a rock in two smaller rocks. After N fragmentations, the size of a residual rock is the product of all the reduction factors of each individual fragmentation with the initial rock size [88]. In 1993, Villarica et al. applied the Smoluchowsky equation:

$$\frac{\mathrm{d}n_k}{\mathrm{d}t} = \frac{1}{2}\sum_{j=1}^{k-1} K_{j,k-j} n_j n_{k-j} - n_k \sum_{j=1}^{\infty} K_{j,k} n_j \tag{3.4}$$

to the cluster growth [89]. This equation represents the rate of formation of a cluster containing k atoms. The parameter n_k is the concentration of k mers and the K_{ij} are the Kernels; constants that characterise the reaction of i mers and j mers. In order words, they quantify how likely the i mers and j mers will give birth to bigger clusters. The first term of the right side of the Smoluchowsky equation corresponds to the generation of k mers through the collision of two smaller species whereas the second term corresponds to the destruction of k mers when they coalesce with other species to form bigger clusters. The underlying assumptions are that sole monomers are present initially in the system, only binary collisions take place and no fragmentation occurs. In their paper, Villarica et al. show that the log-normal function represents a good approximation to the solution of the Smoluchowsky equation.

In the case of our experimental framework, silver atoms that escape the melted silver in the crucible are unlikely to form dimers and trimers before they reach the growing dry ice matrix onto the copper plate. Indeed, mass spectrometry studies [90] show that the silver dimers escaping the crucible are in small proportions, i.e. $P_{Ag_2}/P_{Ag} \approx 10^{-3}$ where P is the partial pressure. Moreover, as these atoms are hot, two silver atoms require a three-body collisions with a molecule of carbon dioxide to take the vibrational energy away. The number of collisions between one silver atom with CO_2 molecules is given by the product of the cylindrical volume swept out by one silver atom on its way to the matrix support by the density of CO_2 molecules in the vacuum chamber:

$$Nb\ of\ collisions = \pi \cdot d^2 \cdot l \cdot \frac{N}{V} = \pi \cdot d^2 \cdot l \cdot \frac{p}{k_b T} \approx \frac{1}{50} \tag{3.5}$$

where $d = (1.72 + 3.46)$ is the collision radius, taking into account the van der Waals radii of both Ag and CO_2[1], $l \approx 0.1m$ is the distance between the evaporator and the matrix, $p = 8 \cdot 10^{-4} Pa$ is the carbon dioxide pressure in the chamber, and $T = 293K$ its temperature. As the collision between one silver atom and one carbon dioxide molecule is a rare event, a three body collision involving another silver atom is even rarer and unlikely to occur. This argument is still valid for atoms being sputtered out of the matrix as the sputtering pressure is of similar order as the dosing pressure. From previous work done with the MACS [37],

---

[1] The CO_2 Van der Waals radius is calculated considering a spherical volume of the molecule in its solid cubic structure

we know that the clusters don't solely form on the amorphous carbon by aggregation simply because the cluster size distribution isn't a function of deposition time. Also mass spectra of the cluster produced from the matrix were measured and they showed a shift in signal towards bigger masses for matrixes containing higher metal loadings, which guaranties the formation of clusters prior deposition. Therefore we conclude that the clusters form initially inside the dry ice matrix from the coalescence of embedded silver atoms and that this process is enhanced when sputtering the matrix. Simulations done by Kai Nordlund and Junlei Jones Zhao (unpublished work) on solid argon matrixes containing 5% and 10% silver atoms show the formation of silver clusters inside the matrix by aggregation prior and after sputtering with 200 argon ions at $1keV$.

3.2.4.2 Analysis and comparison of the results

The size distribution is not very sensitive to the metal loading in the dry ice matrix (see figure 3.8). No significant change is noticed for metal loadings of 4% to 14%. This behaviour is different from the previous work when an argon matrix was used whether it is in transmission mode or in reflection mode (see section 1.6). Experiments carried on with the MACS showed a much more significant size-dependence on the metal loading of the clusters from an argon matrix than that of produced from a dry ice matrix. Indeed, for $\approx 1\%$ to $\approx 6\%$ metal concentration in an argon matrix, the mean cluster size goes from hundreds to thousands silver atoms. In our study, the mean cluster size stays under 250 silver atoms even at 23% metal loading.

We know that the cluster formation takes place in the matrix from the existence of a single log-normal distribution, and that the size is dependent on both the loading and the ion beam energy. Sputtering the matrix provided energy to the system so that it is rearranged and the silver atoms and pre-formed small clusters meet to form bigger clusters prior their extraction. Therefore, in order to understand this difference in clusters size between the Ar and CO_2

matrixes, it is important to look at the bonding energy between the different constituents of the matrix and compare the strength of their bonds. A possible explanation is that the bonding energy of Ag in Ar is $\approx 0.2eV$ [91] [92], whereas the bonding energy of Ag in CO_2 is $\approx 1eV$ [93]. The mobility of Ag is therefore much greater in an argon matrix than in a dry ice matrix. This favours the formation of bigger clusters for higher metal loadings in the former than in the latter. Moreover, the enthalpy of sublimation of carbon dioxide is $27.2kJ/mol$ [94], whereas that of argon is $7.7kJ/mol$ [95] [96], which is more than three times lower. This means that the Van der Waals interactions between argon atoms are weaker than that of CO_2 molecules and that the reorganisation of the matrix is likely to be more consequent in Ar than in CO_2, leading to initial bigger clusters (prior any sputtering). Another explanation is that the major difference between the size distributions in an argon and dry ice matrixes is due to the process through which the clusters are extracted. In transmission mode, it is likely that the clusters grow while passing through the matrix before they are extracted in the direction of the sputtering beam.

When looking at the size distribution as a function of the argon beam energy (see figure 3.10), we see here that bigger clusters are produced. Two competing processes are happening here. On one hand, a higher beam energy provides more momentum to the matrix to rearrange, which enables the migration and aggregation of metal atoms and clusters together to form bigger ones. On the other hand, the matrix depletes more quickly under high ion beam energy (i.e. the growth time is reduced), preventing the formation of bigger clusters. Since bigger clusters are in fact collected when the beam energy is increased, we can conclude that the former mechanism prevails on the latter. This is in agreement with previous work on the MACS with an argon matrix.

It is also known from the literature that the sputtering yield of condensed rare gases increases with the beam energy and is superior to that of a CO_2 matrix. The sputtering yield of a solid Ar matrix with an Ar ion beam increases from 412 to 1252 atoms per ion impact when the ion energy changes from $1keV$ to $4keV$ [44]. For comparison, the sputtering yield of solid carbon dioxide is 501 atoms per impact of argon ion having an energy of $4keV$ [45]. Here, it is observed that the cluster production increases slightly with the beam energy (see figure 3.11), showing that a larger amount of material is ejected from the matrix with increasing beam energies. In other words, the depletion of the matrix under bombardment by a $4\,keV$ argon ion beam is faster than at $1\,keV$.

In summary, although it is reasonable to conclude that the mechanism leading to the formation of bigger cluster prevails, higher amount of material ejected are observed for higher beam energies. This is explained by the fact that the matrix is not entirely depleted and the material consumption during the sputtering process increases with the beam energy.

3.3 Production of silver clusters at liquid nitrogen temperature

Sputtering material at a higher temperature is of interest. Cooling the matrix support with nitrogen instead of helium would reduce the cost of the MACS when operating. In this section, we demonstrate that silver clusters can be produced at liquid nitrogen temperature using a CO_2 matrix. The cluster source used in this section is the MACS 2 described in chapter 4, where the liquid helium tank is replaced by a liquid nitrogen one.

3.3.1 Experimental conditions

The matrix is built up as usual by simultaneously evaporating silver atoms and condensing CO_2 molecules onto the copper matrix support. In the case of the liquid nitrogen cooling agent and considering the limitations imposed by the geometry of the system, the metal concentration in the CO_2 matrix is around 1%. The CO_2 dosing pressure is fixed at $3 \cdot 10^{-6} Torr$ and the dosing temperature is $80K$. As one can see on the figure 3.12, this experiment is conducted in a region of net process of condensation. Higher metal fluxes would require a higher temperature for the evaporation cell and this would lead to an increase in temperature on the matrix support because of their physical proximity. In this case, the matrix would no longer be able to condense the CO_2 gas into a solid film. The matrix is sputtered with either a $1.5keV$ or a $3keV$ argon ion beam with an argon pressure of $1 \cdot 10^{-6} Torr$. The current registered on the matrix support is $15\mu A$. While sputtering, the temperature drops to $78K$ as the shutter of the evaporator is closed. Once again, the region in which this work is done ensures a stable condensed matrix. For the sake of comparison and consistency, experiments were repeated at both liquid helium and nitrogen temperatures with the MACS2. In the case of liquid helium, the dosing temperature is around $30K$ whereas the sputtering temperature is $17K$.

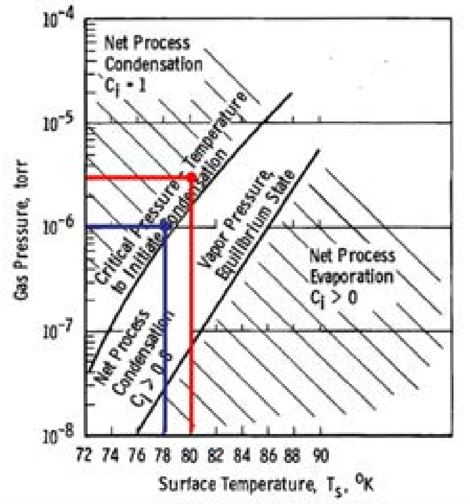

Fig. 3.12 Evaporation and condensation regions for CO_2 studied in the temperature range of $72-90K$ [76]. The red line shows the matrix dosing conditions whereas the blue line shows the sputtering conditions.

3.3.2 Analysis of STEM images

This study is based on the analysis of approximately 3000 clusters. The samples were produced and analysed a few months after that of the section 3.2.2.1, and therefore the single atom intensity is re-estimated in the frame of these samples. At a $10Mx$ magnification the value obtained for a single atom is $1.9 \cdot 10^6$, which is extracted from the fitting of the bell curve on the graph presented in the figure 3.13. This result based on the selection of 250 single atoms is in very good agreement with previous results despite the poorer image quality due to the sample contamination as one can see on the figure 3.13. Regarding the cluster size, the technique adopted here is the same than the one detailed in the section 3.2.2.2.

3.3.3 Temperature comparison

We demonstrate here the successful production of silver clusters at liquid nitrogen temperature. The size-distribution of silver clusters produced from a 1% silver concentration in the dry ice matrix sputtered with an argon ion beam of $1.5keV$ energy is shown in the figure 3.14 at both $17K$ (top) and at $78K$ (bottom). The cluster fluxes expressed in $Clusters/(\mu m^2 \cdot \mu A \cdot s)$

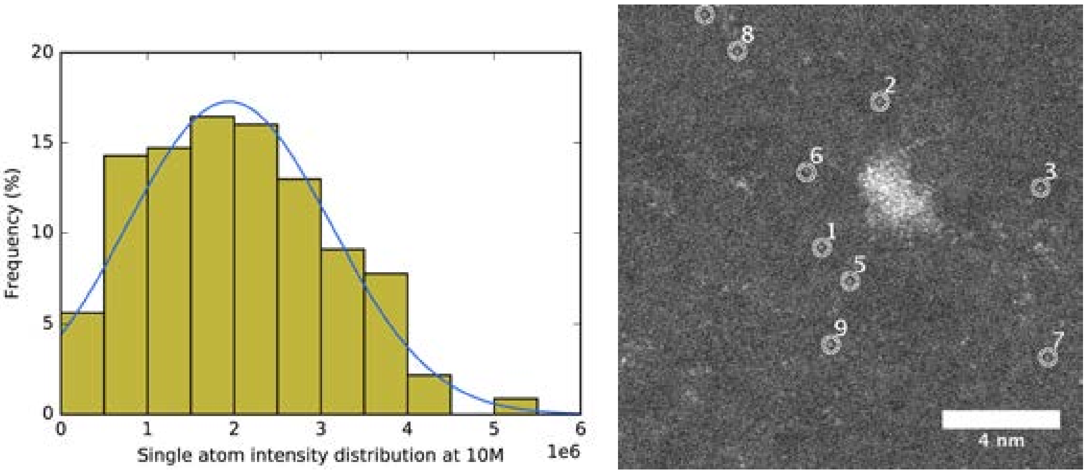

Fig. 3.13 The mean value of the gaussian curve (left) gives the single atom intensity value at a $10M$ magnification. This study is based on the selection of 250 clusters as depicted on the STEM image (right) and described in the section 3.2.2.1.

are 0.55 at $17K$ and 0.75 at $78K$. There is a 40% cluster flux increase between the two experiments. Also, figure 3.14 tells us that the production of bigger clusters happens at lower temperature. Indeed, the mode of the size-distribution is around 50 atoms per cluster formed from a CO_2 matrix at $17K$, whereas it is only 10 atoms per cluster for the clusters coming out a CO_2 matrix at $78K$. We notice here that the size-distribution at $78K$ doesn't follow a strict log-normal distribution. At higher temperature, it would be expected that more material is sputtered per ion impact. Brown et al. [97] have shown that the sputtering yield between $17K$ and $78K$ increases by a factor 8 while sputtering the CO_2 film by MeV helium ions. In our work, the keV argon ions could deposit their kinetic energy into the vibrational modes of the dry ice as suggested by Christiansen et al. [45]. If the energy is sufficient to break the bonds, the molecules leave the matrix' surface. This is more likely to happen at $78\,K$ than at $17\,K$ as the energy barrier to break the ice is smaller [97]. This demonstrates that clusters are ejected before they have the chance to form bigger clusters and the cluster flux is increased.

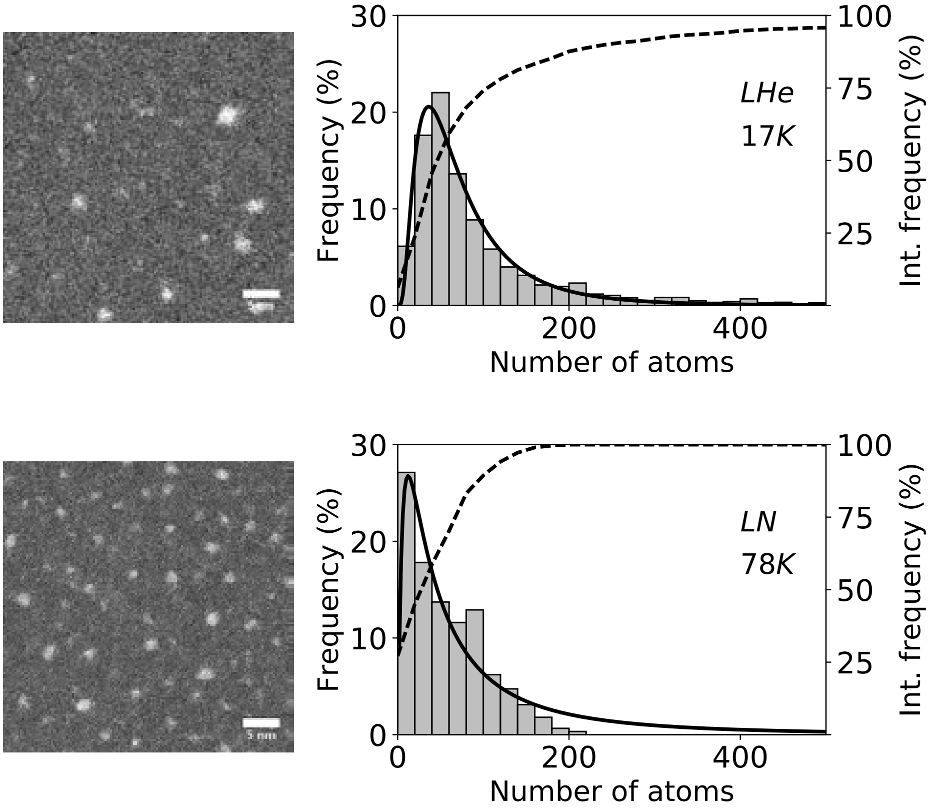

Fig. 3.14 Here are shown the size-distribution of silver clusters produced from a CO_2 matrix with 1% metal loading are presented for two different temperatures. When the system is cooling with liquid helium (top), the temperature recorded is $17K$. Whereas it reaches $78K$ when cooled with liquid nitrogen (bottom). Both histograms are based on the analysis of STEM images as shown here for each temperature. The magnitude is chosen by the microscopist and in this case are different on the two images to facilitate the data analysis. The dotted line on each graph corresponds to the integrated frequency and the plain curve is the log-normal fitted curve.

3.3.4 Different ion argon beam energies

The figure 3.15 shows the size-distributions of silver clusters produced while sputtering a CO_2 matrix at $78K$ with $1.5keV$ (left) and $3keV$ (right) argon ion beam energy. Higher sputtering energies lead, as previously demonstrated, to the production of bigger clusters. In the former, the mean size is around 60 atoms whereas it goes to 90 atoms in the latter. Therefore the dominance of the rearrangement mechanism over the depletion process when increasing the ion beam energy is once more suggested empirically, similarly to what is observed at cryogenic temperatures.

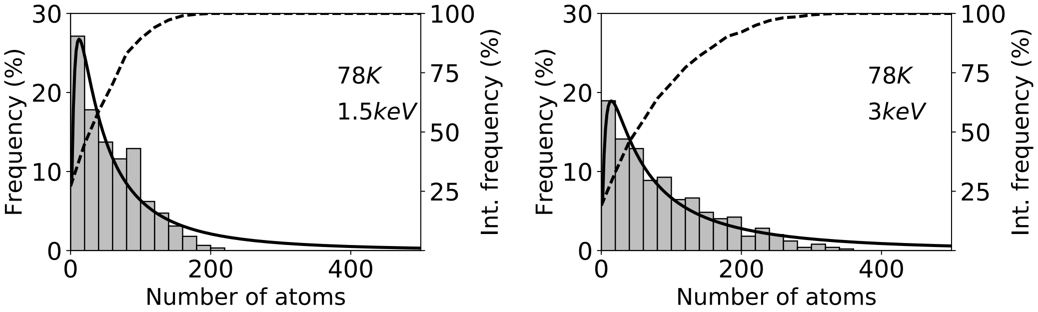

Fig. 3.15 Here are shown the size-distributions of silver clusters produced from a CO_2 matrix with 1% metal loading. On the left, the clusters are sputtered with a $1.5keV$ argon ion beam, whereas on the right the clusters are sputtered with a $3keV$ argon ion beam.

3.4 Conclusion

In this chapter, we first investigated the production of silver clusters in a dry ice matrix at liquid helium temperature. The clusters are deposited onto TEM grids for STEM analysis. The method using the single atom intensity as a unit is validated and enables the study of the size-distribution of the silver clusters produced for four different metal loadings and with four different sputtering beam energies. Increasing both parameters leads to the production of bigger clusters in average but not as significantly as it does in a Ar matrix. One possible explanation for this observation is that the strength of the bonds between atoms in an Ar matrix are weaker than in a CO_2 matrix. The former seems therefore more susceptible to change when being sputtered. Increasing the sputtering energy leads to the production of bigger clusters in greater numbers. The obvious parameter to tune the cluster flux is the ion beam current. The more numerous the incident argon ions are, the more abundant the cluster collection is. Additionally, we demonstrate the successful production of silver clusters at liquid nitrogen, exhibiting smaller sizes than at cryogenic temperature, narrowing the size distribution. The cluster flux displays a 40% increase between $17K$ and $78K$. One explanation for these two observations is that the nanoparticles leave the matrix before they have the opportunity to get bigger as the ice is more fragile at higher temperatures. We show as well that doubling the sputtering beam energy lead to the formation of bigger clusters, widening the size-distribution. More investigations are necessary in order to study the composition of the clusters in flight. A possibility would be to ionise them before they reach a mass-spectrometer. Moreover, high magnification STEM studies would enable the determination of the structure of size-selected clusters deposited on TEM grids.

Chapter 4

Production of powder-supported clusters for catalysis with the MACS 2

4.1 Introduction

One of the many applications of interest for the matrix assembly cluster source is the production of catalytic material. In this chapter, we describe the method used for the production of Ag, Au and $Au-Pd$ clusters deposited onto carbon tape subsequently transformed into a powder. We demonstrate for the first time the possibility to produce binary clusters with the MACS. In order to produce enough material for catalysis, a new matrix assembly cluster source called the MACS 2 is designed and built to accommodate a deposition chamber that can support 21 slides with a total area of 400 cm^2. The first catalytic results obtained from clusters produced with the MACS 2 are presented and discussed.

4.2 Production of a catalyst powder with The MACS 2

4.2.1 The design and working principles

The key component of this new matrix assembly cluster source is its carousel deposition stage supplied by Tear Coating Ltd (figure 4.1). It enables the deposition of clusters over a large area, which makes the production of small quantities of catalysts and biochips [38] possible. In order to collect as many clusters as possible, either the matrix is sputtered close to the deposition stage or the clusters are led towards it with the help of lenses. However, only charged clusters can have their trajectories modified. Because only less than 10% of the MACS 2 generated clusters are charged[1] and because of the fact that lenses could interfere with the ion source, it was decided to collect neutral and charged clusters by bringing the matrix as close as possible to the deposition stage when sputtering. The MACS 2 is built in reflection mode as previous studies on the argon growth showed that this provides a better

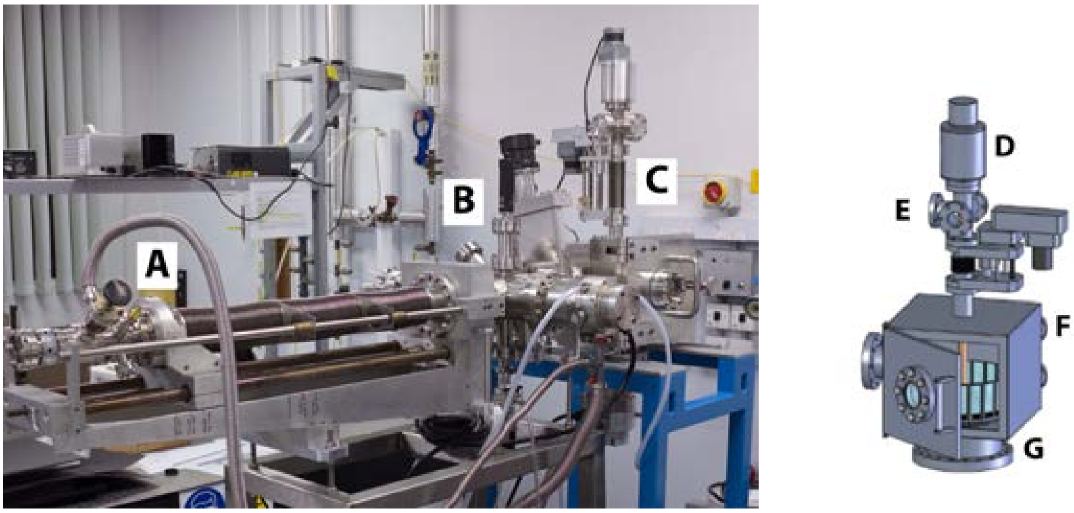

Fig. 4.1 Photo of the MACS 2 (left) and technical drawing of the deposition chamber provided by Tear Coating Ltd (right). The labelled components are: A) linear translator, B) matrix generation chamber, C) deposition chamber, D) rotary drive, E) feedthroughs, F) ports for the gauge, the ion source and the vent valve, G) carousel made of 21 slots to accommodate glass slides.

---

[1] Unpublished study led by Lu Cao.

ion to cluster conversion ratio than the transmission mode [38]. Two distinct chambers are engineered and correspond to the two stages of the cluster formation. First, the matrix is built up by simultaneously dosing argon gas and metal atoms on the copper plate in the matrix generation chamber. Secondly, the matrix is sputtering and clusters are formed, ejected and collected on the slides of the carousel in the deposition chamber. The two chambers are depicted in the figures 4.1 and 4.2. The former shows a picture of the system as it stands once assembled and a technical drawing of the deposition chamber. The later presents diagrams of the top and front views of the system respectively. The chambers are separated by a gate valve, which prevents unnecessary contaminations of the samples while degassing the evaporator and forming the matrix. Additionally, it enables to load and unload the deposition chamber while keeping the matrix generation chamber under high vacuum. Each chamber is equipped with a vacuum system composed of a turbomolecular pump, a rotary pump and a pressure gauge to measure the quality of the vacuum. The rotary pump brings the pressure down to $5 \cdot 10^{-2} mbar$, then the turbomolecular pump is activated and provides a base pressure of around $5 \cdot 10^{-8} mbar$. Both chambers also have vent valves connected to a nitrogen line, minimising water contamination when opening the system. The matrix support is fixed at the extremity of a cryogenically cooled cold finger equipped with a resistive temperature sensor. It is mounted onto a linear translator that enables its smooth motion from one chamber to the other without perturbing its temperature. This cold finger can also rotate so that it faces the evaporators when dosing and the ion source when sputtering.

4.2.2 Matrix formation

The evaporation of Ag and Au atoms is performed with a Createc high temperature effusion cell, also used in the MACS1 (see section 1.4). The crucible is loaded with the desired solid metal and heated to its melting point ($960°C$ for Ag and $1060°C$ for Au) or above, which tunes the flux of material evaporated. Studies at cryogenic temperature (around 20 K) are

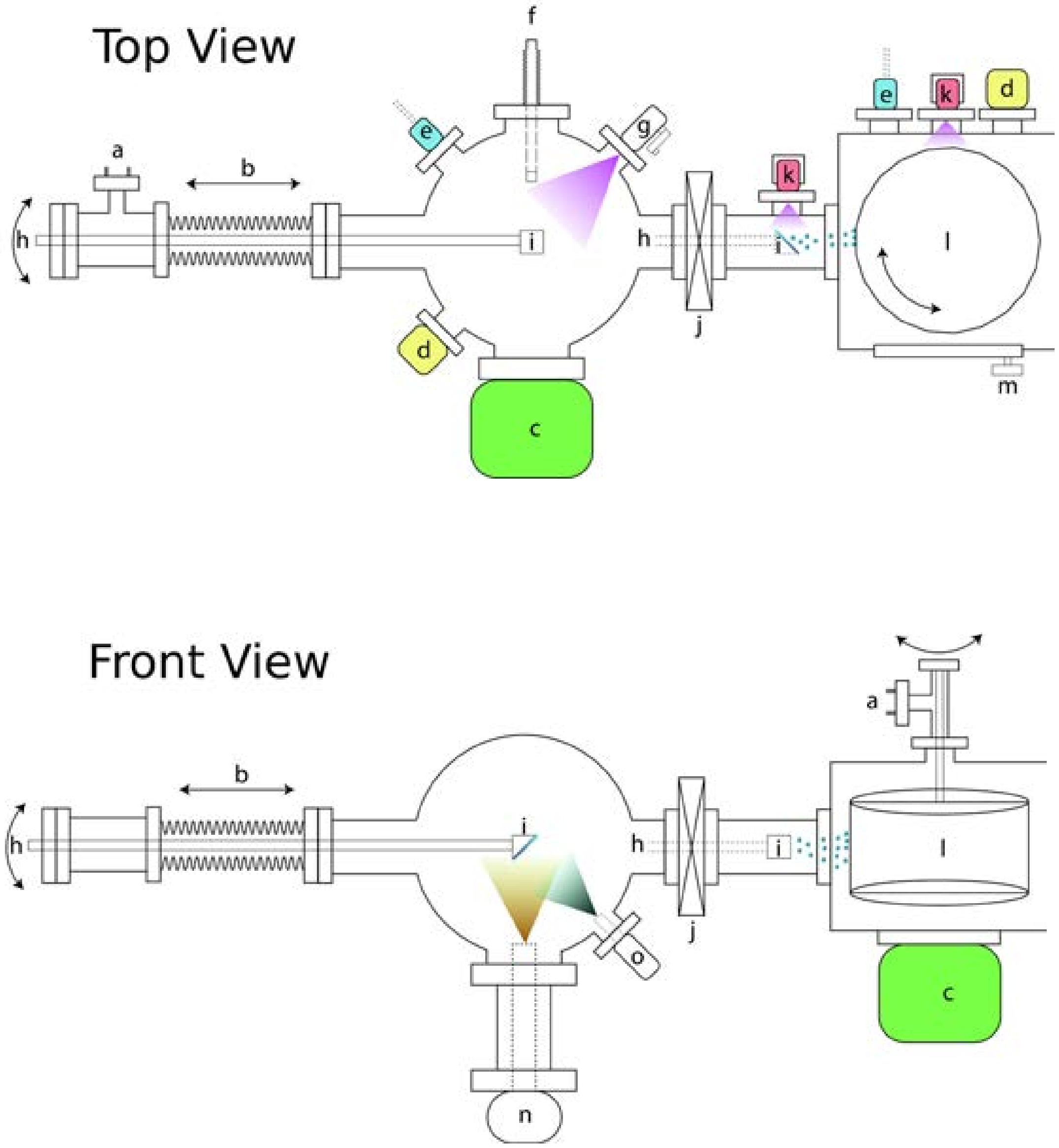

Fig. 4.2 Diagrams of the MACS 2: top view (above) and front view (below). The labelled components are: a) electrical feedthroughs for the temperature sensor fixed on the matrix, the matrix current and (below) for the samples' current, b) manual linear translator, c) pumping systems, d) gauges, e) vent valves, f) retractable crystal quartz microbalance, g) leak valve, h) rotating cold finger, i) matrix, j) gate valve, k) ion sources, l) carousel deposition stage, m) door of the deposition chamber, n) effusion cell, o) e-beam evaporator.

carried out using a transfer line connected on one side to a vacuum isolated container filled with liquid helium and on the other side to the vertical linear driver. The liquid helium is pumped out of the container, through the transfer line until it reaches the internal extremity of the linear driver where the sample is attached. There, it evaporates and the helium gas is carried away to a central helium recycling system. To determine the temperature of the matrix support, a rhodium iron resistance sensor from Oxford Instrument is clamped inside the sample's holder. Four wires are connected to the resistor and permit to determine its resistivity that monotonically decreases with temperature from 500 K to 1.4 K. The temperature chosen for each metal is limited by the cooling power of the cryogenic system. In order to keep the matrix temperature around $25K$ or below, the crucible is heated up to a maximum of $1150°C$ for Ag as it affects the matrix' temperature due to their relative proximity. Therefore, a $20\,cm$ tube extension is placed between the evaporator and the vacuum chamber, which enables to increase the temperature of the crucible up to a maximum of $1500°C$, while keeping the cryogenically cooled matrix support below $25\,K$. Using the quartz crystal microbalance, a concentration of Au in the matrix of up to 1.5% is estimated at $1500°C$. As the vapour pressure of the palladium is a few times lower than that of the gold at a given temperature, and higher temperatures aren't achievable in the effusion cell, an alternative technique is required to evaporate the palladium. To achieve that, the electron beam evaporator EBE-1 from Specs is setup on the MACS2. A Pd rod supported by a rod holder is connected to a power supply so that the electric potential of the rod can be chosen. The used voltage was $1kV$. A $4A$ electric current passes through a tungsten filament located above the rod's apex and heats it up. This generates the emission of electrons from the filament. These electrons are attracted by the positively charged rod and hit it. In turn, the rod heats up and its apex melts and a palladium vapour is generated. An electrode facilitates the measurement of a fraction of the Pd ions coming out of the evaporator. In order to ensure a constant dosing, this flux is kept constant (around $15-17nA$ in this case). The total amount of material deposited onto the matrix holder is measured with a quartz crystal microbalance connected to a Sycon controller that converts the frequency change of the crystal into a film thickness as described in section 1.7. The co-deposition of metal and argon at a pressure of $4 \cdot 10^{-6} mbar$ onto the cryogenically cooled copper plate enables the formation of the matrix. The metal concentration in the solidified rare gas matrix is calculated using equation 1.7 and its values for the different tested metal are listed in table 4.1. The deposition time is fixed at 80 minutes.

Metal	Evaporator's $T°$ or current	Metal concentration(%)
Ag	$1150°C$	2.0
Au	$1450°C$	1.0
Pd	$15-17nA$	1.0

Table 4.1 Concentration of various metals in the solid argon matrix. The temperature of the fusion cell and current of material ejected are given in each case.

4.2.3 Sputtering the matrix

Once the matrix is built up, it is translated to the generation chamber where it is sputtered. The sputtering process enables the formation and the extraction of the metal clusters embedded inside the solidified rare gas. The ion gun used in this work is the ISE 5 Ion Source shown on the figure 4.3. It can generate argon ion beam currents from 25 μA at 0.5 keV to 80 μA at 5 keV. Argon gas is continuously fed into the gas cell via a leak valve manually controlled. A gas discharge is initiated and sustained by applying a voltage between the anode and the gas cell itself, which acts as a cathode. The electrons generated through this process follow a helical path due to the presence of a magnetic field in the source region. On their course the electrons hit argon atoms, which generates more electrons and argon ions. These ions are extracted from the gas cell into a flight tube. A focus element located in the flight tube enables the operator to focus the ion beam before it leaves the ion source, where it reaches its highest kinetic energy. The maintenance of the ion source requires removing the source from

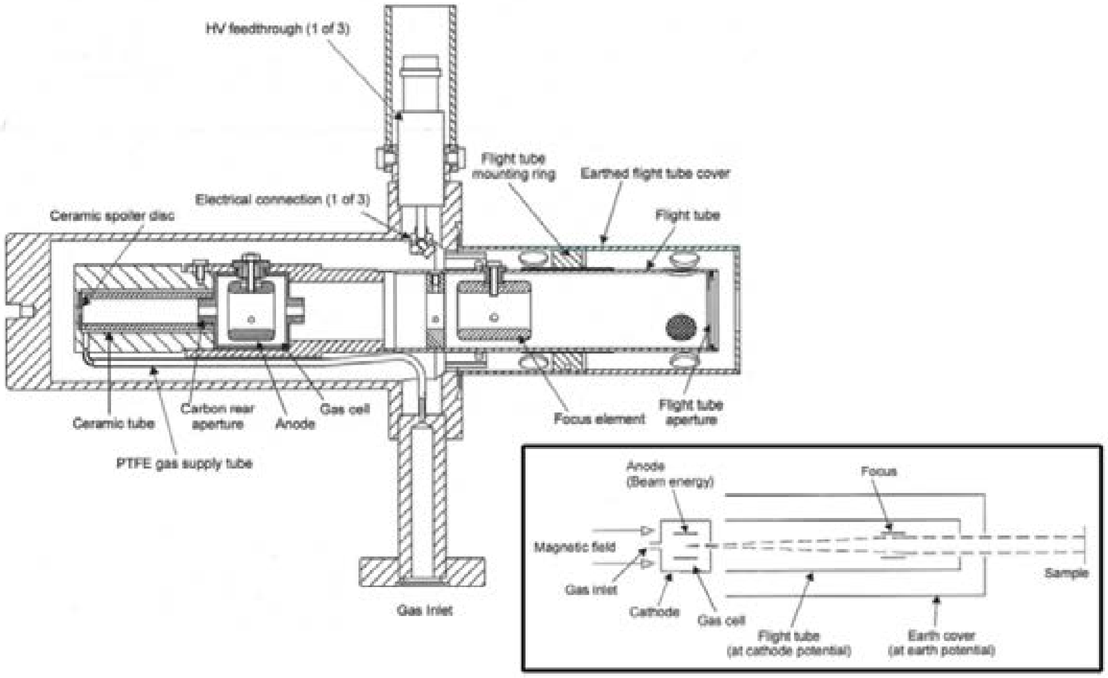

Fig. 4.3 The ISE 5 Ion Source internal schematic. The insert shows the diagram of the principle of operation of the ion source. (Images from Omicron NanoTechnology)

the vacuum system. The instrument needs to be carefully dismantled and cleaned every two to three months, depending on the use. The parameters chosen to operate this ion source are inspired by William Terry's work as he studied the ideal conditions for the cluster production on this particular cluster source and guaranteed a stable functioning of the source over 15 minutes, i.e. the time chosen for deposition [38]. Argon is fed inside the source with a pressure of $1 \cdot 10^{-6} mbar$. The beam current chosen is $15 \mu A$ and the beam energy is $1.5 keV$. These parameters are kept constant for all experiments for the purpose of comparison.

4.2.4 Powder production

The powder production detailed in this work is inspired from previous work done in our laboratories based on size selected *Pd* clusters deposited with the magnetron cluster source on TEM grids and graphite tape [98]. In our case, the support chosen for the deposition of metal clusters is a cheap commercial flexible carbon tape from Minseal. It contains over

99% of carbon and is catalytically inert for the reactions tested as demonstrated further in this work. It is mounted on $7.5x2.5\,cm^2$ glass slides, which fit the carousel. The powder preparation is described here and shown on the figure 4.5. Prior deposition, the graphite tape is first mechanically cut by a diamond saw (DAD321 Automatic Dicer) with a cutting depth of $50-60\,\mu m$ and a cutting pitch of around $800\,\mu m$ as it can be seen in figure 4.4. Another approach using laser was investigated and performed on our samples leading to a cutting depth of around $30\,\mu m$. Because it was much more time consuming (around 4 times longer) and its access was restricted to experts, we opted for the mechanical dicing method. Once the edges of our future flakes had been created, the carbon tape was mounted on glass slides with vacuum compatible double side tape. Then, it was sputtered with a $1\,\mu A$ argon ion beam with an energy of $1\,keV$ for $30\,s$ to generate defects on its surface so that the clusters are stable against sintering [99]. Another option would be to accelerate them to pin them on to the support, which showed good results for size-selected palladium clusters on graphite and prevented them from sintering under realistic conditions for catalytic oxidation of methane [100]. However, this method requires charged clusters and can result in shape

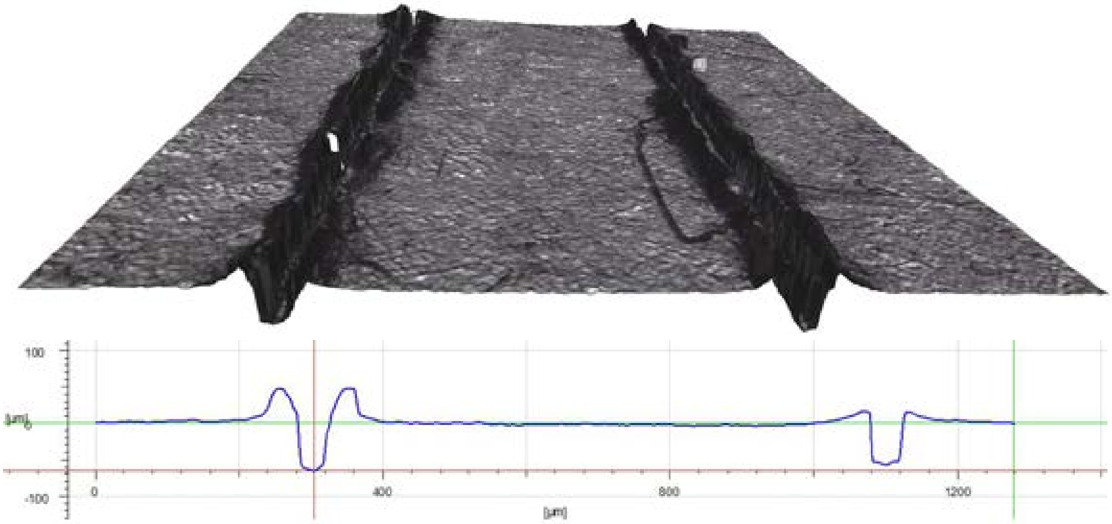

Fig. 4.4 The top picture show an 3D view of the surface of the carbon tape after cutting it with a diamond saw. The bottom view is a perpendicular profile of the surface and shows a $50-60\mu m$ cutting depth. AFM measurements done by Dr Pavel Penchev.

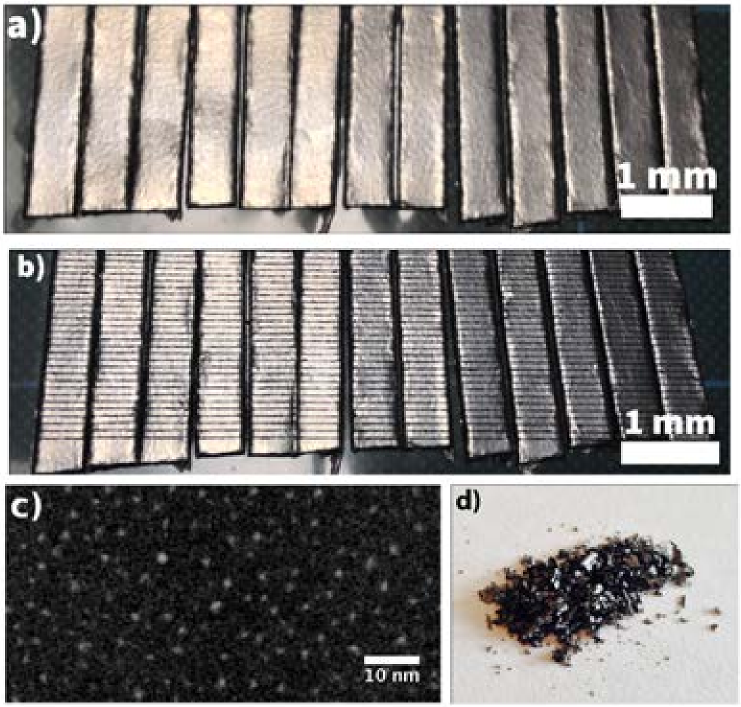

Fig. 4.5 This figure shows the production of powder-supported clusters. The carbon tape (a) is first cut with a diamond saw (b). Clusters (c) are deposited onto its surface and, using a knife edge, the topmost part of its surface is scrapped off to form a powder (d).

being flattened [81]. The clusters are then deposited for 15 minutes. A TEM grid is added onto a slide so that the clusters can be imaged and studied. The new catalyst material is then taken out of the vacuum and turned into a powder by scraping off the topmost diced layer of the carbon tape on which the clusters rest.

4.3 Cluster characterisation

4.3.1 Silver clusters

Silver clusters were made from the sputtering of condensed Ag and Ar atoms in a 2 : 98 ratio onto the matrix support kept at a temperature below $25K$. Their size, determined using the single silver atom HAADF intensity evaluated from high magnification STEM images, gives rise to a log-normal distribution peaking at 30 atoms and an average size around 80 atoms.

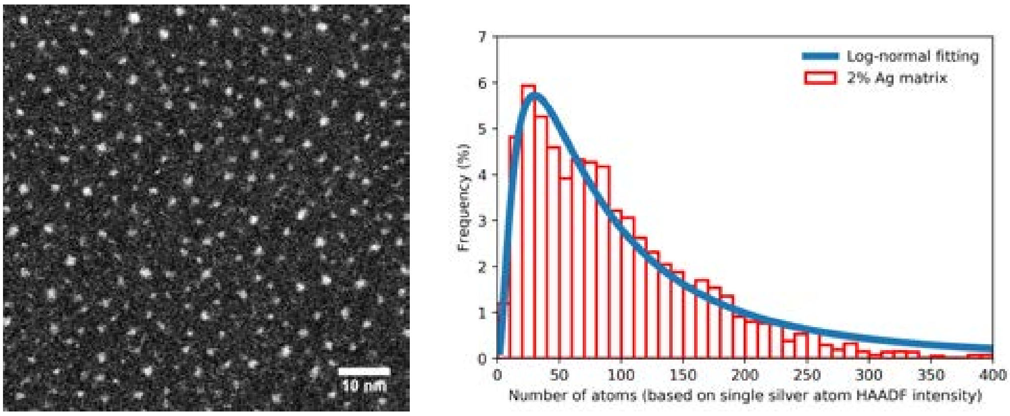

Fig. 4.6 (left) STEM image of the Ag clusters deposited on a TEM grid. (right) The Ag clusters size distribution follow a typical log-normal curve with a peak distribution of 30 atoms and an average size of 80 atoms.

The cluster flux is characterised by the number of clusters landing onto the TEM grid per unit of area per μA of incident ion during the sputtering per second. In these experimental conditions, it is equal to $7\ clusters/(\mu m^2 \cdot \mu A \cdot s)$, which corresponds to a cluster current of $30nA$ on the total area of the slide if one considers the clusters as singly charged nanoparticles. Indeed, $\frac{7\,clusters}{(\mu m^2 \cdot \mu A \cdot s)}$ corresponds to:

$$\frac{7 \cdot 25 \cdot 75 \cdot 10^6\,\mu m^2 \cdot 15\,\mu A \cdot e}{(\mu m^2 \cdot \mu A \cdot s)} \approx 30\,nA$$

where e is the electronic charge, $25 \cdot 75 \cdot 10^6\,\mu m^2$ is the area of the slide and $15\,\mu A$ the sputtering ion beam current.

4.3.2 Gold clusters

The production of gold clusters is achieved using an evaporator at a temperature of $1450°C$ providing the necessary conditions to reach a metal concentration in the matrix of 1% with a standard argon pressure of $4 \cdot 10^{-6} mbar$. The temperature of the matrix support during deposition is $20K$, which guarantees solidification of the argon. While sputtering the matrix with the experimental parameters for the ion beam as listed previously, the clusters are

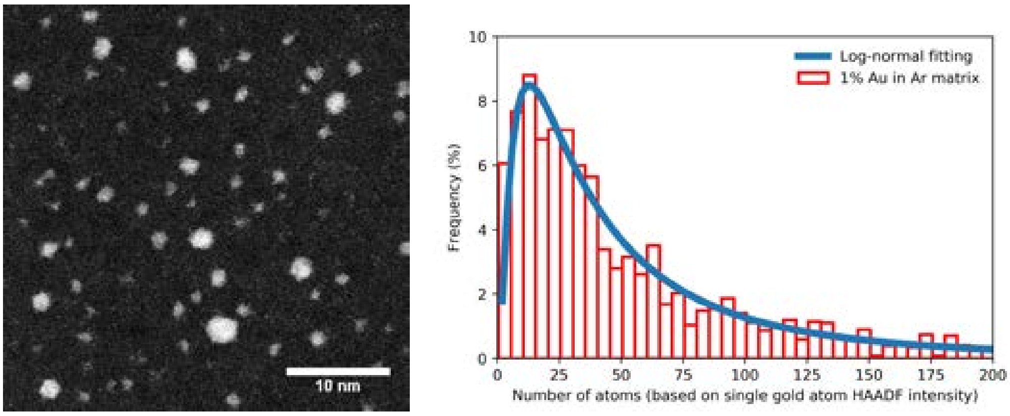

Fig. 4.7 (left) Example of a STEM image of the Au clusters deposited on a TEM grid. (right) The size of Au clusters follows a typical log-normal distribution with a peak distribution of 15 atoms and an average size of 40 atoms.

collected onto the TEM grid and the carbon tape. A HAADF STEM image of the gold clusters is shown in figure 4.7 as well as their size distribution. According to the log-normal fitting, the gold clusters exhibit a peak distribution around 15 atoms with an average cluster size of 40 atoms. The cluster flux is determined averaging the number of clusters per unit of area based on more than 20 STEM images from two different batches of production and is approximatively 4.5 $clusters/(\mu m^2 \cdot \mu A \cdot s)$. The corresponding cluster current is $20nA$.

4.3.3 Binary clusters

We demonstrate here the possibility to produce binary clusters with the MACS 2. The cryogenic matrix is built while using simultaneously an evaporator loaded with gold and an e-beam evaporator containing a palladium rod. The experimental parameters such the ion beam current, the beam energy and the deposition time are kept the same as previously for the purpose of comparison. Instead of considering the number of atoms, since the ratio of gold and palladium atoms is undetermined and varies from one cluster to another, we express the size of the cluster as an area, which is subsequently converted into a volume assuming that the nanoparticles are spherical. The volume distribution of our binary Au-Pd clusters is

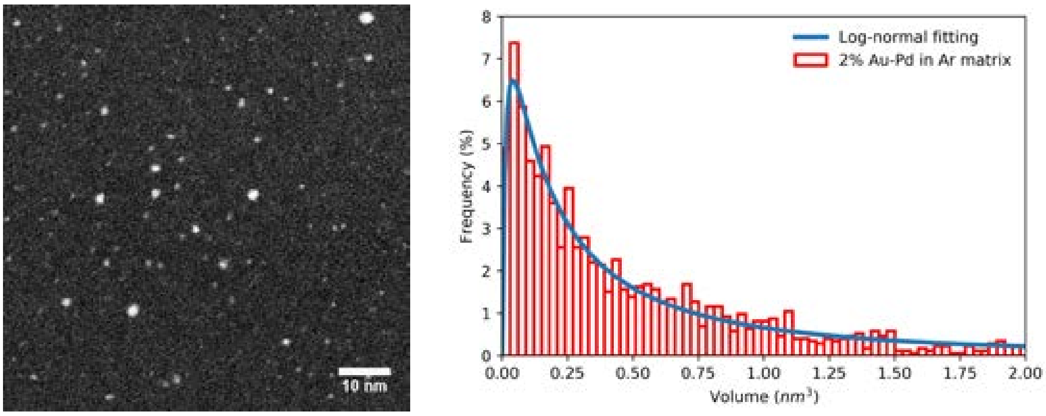

Fig. 4.8 (left) Example of a STEM image of the Au-Pd clusters deposited on a TEM grid. (right) The volume of Au-Pd clusters follows a typical log-normal distribution with a peak distribution corresponding to $0.3nm$ of diameter. The average diameter of those binary clusters is around $1nm$.

shown in figure 4.8 and exhibits a peak distribution which corresponds to a diameter of $0.3\,nm$ with an average cluster diameter of $1\,nm$. The cluster flux is extrapolated from our STEM measurements and is estimated to be around 3.5 $clusters/(\mu m^2 \cdot \mu A \cdot s)$. The corresponding cluster current is around $15\,nA$. EDX measurements are performed to demonstrate that both gold and palladium made up the nanoparticles as seen in figure 4.9. The high energy electron beam is therefore focused on a small area on the sample where a cluster is located. It ejects some of the inner shell electrons of the atoms it encounters, leaving holes for higher energy level electrons to drop down to. During that process, an X-ray photon with an energy equal to the gap separating the two levels is emitted. The difference between two energy levels depends on the electronic structure of the material present on the sample, i.e. the chemical element. Therefore this technique enables to determine the composition of a sample. Our measurements are performed on the largest clusters to maximise the count of X-ray emitted. Indeed a distinctive peak at $2.8keV$ characteristic of the Pd atoms is observed on the Au-Pd samples and is absent from those where only gold clusters are deposited. Peaks at $1keV$,

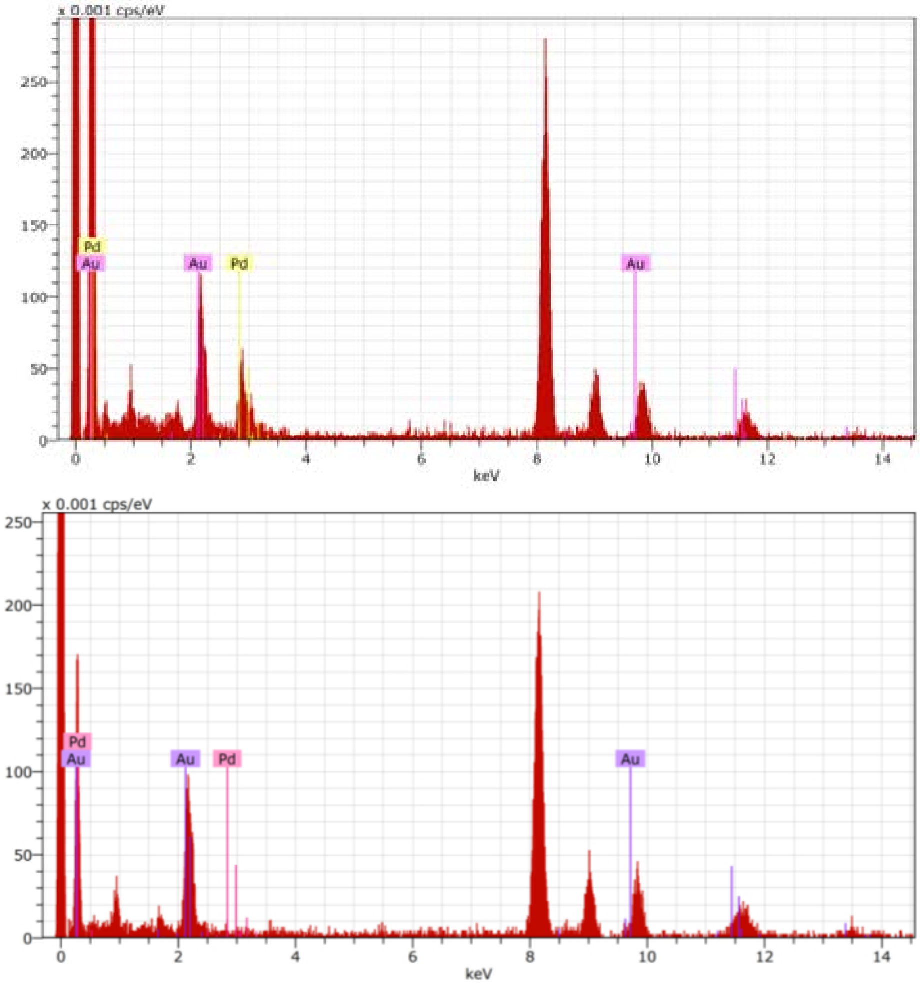

Fig. 4.9 EDX spectroscopy measurements on both the Au-Pd samples (top) and Au samples (bottom). The distinctive peak at $2.8 keV$ for the Pd atoms is missing on the lower graph as expected.

$8keV$ and $9keV$ are from Cu atoms as it is what composes the TEM grid[2]. As the matrix metal loading is composed of 50% Au atoms and 50% Pd atoms (see table 4.1), we can assume that the clusters generated are in average made of such a ratio.

4.4 Characterisation of the powder

4.4.1 Weight loading

Once the deposition is achieved and the topmost layer of the graphite tape is scrapped off using a scalpel, the powder is weighted. $0.8g$ of powder was collected for an area of $150cm^2$. As we know the cluster current I_c, the average size of a cluster S_{av} and the deposition time t_d, it is possible to determine the respective mass of metal m_d deposited onto the powder using the following relation:

$$m_d = \frac{I_c \cdot S_{av} \cdot t_d \cdot N_s \cdot A_w}{e \cdot N_A} \tag{4.1}$$

where $N_s = 8$ is the number of slides, A_w the atomic weight of the metal considered, e the charge of one electron and N_A is the Avogadro constant. We deduced that $19\,\mu g$ of Ag and $12\,\mu g$ of Au were deposited giving a weight loading on the powder of $0.0024wt\%$ and $0.0015wt\%$ respectively. In the case of our $Au-Pd$ clusters, one needs to consider the number of atoms per cluster and a $1:1$ ratio in number of atoms. The average volume of the gold palladium clusters can be calculated from the distribution and its corresponding diameter is $1.7nm$. A $1.7nm$ metal particle is around 110 atoms [101], which leads to a mass of metal on $0.8g$ of powder of $\approx 19\,\mu g$. The corresponding weight loading is therefore $0.0024wt\%$.

---

[2] For the values, refer to the program or equipment manual or search for EDX periodic tables online for the most common de-excitations.

4.4.2 STEM images of the catalyst powder

To determine whether the clusters on the graphite tape correspond to those observed on TEM grids, various imaging techniques such as AFM and STM were employed but were unsuccessful. This is attributed to the nanometric size of the cluster and the poor conductivity of the graphite flake in the case of the STM. Instead, the powder was dispersed into deionised water and sonicated for 10 minutes. The solution containing the topmost layers of graphite was then dropcasted onto a TEM grid and dried in air. The first downside of this technique is that many sub-layers have detached from the flake in this process, hence the majority of the microscopic sheets observed on the TEM grid with the STEM do not have clusters on them. The second inconvenience is that this technique can increase the mobility of the clusters on their support and therefore the sintering. Despite the fact that this task is comparable to finding a needle in a haystack, some clusters resting on their carbon support were imaged demonstrating the existence of the clusters on the tape (see figure 4.10). There are two ways of determining whether the clusters sintered or not, comparing the size distribution or the apparent cluster flux. The latter is the method chosen as poor quality images due

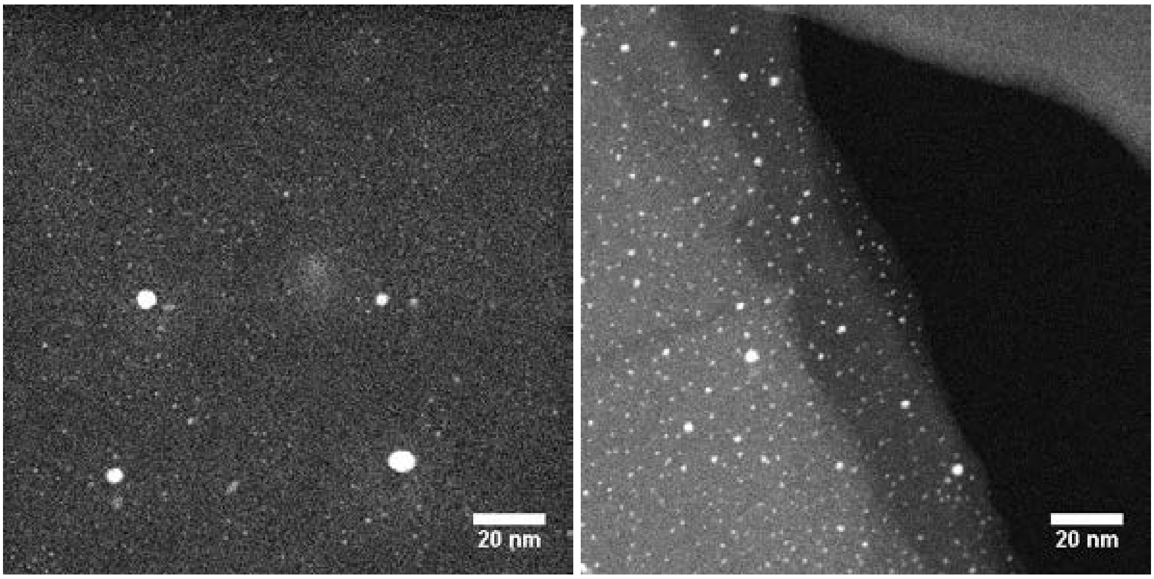

Fig. 4.10 STEM images of silver clusters (left) and gold clusters (right) resting on carbon sheets after being dropcasted from a deionised water solution onto holey carbon TEM grids.

to contamination and abrupt changes in the background thickness due to the presence of multiple flakes stacked on top of each other would alter the estimation of the cluster HAADF intensity. Indeed, as one can see a white zone has formed on the centre of the left image, giving away the presence of contaminations gathering where the sample was imaged at higher magnification. Whereas the silver clusters seem to have sintered as the apparent cluster flux drops to 2 $clusters/(\mu m^2 \cdot \mu A \cdot s)$ and bigger particles can be observed, the gold clusters have maintained their original form as they are in equal number per unit area as those deposited on the TEM grid. This demonstrates that gold clusters deposited on the carbon tape can be studied independently on TEM grids as both studies lead to similar results. In the case of the silver samples, we conclude that the clusters might move, sinter and have their number of atoms tripled in average despite the existence of defects on the surface. This result is in agreement with studies performed on size-selected silver clusters deposited on sputtered graphite with sizes of 50, 185 and 250 atoms, all diffusing and agglomerating in much bigger particles [102]. Work done by Rongsheng Cai[3] shows that Pd-Au clusters produced in the same conditions as those described here display a similar size distribution (within a $\pm 0.5nm$ error) demonstrating that no sintering takes place for the binary clusters on the graphite support.

4.5 Performance of the catalyst powder

4.5.1 Production efficiency

The deposition of clusters on 8 successive glass slides while rotating the carousel would normally take a day of work considering the time required to cool down the system (2 to 3 hours), the construction of a cryogenic matrix (80 minutes) and the deposition on 4 glass slides (60 minutes), where both last steps are repeated twice to cover a total area of 8 glass

---

[3] "Directly deposited preformed palladium clusters on graphite supports for selective hydrogenation of 1-pentyne" to be published.

slides corresponding to $150cm^2$. The average powder produced for 8 slides is $0.8g$ with a metal loading of around $10-20\mu g$. In comparison, such a deposition with the magnetron cluster source would take weeks as the cluster current is typically around $100pA$ [103]. This is more than 2 orders of magnitude lower than the one achieved for metallic clusters with the MACS 2, which is typically around $20-30nA$. Although the comparison can seem unfair as the clusters are size selected with the magnetron cluster source, the cluster size distribution from the MACS is relatively narrow as hardly any clusters of more than 300 atoms are produced limiting the size of cluster much below $3nm$.

4.5.2 CO oxidation

In order to demonstrate that our sample production method is suitable for catalysis, we chose to test the catalytic activity of our metal cluster loaded powder on the CO oxidation as a model catalytic reaction. As previously described in section 1.2.2, the CO oxidation can be enhanced by the substrate and the nanoparticles separately, and the nanoparticles can be modified by, or act with their support, which enhances the reaction. Here we will focus solely on studying the activity of different metal nanoparticles on the carbon support. Inert supports, such as SiO_2 or graphite as we show later in the text, are good choices to see whether the metal clusters are catalytically active or not [12]. The review detailed in section 1.2.2 demonstrates that our measurements are done not only on the adequate metals but also in a close to ideal range of sizes to observe catalytic activity. For the purpose of a comparison with published results, our nanoparticles must be regarded as spherical entities of around one or two nanometres of diameter deposited on a carbon substrate.

4.5.3 Catalytic results

The catalytic activity characterisation of our catalyst powder was conducted at Johnson Matthey and performed by Rongsheng Cai in their vapour-phase chemical reaction facility.

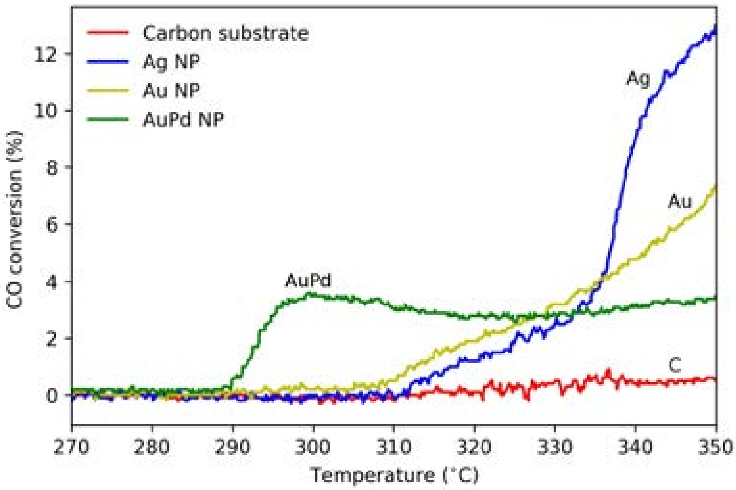

Fig. 4.11 Conversion of the CO oxidation as a function of the temperature for the blank graphite sample and diverse metal nanoparticles deposited onto the carbon support.

The instrument is composed of a tube furnace, in which $0.2g$ of the catalyst is held in its centre and through which the gas passes. Valves regulate the controlled flow rates. A mixture of CO and O_2 in a $1:20$ ratio and mixed with 79% helium is used. The temperature is ramped up at $5°C$ per minute. The conversion rate of CO molecules as a function of the temperature is shown on the figure 4.11 for the diverse samples. We can see that the graphite support is catalytically inert and that the highest catalytic activity is achieved with the silver sample, whereas the binary clusters start to react at a slightly lower temperature. All samples are catalytic active in the range of conditions explored. The fact that the activity arises at high temperature results from the lack of pretreatments and the choice of the support, as oxide metals are usually favoured for this particular reaction. The poor conversion can be explained by the very weak concentration of metal particles in the furnace. One of the factors that can explain the different behaviour of the curves is the sintering of the particles onto the substrate as the temperature increases their mobility or induces the migration of single atoms from one cluster to another. Indeed, at $250°C$, ripening was reported for this particular reaction on size-selected Au nanoparticles deposited on TEM grids [104].

4.6 Conclusion

In this chapter, we demonstrate the successful building of a cluster source called the MACS 2 and the ability to produce various metal clusters. We demonstrated the possibility to form binary metal clusters with the MACS for the first time. Thanks to the carousel implemented in the deposition chamber, a large area was unlocked to deposited the clusters onto. In one day, $0.8g$ of powder made of metal nanoparticles loaded onto the graphite support can be produced. Coupled with test tube chemistry and STEM imaging, we were able to characterise the clusters. Nanometric Ag, Au, and $Au-Pd$ clusters were produced at clusters current of $30nA$, $20nA$ and $15nA$ respectively. We also demonstrated their catalytic activity for the CO oxidation. Even though metal oxides supports are preferable as they provide oxygen and bring down the activation energy, favouring the reaction, we still observed catalytic activity for all samples. This confirms our hypothesis regarding the applicability of the MACS clusters for catalysis. The fact that all clusters have sizes comprised in the ideal size range of around 1 to 2 nanometres for this particular reaction is a major advantage. The low conversion is explained by the low metal nanoparticles concentration. Of the studied nanoparticles, the binary $Au-Pd$ clusters display the best results as the reaction starts at the lowest temperature. These observations led to the production of many more batches of catalyst powder containing Au, Pd and $Au-Pd$ nanoparticles used for the selective hydrogenation of 1-pentyne by Rongsheng Cai and demonstrated the very good quality of the catalyst in comparison with Pd reference sample synthesis by traditional wet impregnation[4].

---

[4] Rongsheng Cai's thesis, to be submitted.

Chapter 5

Linear and nonlinear optical properties of AuNP embedded in a PSi layer at $2.5\mu m$

5.1 Introduction

Because of its dominant role in electronic devices, its abundance on earth and the facility to process and modify it, silicon has been given great attention in the field of optoelectronic. Since 1990, new methods have been developed to produce porous silicon and investigate its unique physical properties [105]. The broad spectrum of possible applications for this high surface to volume ratio material with intrinsic quantum confinement properties captured the imagination of scientists all around the world. This has led to over a thousand publications per year across various domains of applications as shown in figure 5.1. The most widely researched domain for porous silicon is energy conversion. Solar cells in particular make good use of porous silicon because of its anti-reflection properties in the visible range [107] and its enlarged band-gap in comparison with that of bulk silicon. In the pharmaceutical world, porous silicon has also become an attractive choice for biomedical applications since

Fig. 5.1 Current broad application areas of porous silicon under evaluation. Applications are arranged by the dominant physical form of porous silicon required. On the left-hand column, applications require primarily powders, on the right-hand column primarily chip-based layers. The central column applications utilize all three dominant forms: powders, membranes, and films. Figure and caption from [106].

Canham demonstrated its biomedical activity in vitro [108]. Moreover, it was found that binding organic molecules in the pores of the nanostructured silicon changes its refractive index, paving the way to engineering biosensors [109]. In communication systems, modulators are required to transform light into a meaningful signal as it is best sometimes not to meddle with the laser source itself. Therefore, this technology relies on fast and strong changes of optical properties of the modulating material. Park et al. showed that porous silicon membranes can exhibit a 50% transmitted light modulation in the mid-infrared spectrum by the means of optical excitation [110]. Nanometric planar silicon structures have also shown great results with a $94\,\%$ change in transmission at $1.5\,\mu m$, achieved at beam energies as low as $25\,pJ$ [111]. Beyond the genuine intellectual curiosity, the creation of novel silicon based nanocomposites with enhanced linear and nonlinear optical properties, whether they are in the visible or infrared range, is of great commercial interest for optical modulating and switching devices [112]. Indeed, electronic transistors have modulated and switched electronic signals in computers for decades and current efforts are made to replace these by optical compounds to increase the energy-efficiency and the speed of chip-based devices [113]. These new technologies are also of interest in sensors and the tunability of the material over a great range of frequencies is key for its success on the market [114]. Fekete et al. [115] demonstrated in 2005, that thin silicon layers can change their reflective properties for terahertz frequencies from anti-reflective to highly-reflective just by increasing the number of free carriers in the material. Similar results have been reported in infrared when changing the temperature of the material [116]. However, it should be noted that the time response of the material when modifying its temperature is found to be much greater than when modifying its carrier population.

In this work, we investigate and characterise the optical properties of embedded gold nanoparticles in highly mesoporous silicon layers at $2.5\mu m$ wavelength based on reflectometry and ultrafast time-resolved pump-probe spectroscopy measurements.

5.1.1 Optical properties of nanocomposites

One method to develop a physical compound with unique optical properties is to combine different materials together and form a composite at a nanoscopic scale. Such a medium has linear and nonlinear optical properties that differ from those of either of its constituents. It appears homogeneous as the scale of its structure is much smaller than the wavelength of the light used to probe it, allowing the description of its optical features by the means of linear effective optical constants. Effective medium approximations, such as Maxwell Garnett mixing rule described in section 2.2, enable us to predict desired linear optical features and support experimental work. Percolated, layered or randomly dispersed mixtures must be treated distinctively and described by different physical models [117]. Indeed, the arrangement of the constituents matters greatly as isotropic and anisotropic materials are characterised by very different mathematical object, i.e. a single dielectric constant and a dielectric tensor respectively. Nonlinear properties of the newly formed material are equally dependant on its architecture. For example, work by Sipe and Boyd [118] devoted to the determination of the nonlinear susceptibility of composite optical materials in the Maxwell

Garnett model predicted that there exist conditions under which the nonlinear properties of the composite might be larger than those of its individual constituents. Also, experimental work based on percolated glass filled with nonlinear fluids showed enhanced nonlinear optical response [119]. As there is an infinite number of possible combinations of materials and arrangements, both theoretical and experimental work are essential to shine light upon this vast and recent field of study. This study will investigate the optical properties of composites made of gold nanoparticles embedded in porous silicon layers at $2.5\,\mu m$. Adding gold could potentially enhance weak linear and nonlinear optical properties of porous silicon.

5.1.2 Optical properties of gold inclusions

The field of effective medium theories started in 1904, when Maxwell Garnett [58] successfully explained the colour of glasses containing various volume fractions of metal particles and correctly predicted the position of absorption peaks in the visible spectrum. In fact, the vast majority of optical studies carried out on gold nanoparticles are focused in the visible range where plasmon resonances occur. The resonance frequency of spherical gold nanoparticles (hence, having an aspect ratio around 1) is known to be around $520\,nm$ [120]. In 1992, Foss et al. [121] prepared composite membranes made of arrays of gold nano-cylinders in porous alumina. They reported that their experimental studies on spherical and needle-like gold particles were very much in agreement with simulated absorption spectra using the 3D and 2D Maxwell Garnett mixing rules respectively. This gives credit to the importance of shape and orientation of particles for the determination of the effective optical properties of the composite in the visible range. Two years later, in the same vein of their previous work, they observed a blue shift of the absorption peak when the aspect ratio of the particle increases and also when its diameter shrinks. Both observations were in qualitative agreement with the Maxwell Garnett theory modified to address size and shape effects [59]. These results were later confirmed by Hornyak et al. [122], adding that no shift of the absorption peak is observed for particles of 15 nm diameters and smaller, regardless of the particle's shape. Interestingly, in 1999, Link and El-Sayed published spectral studies of surface plasmon electronic oscillations in gold nanorods [123], demonstrating the existence of two absorption peaks in the visible spectrum of light and simulated them as shown in figure 5.2. According to their findings, the absorption peak blue-shifting for increasing aspect ratio (left peaks in figure 5.2) is associated with a transversal oscillation mode. A second one, red-shifting with larger aspect ratios (right peaks), corresponds to the longitudinal electronic resonance.

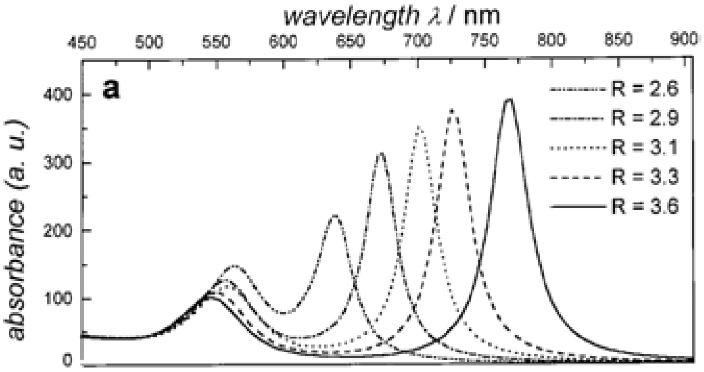

Fig. 5.2 Simulation of the surface plasmon absorption for gold nanorods of different aspect ratio. The graph shows the calculated absorption spectra of gold nanorods with varying aspect ratios R. Figure and caption from [123].

We understand here that the strong anisotropy of a sample is invisible when the probing light is s-polarised as its electric field is oriented along the transversal direction of the nanorods only. On the contrary, the anisotropic nature of the medium must be considered when the light is p-polarised or a combination of both polarisation. In that case the dielectric constant of the material is written $\varepsilon = (\varepsilon_x, \varepsilon_y, \varepsilon_z)$. This was successfully demonstrated by Atkinson et al. when they quantified the dielectric tensors of composites made of gold nanorods embedded in alumina [124]. In all the studies mentioned, the use of Maxwell-Garnett mixing rule enabled to successfully describe and locate absorption peaks, justifying their shift as a function of the aspect ratio of the nanocylinder but has failed to quantify the intensity of the resonance phenomenon. This has been attributed to electron confinement. As at least one dimension of the particles is smaller than the typical mean free path of the electrons in the bulk material, their collective behaviour is spatially limited.

Gold particles display distinctive features on carrier processes. When exciting gold particles in an aqueous medium with high power ultra short pulses of light of wavelength close to their plasma resonance frequency, a large proportion of the light is absorbed by the conduction electrons. These electrons are excited to higher energy states within the conduction band and are referred to as "hot" electrons. Relaxation processes can be quantified and identified when recording the time dependence of the optical response of the probe signal after excitation. It is reported that these hot electrons thermalise rapidly through electron-electron relaxation, subsequently followed by a $2.5\,ps$ lifetime electron-phonon relaxation [125]. Lattice relaxation occurs at times greater than $50\,ps$. As the material goes back to its ground state over time, it recovers its optical properties in equilibrium. Different relaxation times are observed depending on the size of the particle but also on its surrounding material, as inter-media electron-phonon and phonon-phonon interactions most likely occur. This becomes transparent when comparing studies of similar gold nanoparticle sizes in different hosts. Gold particles in a SiO_2 matrix have a electron-phonon relaxation time of $2.8\,ps$ [126], $7\,ps$ in water and $3.5\,ps$ in a cyclohexane solution [127].

Nonlinear properties of gold nanoparticles have also been extensively studied in the visible range. For particles embedded in membranes or in solutions, nonlinear transmission measurements are carried out using a technique called z-scan. Z-scan is the measurement of the transmission light through the sample as a function of the light intensity. The light is focused using a convex lens placed before the sample. By changing the position of the sample along the axis of the propagation, the intensity at the detector varies due to the altered focus position in regards to the sample. Optical nonlinear coefficients can be estimated while fitting the intensity dependence transmittance using nonlinear equations. Studies based on this technique have demonstrated high nonlinearities for gold nanoparticles incorporated onto europium oxide films [128]. Strong third order nonlinearities near the plasmon resonance frequency have also been shown [128]. Philip et al. [129] reported the intense size-dependence of gold nanoparticles nonlinearities. Z-scan measurements on 15-atom gold clusters have demonstrated an order magnitude enhancement of the nonlinear properties of the gold clusters once in contact with indium tin oxide. Interestingly, Neira et al. [74] showed that composites made of gold nanorods embedded into a nanoporous Anodic Aluminum Oxide structure displayed third order nonlinearities of much higher intensities than those of either constituents and reported that the experimental conditions for the highest nonlinear parameters were obtained when the material had its dielectric constant ε near zero (ENZ). They concluded that the nature of the nonlinearity can vary depending on the combination of the strength, the angle and the wavelength of the light. Additionally, as the sign of the real and imaginary nonlinear parameters can change, focusing or defocusing nonlinearities and induced absorption or transparency are optical properties that can be tuned by engineering the architecture of the nanocomposite.

In summary, it can appreciated that the vast majority of research on the optical properties of gold nanoparticles focuses on the plasmon resonance frequency occurring in the visible range. However, very little effort has been made so far to create nanocomposites and investigate their linear and nonlinear optical properties around the effective plasmon resonance of the composite, which can be located outside the visible spectrum depending upon its host material and the direction considered.

5.1.3 Optical properties of porous silicon nanostructures

In 1990, Canham [105] described a novel electrochemical dissolution method to dig vertical voids in silicon wafers, leaving behind free standing silicon wires. This research not only opened the route for a simpler way of producing mesoporous structures than by the means of epitaxial growth or lithography, it also provided evidence that these structures exhibit red photoluminescence when excited with high intensity green or blue laser light. It is important to remember that luminescence is absent from Si bulk because of its indirect band-gap. In 1997, a review of the field by Cullis et al. [130] highlighted the correlation between the width of the wirelike silicon arrays and the wavelength of the light emitted. It is thought that quantum confinement is responsible for the occurrence of luminescence in the porous structure. Later, Wolkin et al. [131] corroborated that the energy of the light emitted increases with decreasing sizes, also, the quantum confinement modifies band structures and enlarges the band-gap and the passivation of the surface changes the luminescence colour.

Regarding the determination of the refractive index of a porous structure, as previously stated, the model chosen to describe the material can vary depending on its geometry, porosity and the wavelength at which the measurements are performed. The linear optical properties of various porous silicon layers, exhibiting different void-matter volume ratios, were studied using ellipsometry and reflectometry across the entire visible range down to mid infrared wavelengths [132]. The effective refractive index was quantified and found to steadily decrease with greater void volumes. Simulations based on Bruggeman's effective mixing approximation showed good agreement with experimental data in the visible range but discrepancies emerged in the infrared due to the presence of oxides. More recently, Wolf et al. [133] determined the refractive index of 30% porous silicon and demonstrated that Bruggeman's model would fit well in the visible range whereas Maxwell-Garnett would take over in infrared.

The mechanisms behind carrier excitation and relaxation in porous silicon were described in brief in section 2.3.1. Femtosecond pump-probe techniques have recently given evidence that both Auger and SRH recombinations take place in porous silicon, with their respective dominance depending on the wavelength of the probe. Fourier transform infrared spectroscopy measurements have helped to determine that Auger recombination dominates the picture at certain wavelengths due to the activation of vibrational modes of molecular impurities at the surface of the pores, making the Auger recombination phonon-assisted [134]. In this study, the enhancement of the Auger recombination rate is reported to be three orders of magnitude higher than that of bulk silicon.

In 1995, z-scan measurements performed at $665\,nm$ on n-type porous silicon membranes showed a high and positive n_2, over two order of magnitude above that of bulk silicon [135]. A two photon absorption process in the porous silicon structure was identified. Additionally, the possibility to use such a material as an all-optical switcher was demonstrated, as the absorption of a $815\,nm$ light drastically drops when the material is exposed to a $650\,nm$ pump beam. The reason is that the major part of the electrons from the ground state, which are responsible for the absorption of the probe, are suddenly excited to an intermediate state by the pump. Interestingly, Lettieri et al. also showed high nonlinear refractive coefficients calculated from z-scan measurements on 80% porosity of p-type porous silicon, however, negative at all wavelengths studied ($532\,nm$, $737\,nm$ and $1064\,nm$). The two-photon absorption and Kerr coefficients of silicon were thoroughly studied in the wavelength range of $850 - 2200\,nm$ using the z-scan technique by Bristow et al. in 2007 [136]. The measurements were performed on a thin silicon wafer of $125\,\mu m$ thickness. The value of the Kerr coefficient n_2 and the two-photon absorption coefficient β were fluctuating between 3 and $12 \cdot 10^{-14}\,cm^2/W$ and between 0.25 and $2\,cm/GW$, respectively, across the spectrum studied. Using pump-probe spectroscopy in transmission at a $1550\,nm$ wavelength for both the pump and the probe, Suess et al. [137] and Apiratikul et al. [138] confirmed a value for the Kerr coefficient of $n_2 = 6.7 \cdot 10^{-14}\,cm^2/W$ and a value for the two photon absorption coefficient of $\beta = 1\,cm/GW$ for a 70% porous silicon, demonstrating a close correlation between the porous structure and the bulk. However, a recovery time for the carriers in the porous silicon is estimated around $10ps$, which is two orders of magnitudes less than in bulk silicon according to their study.

5.2 Pump-probe experimental setup

Ultrafast time-resolved pump-probe reflection measurements are presented in this work and were conducted using a femtosecond pump-probe technique shown in figure 5.3. The pump, used to create a perturbation in the medium of interest, is a p-polarized monochromatic light, exhibiting a central wavelength of 800*nm*. The probe, used to study the linear and nonlinear optical properties of the sample, is an s-polarized 2.5μm wavelength. They both have a repetition rate equals to $1kHz$ and a pulse duration $\tau = 65fs$.

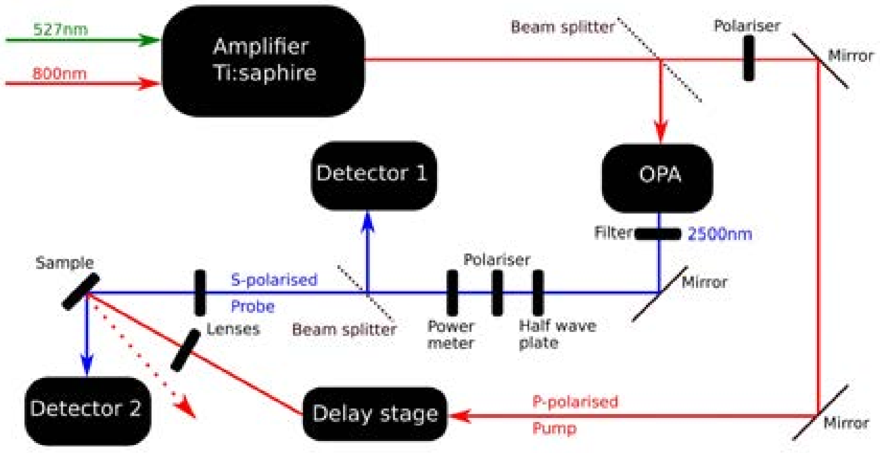

Fig. 5.3 Simplified schematic of the pump-probe experiment setup and its most important constituents.

The system is composed of different units generating the two beams, which are briefly described here. A $Ti:saphire$ cavity amplifies an incoming 800*nm* wavelength ultrafast short seed pulses. The beam exiting the amplifier is a femtosecond laser beam of 2.8W of intensity. It is then split with the help of a beam splitter. 5% of the beam is transmitted and polarised. It is used to pump the samples. The reflected part is diverted towards an optical parametric amplifier (OPA) capable of converting the 800*nm* input laser into near-infrared pulses, which we used to probe the sample. The exiting signals are then filtered to ensure that only the 2.5μm with a spectral width of 100*nm* propagates through. It is consecutively re-directed into a half wave plate and a polariser. To choose the intensity of the probe, one rotates the half-wave plate and measures the power of the light P_{av} exiting the polariser using a powermeter. The optical path length of the pump is modified using a computer controlled retroreflector (or delay stage). This changes the time at which the pump reaches the sample, enabling the study of the sample's response to the probe before, during and after perturbation. Prior to this, however, the beams must spatially overlap on the sample and this is guaranteed using IR card and a CCD camera sensitive to the $800nm$ pump. The incident angle of the probe and the pump are 20° and 30°, respectively. Both pump and probe are focused on the sample with lenses. The beam profile is measured using a scanning slit placed in front of a detector and its width and area A are estimated from the full width at half maximum of the Gaussian profile. The peak intensity is calculated by the following ratio $P_{av}/(\tau \cdot f \cdot A)$, where f is the frequency of the pulse. The reflected probe beam is collected by a 2.5 μm *PbS* ThorLab photoconductive detector connected to a lock-in amplifier. Another detector is placed prior reflection to monitor and smooth fluctuations in the beam intensity. The intensity of both detectors is recorded using a LabView based program.

Both beam profiles are measured by placing a thin slit where the samples would normally rest and scans across while collecting increments of the beam light in a closely placed detector. The beam diameter is then given by the full width of the beam at half of its maximum intensity (FWHM) of the fitted Gaussian as depicted in figure 5.4. Taking into account the angle made with the sample and the projection of the beam, the probe area was $0.34 \pm 0.06mm^2$ and the pump area was $0.82 \pm 0.17mm^2$. The error is estimated considering a $\pm 5mm$ error on the position of the slit in regards to the exact position of the sample. It is important that the pump beam area is larger than the probe beam area for a uniform excitation.

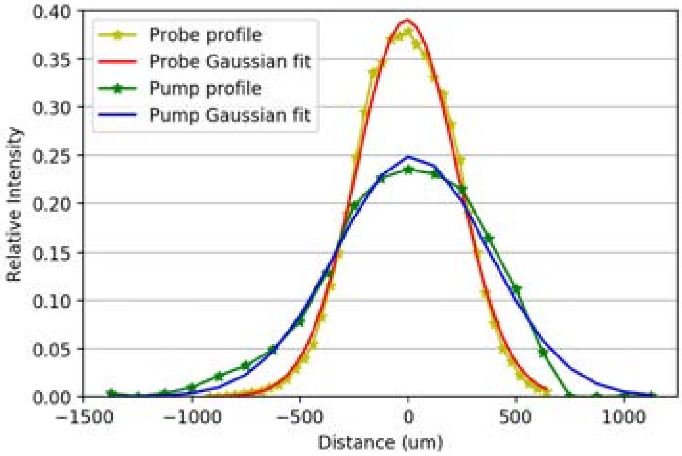

Fig. 5.4 The beam profiles for both the pump and the probe are measured and fitted using a Gaussian curve. The diameter of the beam corresponds to the full width at the half maximum intensity of the curve. $\Phi_{probe} \approx 640\mu m$ and $\Phi_{pump} \approx 950\mu m$, leading to an area of $0.34 \pm 0.06mm^2$ for the probe beam and an area of $0.82 \pm 0.17mm^2$ for the pump.

5.3 Gold nanoparticles embedded in porous silicon layers

5.3.1 Fabrication of the samples

Porous silicon (PSi) samples were prepared by electrochemical anodization of a boron-doped Si wafer. The resistivity of the silicon doped is $5 - 20m\Omega \cdot cm$, which corresponds to a doping density of $3 \cdot 10^{24} m^{-3}$. A 1 : 1 ratio mixture of methanol and 40% hydrofluoric acid was used as the electrolyte at a current density of $100mAcm^{-2}$ for $8s$ to yield a layer with a thickness of approximately $630nm$ (measured by scanning electron microscopy). A 65% porosity is estimated using gravimetric analysis on membranes produced under similar conditions. The pores size is approximately a few tens of nanometres. The wafer was rinsed in methanol, dried and kept in air. With time, a native oxide layer developed on the surface of the sample and inside the pores. To refresh the layer and remove the thin silicon oxide layer, the wafer was dipped in a 2% of HF solution diluted in DI water for 30 seconds only and immediately rinsed in DI water afterwards. Adding this step has demonstrated better impregnation of gold nanoparticles in the pores.

We have investigated both physical and chemical methods to introduce gold in the silicon pores. Accelerating charged metal clusters or ions generated inside the magnetron cluster source towards a high voltage biased PSi samples was tested in our laboratories. Various voltages were tried from $1keV$ to $5keV$ and led in all cases to the clogging of the pores and the formation of a film. Similar results were also published by Lenshin et al. [139]. Electrodeposition [140] is the most efficient technique to fill very low aspect ratio silicon mesopores (pores of $2-50nm$ diameter) and macroporous ($> 50nm$ diameter) silicon with metals. It should be mentioned that the method works better on larger pores and a pore tip is required for the reaction to take place initially [141]. However, the equipment needed to perform metal electrodeposition is expensive and the procedure is complex. Instead, we chose to impregnate metal with the electroless immersion plating technique. The modus operandi used for the impregnation of metal in the pores is inspired by that of Nativ-Roth et al. [142]. They demonstrated the spontaneous deposition by immersion plating of metals in the pores of PSi samples, for various concentrations of salt in the solution, leading to nanoparticles of various size inside the porous layer but also on the surface. In order to produce a $0.5mM$ solution of tetracloroauric acid ($HAuCl_4$), $9.85mg$ of the salt were thoroughly mixed in $2.5ml$ of DI and $47.5ml$ of Ethanol in a beaker. To double the molar concentration, one can double the amount of salt in the solution. The solution was placed in a ultrasonic bath for $10min$ to remove air bubbles from both the salt solution and the Di water of the bath. Then the PSi sample was added in the salt solution with the ultrasonic bath to agitate the salt solution and stimulate it to flow inside the pores. After a chosen time period, the sample was rinsed in ethanol and dried on a filter paper in air.

5.3.2 SEM imaging of the samples

All the samples referred to in this chapter are listed in table 5.1 and images taken with a scanning electron microscope are shown in figure 5.5. Images were not all taken on the

Sample	Salt concentration	Immersion time
Au/PSi NC 1	0.5mM	10 min
Au/PSi NC 2	1mM	20 min
Au/PSi NC 3	1mM	120 min
Au/PSi NC 4	1mM	720 min

Table 5.1 List of the nanocomposite samples (NC) formed via electroless immersion plating.

same day and, depending on the status of the instrument, only a certain resolution was achievable. This explains the change in scale and contrast of the images. A secondary electron emission detector was used to gather information from the surface. However, we used the backscattering electron detector in cross section, as the resolution was not optimal to get a clear picture of the embedded nanoparticles. The benefit of the backscattering detection mode is that it gives information in depth, rending a better contrast. However it prevents the determination of the volume fraction of gold. For that purpose, an optical model is developed further in the text. The images illustrate the presence of gold all across the layer for $10 min$, $20 min$, $120 min$ and $720 min$ immersion periods. Naturally we observe that longer immersion times lead to increasing amounts of gold inside and on top of the layer but did not lead to saturation of the surface.

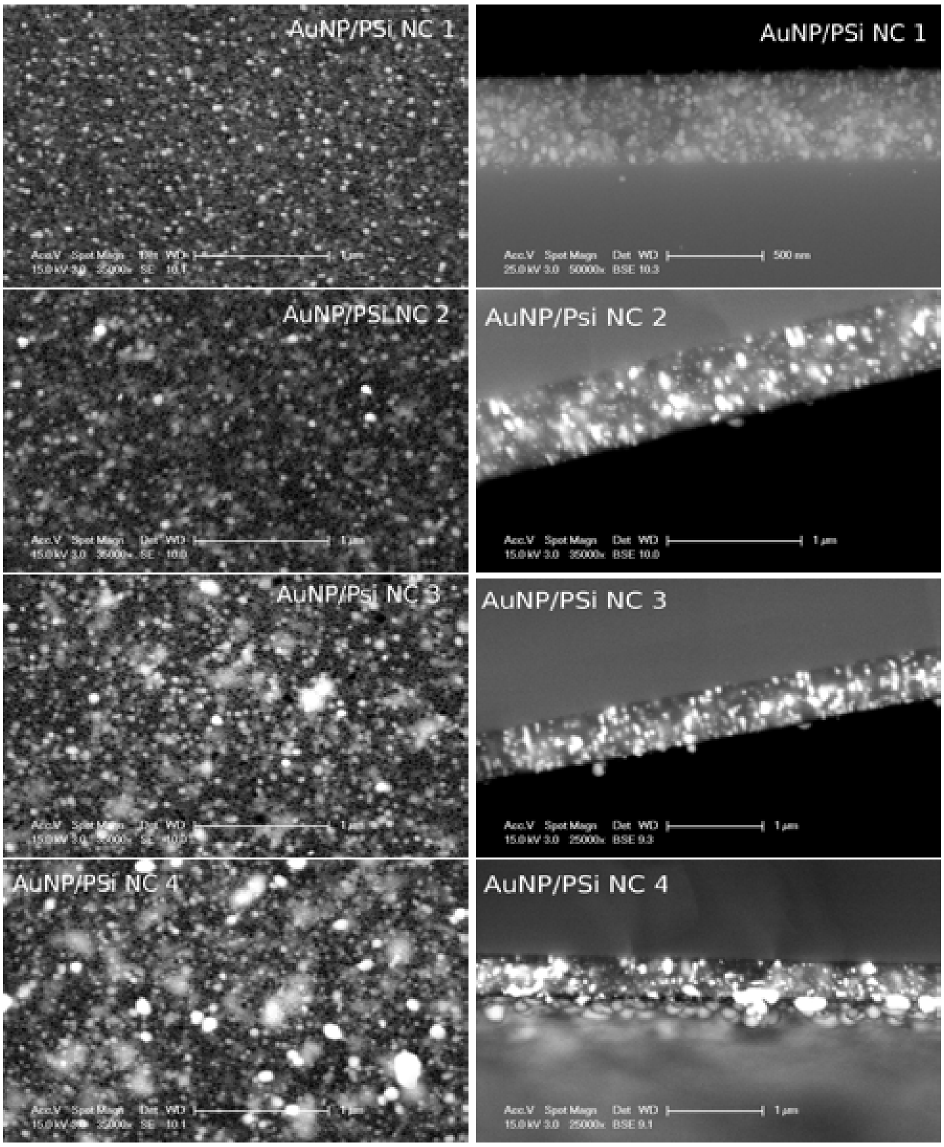

Fig. 5.5 SEM images of the four different samples containing various volume fraction of Au nanoparticles embedded in PSi layers. Top views (Left) of the nanocomposite surface demonstrates the presence of gold nanoparticles in the layer and on the surface without saturating it. Cross section views (right) using BSE detector for better contrast are shown to prove the presence of the gold all across the layers. Dark zones correspond to areas where the pores are empty and grey/white zones are filled or partially filled pores with gold. Increasing deposition time leads to increasing gold volune fractions and greater nanoparticle sizes. The experimental conditions for the formation of the four samples are listed in the table 5.1.

5.4 Reflectometry measurements

In this section, the linear optical properties of the material in equilibrium are investigated using reflectometry. The experimental setup used for our reflectometry measurements is identical to the pump-probe experimental setup as described in section 5.2 except that the pump is blocked and the position of detector 1 is moved around the sample stage as the sample is rotated on its central vertical axis. A schematic is given on figure 5.6 showing a s-polarised probe light incident upon our porous silicon layer filled with gold nanoparticles. The reflected intensity of the beam is measured with the rotating detector 1 and the ratio between the reflected intensity and the incident intensity gives the reflectance. Measurements are collected using both polarisations s and p with a $2.5\,\mu m$ wavelength probe beam in order to gather multiple points and gain resolution when fitting them as shown in figure 5.7. The refractive index of the substrate is determined through the fitting of reflectometry measurements using the mathematical developments elaborated in section 2.1.2 as it is a single interface problem. In the cases of the nanocomposite samples, only the real part of the refractive index of each layer is estimated, the imaginary part being too small to be determined. This is achieved through the fitting of reflectometry measurements using the transfer matrix method elaborated in section 2.1.3 when two interfaces must be considered. Despite ignoring a possible birefringence of the sample, a good fit is achieved and unique value for the refractive index independent of the direction of the propagation of the light is found. Using the two dimensional Maxwell-Garnett mixing approximation with randomly dispersed cylindrical inclusions of gold and silicon in a matrix of air, enables the determination of the fraction of gold and the imaginary part of the refractive index of each layer as listed in table 5.2. It is seen that both real and imaginary parts of the refractive index increase with higher concentrations of gold nanoparticles in the porous structure. From section 2.2, the effective dielectric constant ε_{eff} from the $2D$ Maxwell Garnett mixing rule is related to the volume

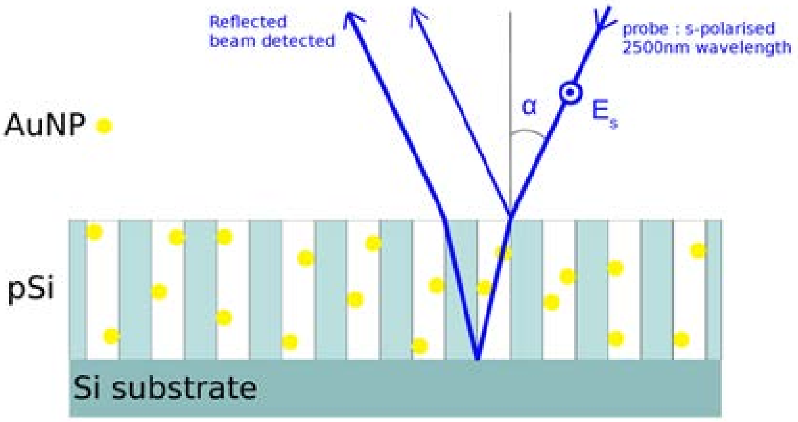

Fig. 5.6 Schematic of the geometry of our reflectometer. The s-polarised 2500 *nm* wavelength light is reflected by both interfaces of the pSi layer embedded with gold nanoparticles. They interfere and build the reflected signal observed on figure 5.7 for various values of the angle α.

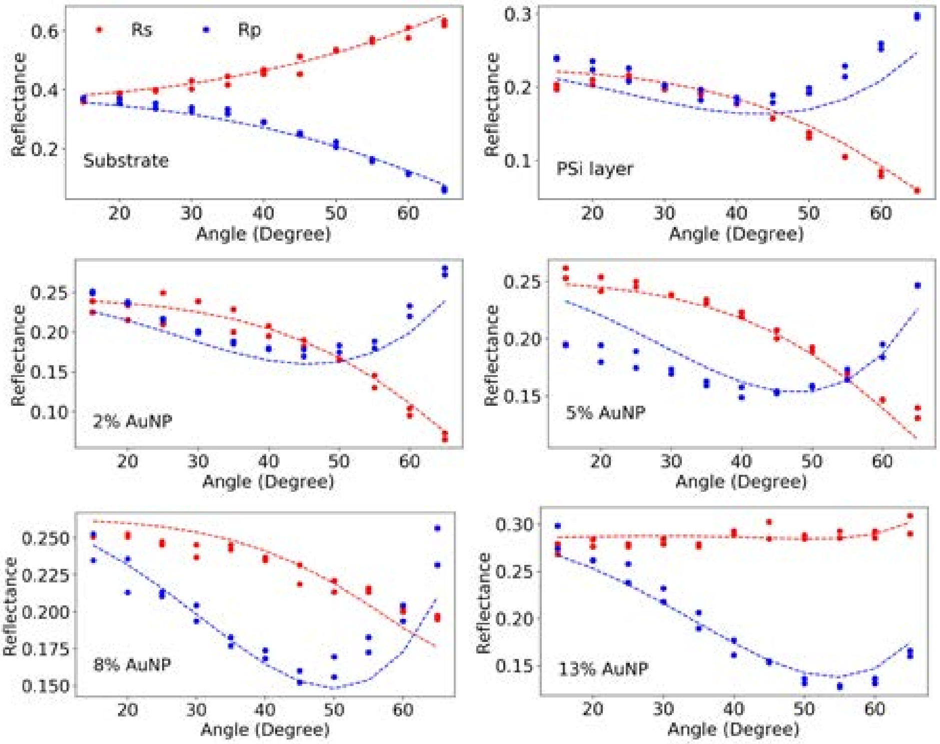

Fig. 5.7 Experimental data and fitting curves of the reflectance versus angle for s and p polarisations. The measurements are carried out on various samples with increasing concentration of gold nanoparticles in the porous silicon layer. The fitting parameters are listed in table 5.2.

Sample	Refractive index	thickness	Au volume fraction
Si substrate	$4.10-0.04i$	$500\mu m$	0%
PSi layer	$1.37-0.001i$	$\approx 630nm$	0%
Au/PSi NC 1	$1.40-0.001i$	$\approx 630nm$	$2\pm 2\%$
Au/PSi NC 2	$1.45-0.001i$	$\approx 630nm$	$5\pm 2\%$
Au/PSi NC 3	$1.50-0.001i$	$\approx 630nm$	$8\pm 2\%$
Au/PSi NC 4	$1.60-0.002i$	$\approx 630nm$	$13\pm 2\%$

Table 5.2 In this table, the real part of the refractive index of each sample obtained from reflectometry measurements is given. The determination of the imaginary part and the gold concentration is established using Maxwell Garnett mixing approximation. The error on the real part is ± 0.3 and is established while fluctuating the range of thickness from $600nm$ to $660nm$, from which the error on the gold volume fraction is deduced.

fraction of the gold f_{Au} via:

$$\frac{\varepsilon_{eff}-\varepsilon_{air}}{\varepsilon_{eff}+\varepsilon_{air}} = f_{Si}\frac{\varepsilon_{Si}-\varepsilon_{air}}{\varepsilon_{Si}+\varepsilon_{air}} + f_{Au}\frac{\varepsilon_{Au}-\varepsilon_{air}}{\varepsilon_{Au}+\varepsilon_{air}} \tag{5.1}$$

with $f_{Si}=0.65$, $f_{air}=1-f_{Au}$, $\varepsilon_{air}=1$, $\varepsilon_{Si}=16.8+0.3i$ (as measured) and $\varepsilon_{Au}=-288.6+14.8i$ [143]. In this study, we consider air as the host since the volume is mostly made of cylindrical void carved in the silicon during the formation of the porous layer. For each volume fraction of gold, an effective dielectric constant can be calculated from the Maxwell Garnett formula. When the effective dielectric constant calculated through the mixing approximation matches the effective dielectric constant obtained from fitting the reflectometry measurements with the transfer matrix method, then the volume fraction of Au is deduced. The formula satisfies the limit conditions for which $\varepsilon_{eff}=\varepsilon_{air}$ when $f_{Au}=f_{Si}=0$ and $\varepsilon_{eff}=\varepsilon_{Si}$ when $f_{Si}=1$. The use of this formula is justified as the volume fraction of the inclusions is inferior to the host volume fraction and that the wavelength of the light incident on the material is significantly bigger than the nanometric structures it encounters [144]. Maxwell-Garnett mixing rule turned out to be the best model to fit experimental spectroscopy measurements in porous silicon mainly because it predicts a refractive index for the 65% porous silicon layer in agreement with the refractive index extracted from the reflectometry measurements. It works even at low porosity [133] and has been utilised and reported as the appropriate model in the case of infrared spectroscopy studies on porous silicon structures [134] [117].

5.5 Time-resolved pump-probe measurements

In this section, the evolution of the refractive index of our samples when generating a free carrier population is investigated and the nonlinear optical behaviour of the samples is observed and characterised. Time-resolved pump-probe measurements are carried out with a p-polarised $800\,nm$ pump and a s-polarised $2.5\,\mu m$ probe using the setup as described in section 5.2. The photon energy of the pump beam is chosen to be higher than the band-gap of silicon: $E_{bg} = 1.14\,eV$. Indeed, reflectometry measurements carried out on porous silicon testing both $540\,nm$ and $1080\,nm$ wavelengths showed that only the former could induce a reflectance change as the latter has a corresponding photon energy of E_{bg}. Since higher energy and momentum are required in an indirect band-gap material, a wavelength of $1080\,nm$ does not generate carriers [145]. Additionally, the band-gap energy increases with quantum confinement as reported previously [131]. The peak intensity expressed in GW/cm^2 of the beam is calculated from the average power P_{av} measured with a power meter by:

$$I_{pump} = \frac{P_{av}}{10^9 \cdot A \cdot f \cdot \tau} \tag{5.2}$$

where the area of the beam on the sample, A, is deduced from the Gaussian beam profile as previously shown in section 5.2, $f = 1\,kHz$ is the frequency of the pulse, and $\tau = 65 \cdot 10^{-15}\,s$ is the pulse duration.

5.5.1 Pump intensity dependence

The main aim of the work presented in this section is to quantify the carrier density when pumping the material at various pump intensities and estimate the effective refractive index of the excited layers.

5.5.1.1 Experimental results

Figure 5.8 shows the time dependence of the transient change in reflectance $(R-R_0)/R_0$ before and after pump excitation for all samples for various pump intensities using a probe intensity of $3.6 GW/cm^2$. Two consecutive repeats were performed and averaged to smooth the signal fluctuations of the probe. From measurements performed under identical conditions at various spots on one sample, an error of $\approx 15\%$ is attributed to the maximum $\Delta R/R_0$ occurring at $\Delta t = 0$. Figure 5.9 demonstrates the evolution of the transient change in reflectance at zero delay time for increasing pump intensities.

Primarly, figures 5.8 and 5.9 demonstrate the significant difference in response between bulk and porous silicon. We observed that the optical properties of the bulk silicon under pumping intensities up to $157 GW/cm^2$ are marginally unchanged. This allows us to ignore the contribution of the substrate when looking at the measurements carried out on the supported layers. Our observations are similar to those of Sokolowski et al. [68] when pumping bulk silicon with a $625\,nm$ wavelength p-polarised light. At a laser fluence of $10 mJ/cm^2$, which corresponds to a power of $157 GW/cm^2$ (as $E(J) = P(W) * t(s)$), they did not observe any noticeable change in the reflectance of the excited silicon. Sokolowski et al. measured that, at such an energy, the electron-hole density is approximatively $10^{26} m^{-3}$ and show that a pump fluence of one order of magnitude higher is required to see major changes in the optical properties of the excited material.

Secondly, it is clear that not only increasing the pump intensity leads to a bigger transient change in reflectance but also that this effect is enhanced by increasing the amount of gold

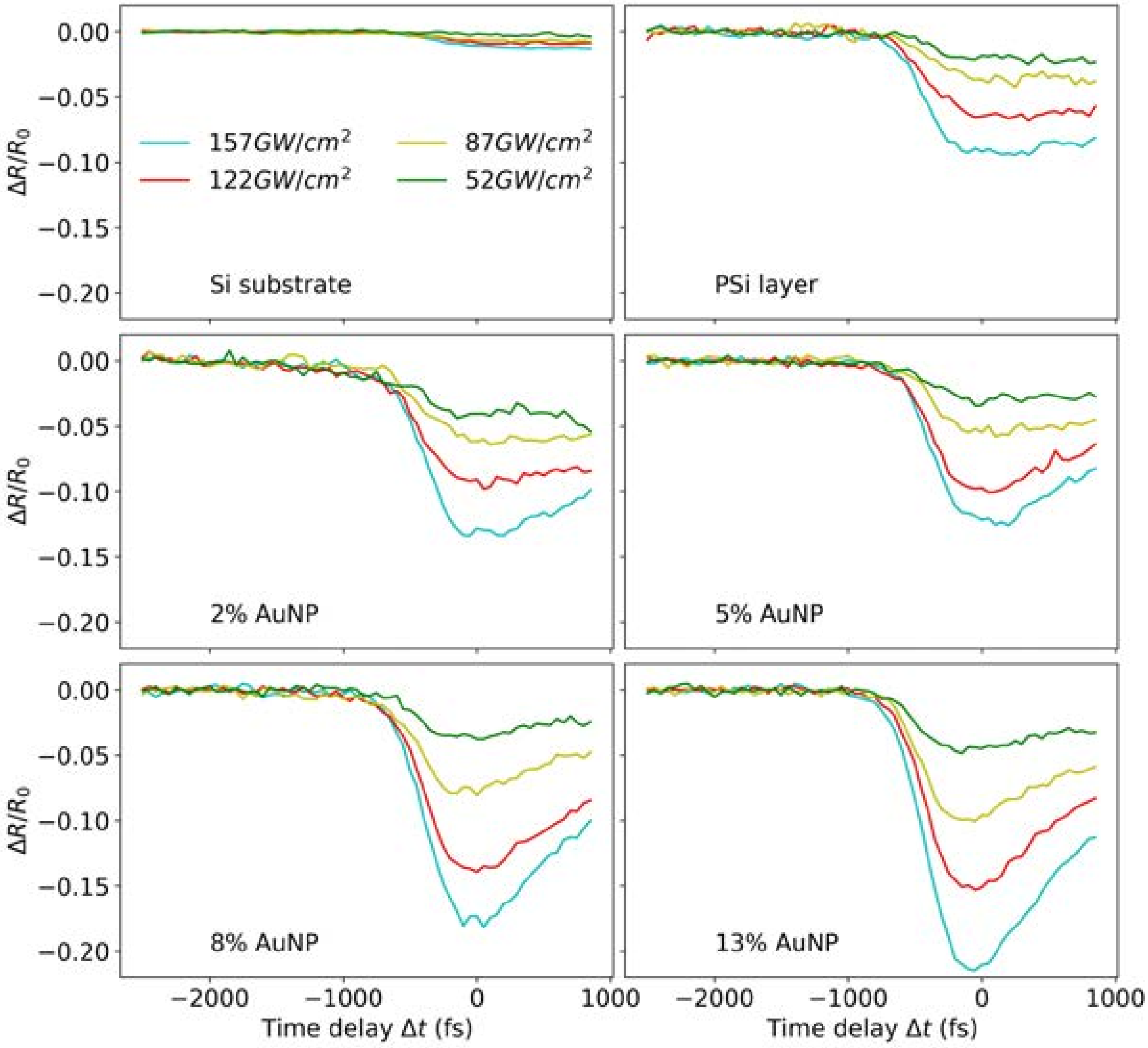

Fig. 5.8 Time-resolved pump-probe spectroscopy of the silicon substrate and various samples with increasing concentrations of gold nanoparticles in the porous silicon layer for four different pump intensities. As seen here, the transient change in reflectance increases with both the gold concentration and the pump intensity.

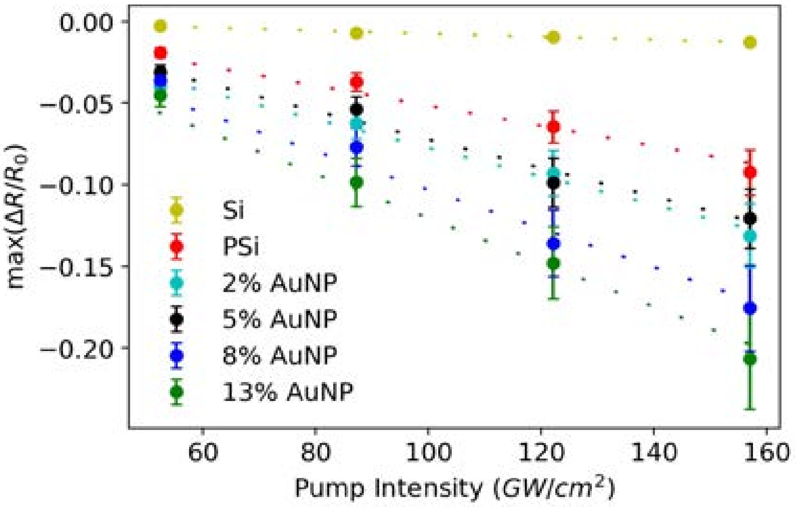

Fig. 5.9 Evolution of the maximum transient change in reflectance occurring at zero delay time as a function of the pump intensity. The silicon substrate and various volume fraction of gold in the porous silicon membrane are investigated. For all samples, we observe that increasing the pump intensity leads to a higher transient change in reflectance at zero time delay and also that increasing the volume fraction of gold amplifies the response. From measurements performed under identical conditions at various spots on one sample, an error of $\approx 15\%$ is attributed to the maximum $\Delta R/R_0$ occurring at $\Delta t = 0$. The maximum $\Delta R/R_0$ is an average of 5 points around the minimum of the experimental curves shown on figure 5.8 in order to smooth the signal fluctuations. The dotted lines are provided as an eye guide.

in the porous silicon layer. As seen in figure 5.9, the drop in reflectance at zero delay time goes from 10% to 20% for the porous silicon layer and the $13\% AuNP$ porous silicon layer, respectively, when pumped with an intensity of $157 GW/cm^2$. Also, when increasing the pump intensity from $52 GW/cm^2$ to $157 GW/cm^2$, the maximum transient change in reflectance ranges from -5% to -20% in the case of the $13\% AuNP$ porous silicon layer.

5.5.1.2 Analysis

An optical model is created to retrieve the carrier density dependence on the pump intensity and the refractive index of the layers. We use the $2D$ Maxwell Garnett mixing approximation as previously done in the case of our reflectometry studies to express the effective dielectric constant of the excited layer $\varepsilon_{ex,eff}$, such as:

$$\frac{\varepsilon_{ex,eff}-\varepsilon_{air}}{\varepsilon_{ex,eff}+\varepsilon_{air}} = f_{Si}\frac{\varepsilon_{ex,Si}-\varepsilon_{air}}{\varepsilon_{ex,Si}+\varepsilon_{air}} + f_{Au}\frac{\varepsilon_{Au}-\varepsilon_{air}}{\varepsilon_{Au}+\varepsilon_{air}} \tag{5.3}$$

where all volume fractions are known. The dielectric constant of the excited silicon $\varepsilon_{ex,Si}$ and the gold ε_{Au} are developed using the Drude model. As developed in section 2.3.2, the dielectric constant for the gold is:

$$\varepsilon_{Au} = 1 - \frac{N_{e,Au}\,e^2}{m_e\varepsilon_0}\frac{1}{(\omega^2 - i\Gamma_{Au}\omega)} \tag{5.4}$$

where $m_e = m_0$ [146], $\Gamma_{Au} = 10^{14}\,s^{-1}$ [147] and $N_{e,Au} = 5.9\cdot 10^{28}\,m^{-3}$ [64]. In metals, the generation of carriers by the pump is assumed to be many orders of magnitude lower than those naturally present in the conduction band. The expression of the dielectric constant of silicon is:

$$\varepsilon_{ex,Si} = \varepsilon_{back,Si} - \frac{e^2}{\varepsilon_0}\left(\frac{N_{dop}}{m_h} + \frac{N_{pump}}{m^*}\right)\frac{1}{(\omega^2 - i\Gamma\omega)} \tag{5.5}$$

where $m^* = 0.17m_0$ [148] is called the reduced optical mass and is given by $m^* = (1/m_h + 1/m_e)^{-1}$, $m_h = 0.36m_0$ [57], $\varepsilon_{back,Si} = 11.7$ [149] and $N_{dop} = 3\cdot 10^{24}m^{-3}$. We understand from equation 5.3 that $\varepsilon_{ex,eff}$ is a function of N_{pump} and Γ_{Si}. Both parameters are yet to be determined. Therefore, we assume that the generation of free carriers occurs only in silicon and that the number of excited electrons in silicon is independent on the volume fraction of gold embedded in the porous silicon structure. This enables us to use all the data points at one particular pump intensity for the determination of the corresponding carrier density. Additionally, we consider that the excitation is uniform in the layer. In order for this to be valid, we must make the assumption that there is no gradient of absorptance in the layer. Therefore, the penetration depth α^{-1} of the probe must be much larger than the thickness of the layer ($630nm$). This is true when $\alpha^{-1} = \lambda_{probe}/(4\pi N_i) > 630nm$, i.e. when $N_i << 0.3$. An iterative program is built to generate a spectrum of possible values for $\varepsilon_{ex,eff}$ and their

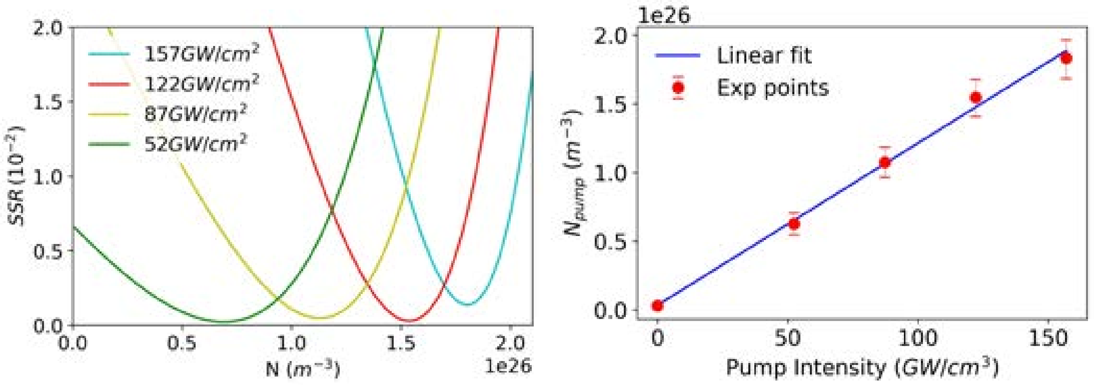

Fig. 5.10 Left: The sum of the squared residuals between measured and simulated transient changes of reflectance at zero delay time is shown in this graph. The solution lays in the minimum of each intensity curve. Right: The solutions from our optical model are presented here and demonstrate that the dependence of the carrier density on the pump intensity is linear. The probe intensity is $3.6 GW/cm^2$.

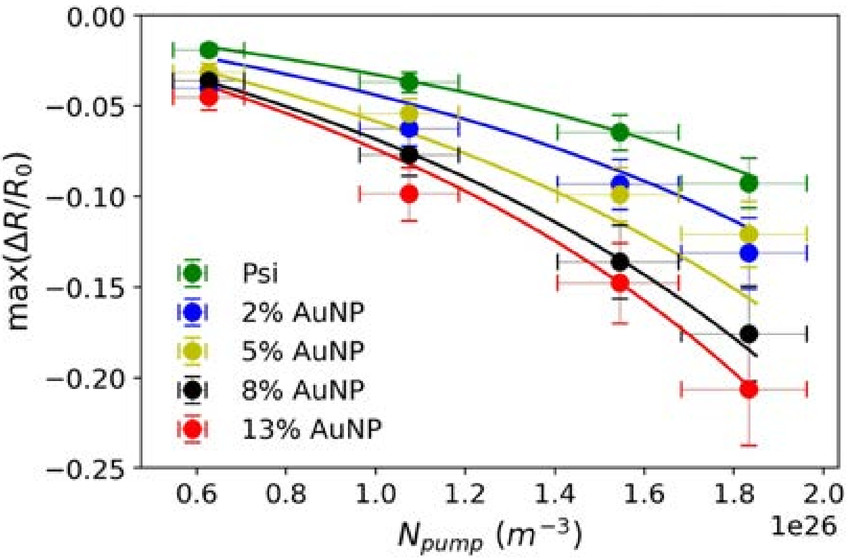

Fig. 5.11 In this graph, we see the evolution of the maximum transient change in reflectance as a function of the carrier density for all 5 layers. The probe intensity is fixed at $3.6 GW/cm^2$. The dots represent our experimental data points and the solid lines represented the simulated values $\Delta R_{sim}/R_{0,sim}$. The best fit is represented here using $\Gamma_{Si} = 6 \cdot 10^{13} s^{-1}$. The horizontal error bars are the incertitude on the carrier density estimated by from the experimental margin of $\approx 15\%$ on the transient change in reflectance at zero delay time, which are respectively represented by the vertical error bars.

respective transient change in reflectance $\Delta R_{sim}/R_{0,sim}$ calculated using the transfer matrix method (see section 2.1.3). As we know the experimental values of the transient change in reflectance (see figure 5.9), the sum of the squared residuals between simulated and experimental values of $\Delta R/R_0$ is estimated and the best N_{pump} and $\varepsilon_{ex,eff}$ can be extracted from the model. The sum of squared residuals as a function of the carrier density is shown in figure 5.10 (left) to demonstrate the existence of a unique solution for each pump intensity. The best fit is found for a relaxation rate Γ_{Si} of $6 \cdot 10^{13} s^{-1}$ in the silicon structure. Moreover, figure 5.10 (right) demonstrates that the carrier density increases linearly with the pump intensity. In figure 5.11, we express the transient change in reflectance at zero delay time as a function of the carrier density estimated via the optical model. The error on the carrier density is calculated considering an experimental margin of $\approx 15\%$ on the transient change in reflectance at zero delay time, as previously stated. The simulated transient change in reflectance (coloured lines) follows closely the experimental results as the transient change in reflectance increases with both the amount of gold and the carrier density. From the optical model, the effective refractive index of the exited layer can be retrieved. Figure 5.12 shows the carrier density dependence of the real (left) and imaginary (right) parts of the refractive index as calculated from the optical model. As the pump intensity goes up, the $2.5\mu m$ light is increasingly absorbed by the material. The imaginary part of the refractive index increases by an order of magnitude between the ground state of the material and the highest excited state tested. It is important to note that N_i stays an order of magnitude below 0.3, which justifies the assumption made to consider the absorptance uniformly across the layer. When we look at the predicted values for the refractive index of our samples in equilibrium, the values fall closely to those obtained from our reflectometry measurements, giving credit to the validity of our calculations. Figure 5.13 shows the evolution of both the real and the imaginary part of the refractive index as a function of a wider range of carrier densities than previously explored in figure 5.12. The trend displayed on this figure is characteristic of a plasmon resonance in the mixed material. It shows that around $4 \cdot 10^{26} m^{-3}$, the peak of absorption described by the imaginary part of the refractive index is at its maximum. It goes from $N_i = 0.95$ for the porous silicon layer up to $N_i = 1.2$ for the $13\% AuNP$ porous silicon layer. This demonstrates that the resonance phenomenon responsible for the increase in absorption is amplified by larger gold concentrations.

5.5.2 Probe intensity dependence

5.5.2.1 Determination of the nonlinear refractive and absorption coefficients

In this section, we look at the probe intensity dependence of the optical response of our samples using a fixed pump intensity of $127\, GW/cm^2$. Figure 5.14 shows that the reflected intensity of a $2.5\, \mu m$ light shone upon our samples prior excitation linearly increases with the incident light intensity, highlighting the linear response of the material in equilibrium in the range of intensities explored. The time-resolved pump-probe spectroscopy measurements carried out on all samples for various probe intensities from 3.6 to $27.1\, GW/cm^2$ are presented in figure 5.15. Three repeats were performed and averaged for each curve. The non-linear optical response of the material is apparent for all layers and negligible in the case of the bare Si substrate. We know that the transient change in reflectance at zero delay time is amplified by the presence of gold nanoparticles as detailed in the previous section. It monotonically decreases with increasing probe intensities in a similar fashion for all samples. Indeed the maximum transient change in reflectance seems to drop by a factor of around 3 for all layers between 3.6 and $27.1\, GW/cm^2$ probe intensities, suggesting that the nonlinear mechanisms behind the optical response of the layers containing the gold are very similar to those of the PSi layer. For example, in the case of the 8% $AuNP$ porous silicon layer, the maximum transient change in reflectance drops from -15% to -5% for probe intensities of $3.6 GW/cm^2$ and $27.1 GW/cm^2$ respectively, as seen in figure 5.15. Therefore, we build an optical model using a single set of nonlinear parameters valid for all samples such as the

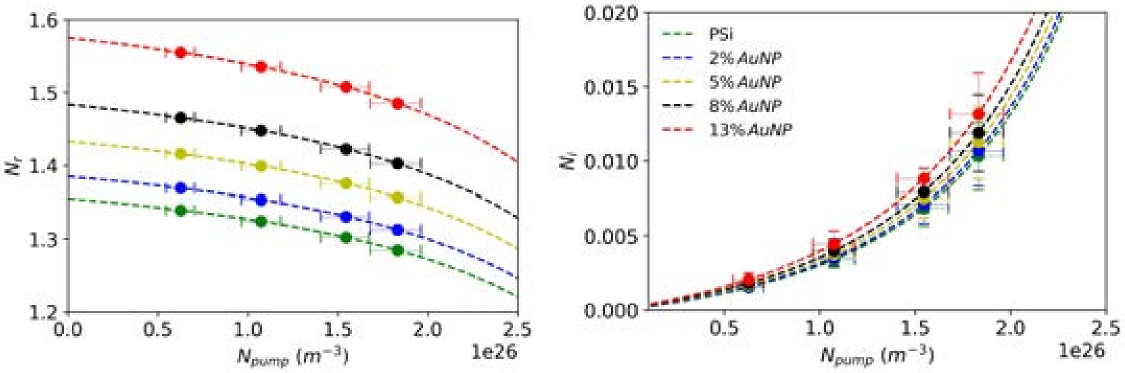

Fig. 5.12 Left: Real part of the refractive index of our layers as a function of the carrier density. The vertical error bars are negligeable as the real part of the refractive index barely changes in the range of excitations explored. Right: Imaginary part of the refractive index of our layers as a function of the carrier density.

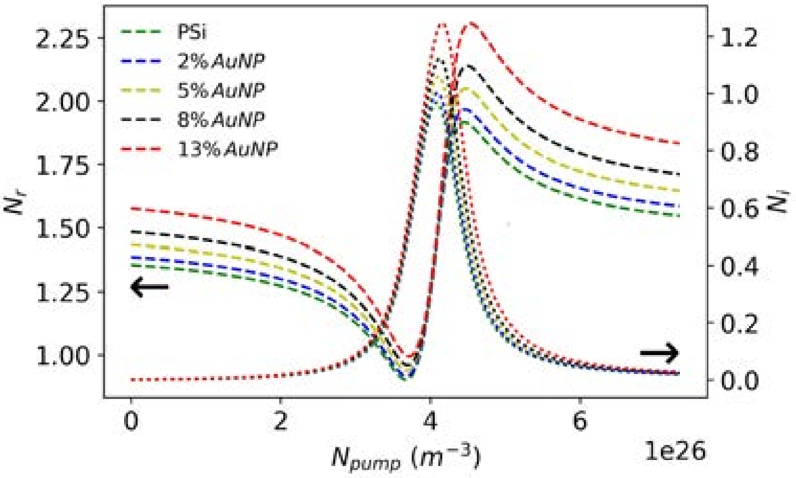

Fig. 5.13 Evolution of the real and imaginary parts of the refractive index of the layer for various concentrations of gold embedded in the porous silicon. The effective plasma resonance of the mixed material occurring at a carrier density of $4 \cdot 10^{26} m^{-3}$ amplifies with increasing amounts of gold.

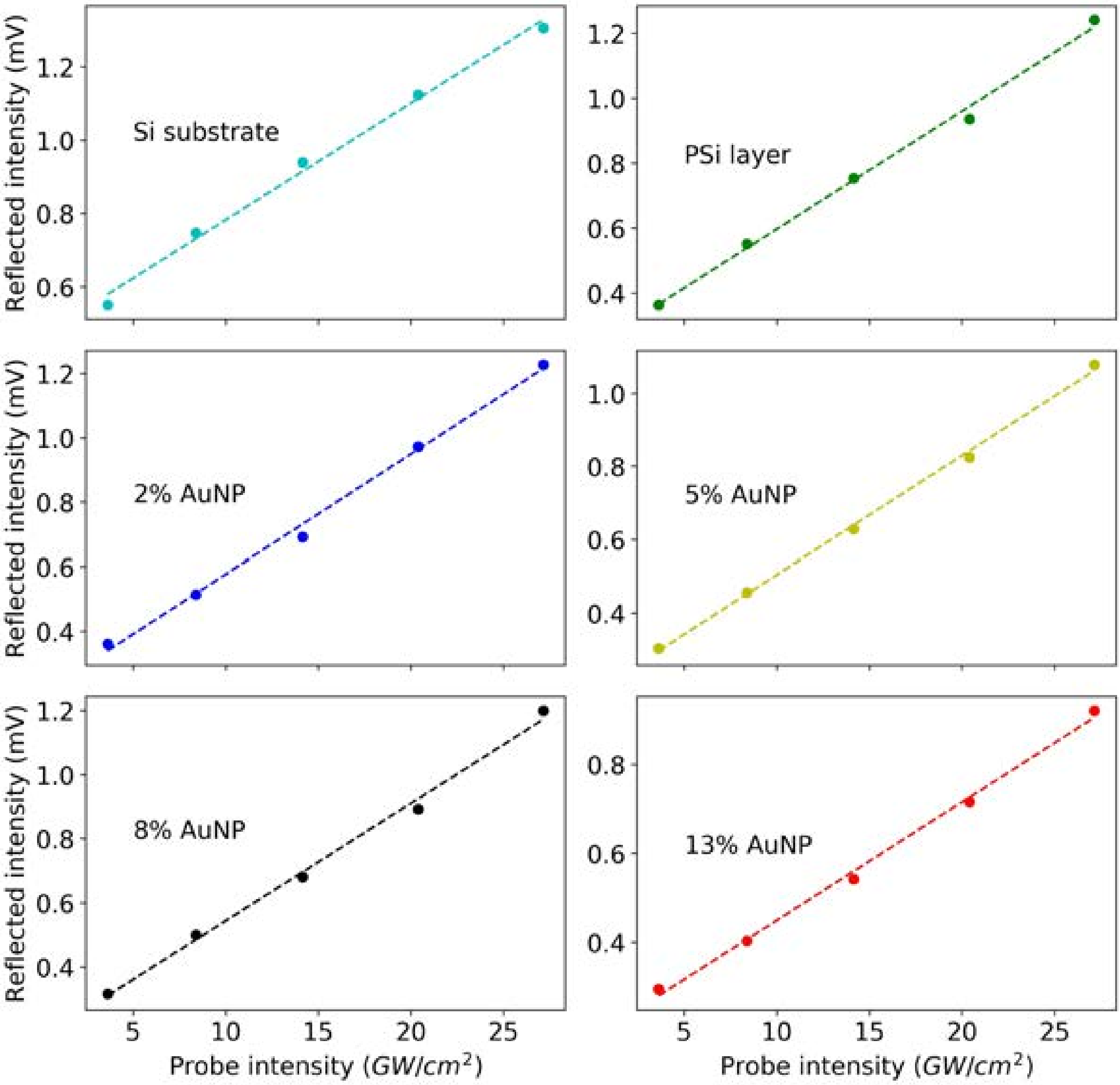

Fig. 5.14 The light intensity collected after reflection on our samples without pump excitation is linearly proportional to the incident light intensity at 2.5 μm.

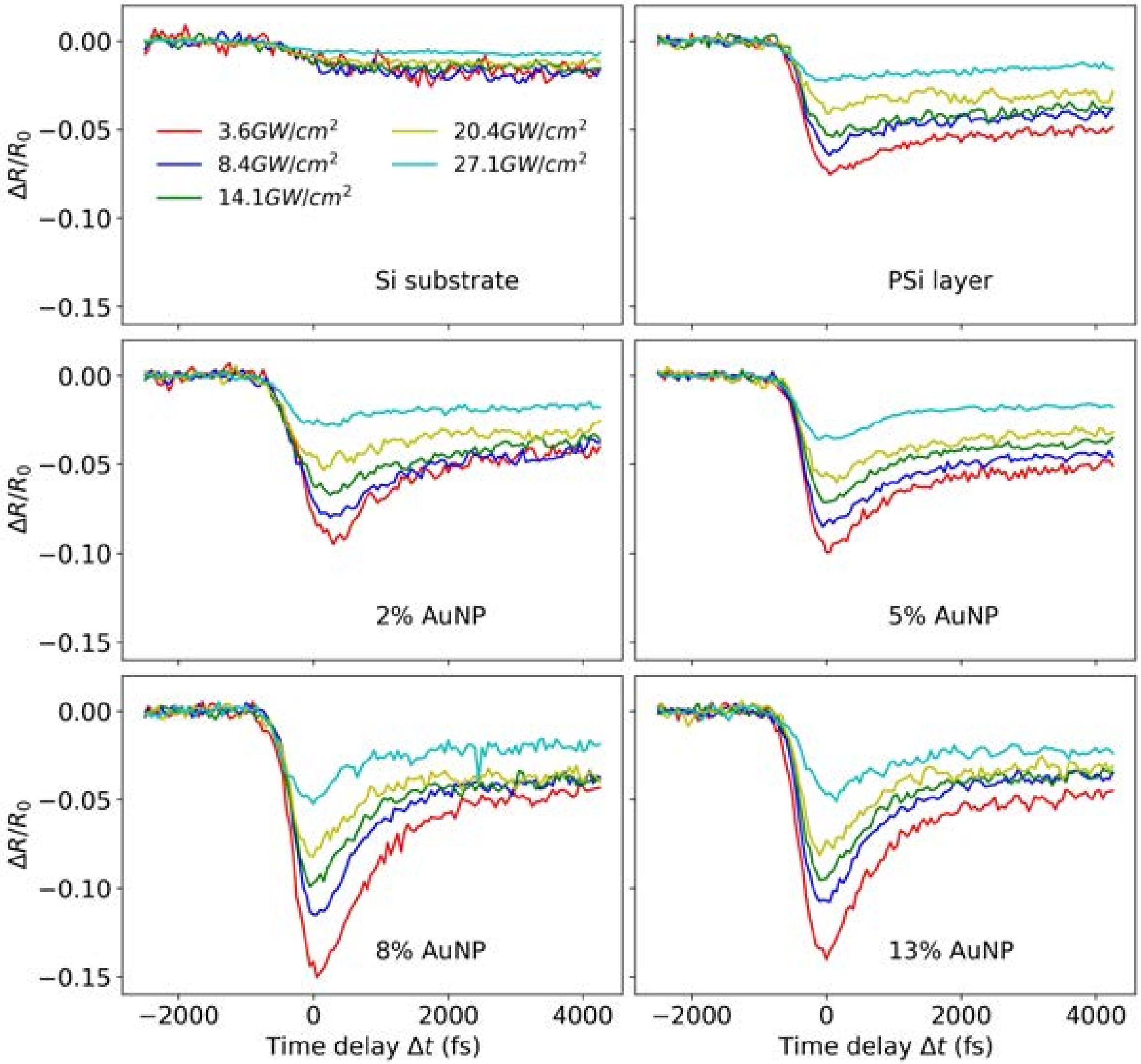

Fig. 5.15 Time-resolved probe intensity dependence of the transient change in reflectance for all samples.

refractive index of a layer $N = n - ik$ at zero time delay is given by:

$$n = n_0 + n_2 \cdot I \qquad and \qquad k = k_0 + k_2 \cdot I \tag{5.6}$$

where n_0 and k_0 are the real and imaginary part of the refractive index of the sample under excitation with a $800\,nm$ light of $127\,GW/cm^2$ intensity. As previously developed in section 2.4, n_2 is the nonlinear refraction coefficient and k_2 is more commonly described through the nonlinear absorption coefficient $\beta = 4\pi k_2/\lambda$. Together, they characterise the amplitude of the nonlinear optical response of the sample as a function of the probe intensity. A map of the sum of the squared residuals is built between the maximum transient change in reflectance experimentally determined for various probe intensities and simulated ones. Simulations are performed using the transfer matrix method introduced in section 2.1.3 and using an effective refractive index of real and imaginary parts based on equations 5.6. n_0 and k_0 were determined in previous section. In the model we consider $n_2 \in [0:4] \cdot 10^{-3}\,cm^2/GW$ and $k_2 \in [-4:0] \cdot 10^{-4}\,cm^2/GW$ as seen in figure 5.16. A unique solution is found giving

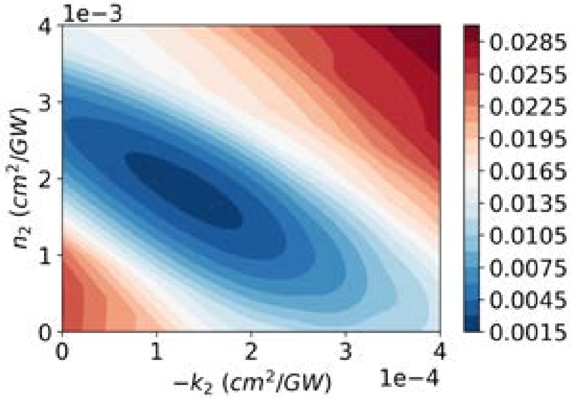

Fig. 5.16 Map of the sum of the squared residuals between experimental and simulated values of the intensity-dependent maximum transient change in reflectance. The solution is found where the sum is minimum, i.e. when $n_2 = 1.8 \cdot 10^{-3} cm^2/GW$ and $k_2 = -1.3 \cdot 10^{-4} cm^2/GW$.

a nonlinear refraction coefficient of $n_2 = 1.8 \cdot 10^{-3} cm^2/GW$ and a nonlinear absorption coefficient of $\beta = -6.5\,cm/GW$. When these values are compared with Bristow's values obtained in the near-infrared for thin silicon wafer, in our case the nonlinear refractive index is two orders of magnitude higher and the nonlinear absorption coefficient is of similar order although it is negative. Figure 5.17 (top) shows the maximum transient change in reflection as a function of the probe intensity (data dots) and the best fit (dashed lines). Figures 5.17 (middle and bottom) show the evolution of the real part and imaginary part of the effective refractive index of the layer as the probe intensity increases. The real part slightly increases and the imaginary part decreases.

5.5.2.2 Discussion

It has been demonstrated that in equilibrium, the nonlinear optical response is negligible. When pumped with a $127\,GW/cm^2$ p-polarised monochromatic beam with a central wavelength at $800\,nm$, nonlinearities appears for all layers. The existence of a unique solution for the nonlinear refractive and absorption coefficients for all layers means that we cannot quantify or observe a modification of the nonlinear optical properties with the addition of gold nanoparticles in the layer. As n_2 is positive and β is negative, the light is self-focusing and induces transparency in the nonlinear excited material when probed at $2.5\,\mu m$. Adding gold not only amplifies the maximum transient change in reflectance but also appear to amplify the relaxation process as the reflectance drops more rapidly with increasing volume fraction of gold. This is illustrated in figure 5.18. It is shown that, when the transient change in reflectance is normalised, the samples containing gold nanoparticles return to their ground state faster than the porous silicon layer.

5.6 Conclusion

In summary, we demonstrate the successful production of gold nanoparticles embedded in porous silicon layers through electroless deposition. Reflectometry measurements are performed at $2.5\,\mu m$ and enables the determination of the effective refractive index for each

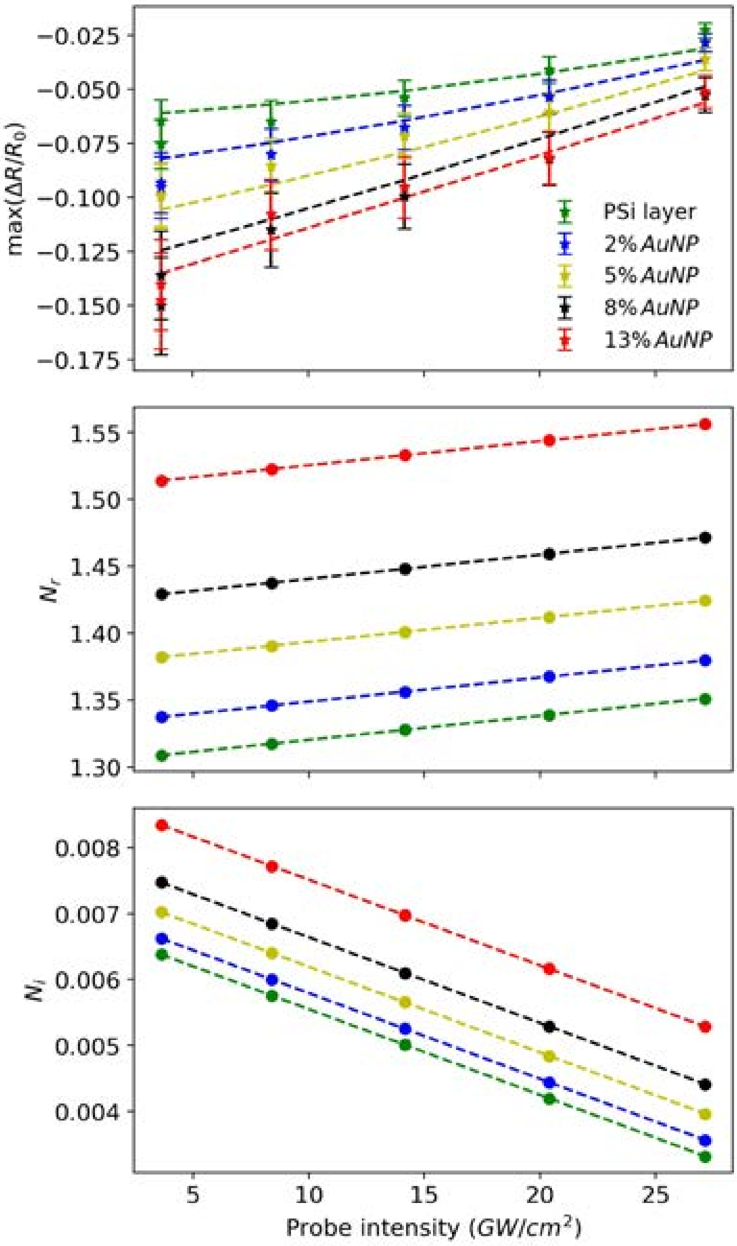

Fig. 5.17 Top: Maximum transient change in reflection as a function of the probe intensity with their respective fit considering a unique solution (dashed lines). Middle: Probe intensity dependence of the real part of the effective refractive index of the layer. Bottom: Probe intensity dependence of the imaginary part of the effective refractive index of the layer.

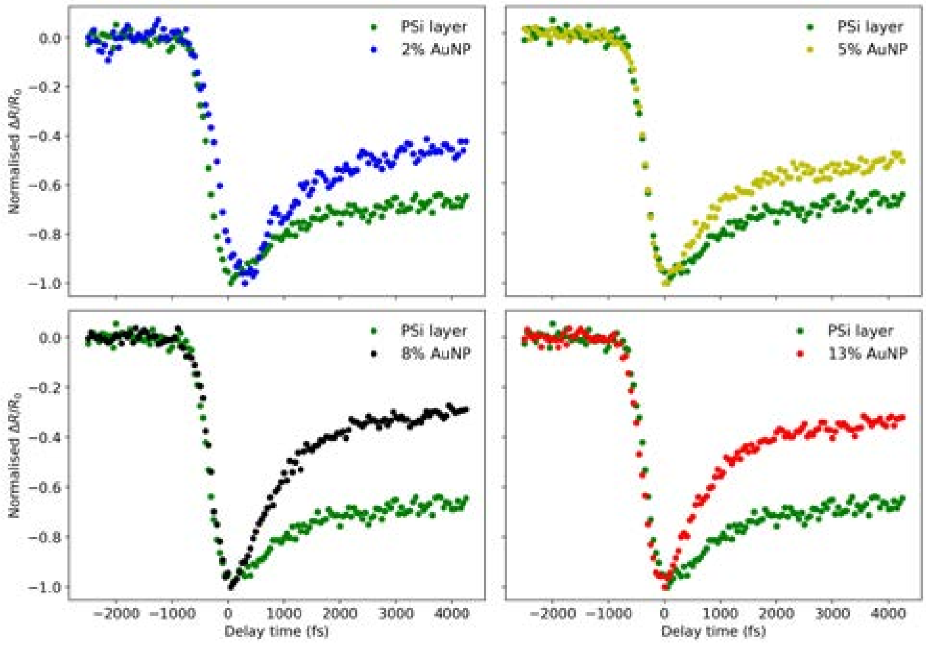

Fig. 5.18 Normalised time-resolved transient change in reflectance for all four gold concentrations compared with the optical response of the porous silicon layer. In all cases, the transient change in reflectance after zero delay time changes faster in the presence of the gold.

layer. Despite the complexity of the mixture, a good fit using the transfer matrix method is achieved without considering the possible birefringence of such a material. The 2D Maxwell-Garnett mixing approximation gives us the possibility to estimate the amount of gold in the layer and predicts correctly the refractive index of the porous silicon layer. The pump-probe reflectance measurements are carried out on each sample varying separately pump and probe intensities. When pumped with a high intensity $800 nm$ laser wavelength, it has been shown that a population of free carriers is generated in the silicon nanostructure and grows linearly with increasing pump intensities. Using the Drude model and our experimental data, the carrier density is quantified and the effective refractive index for each excited nanocomposite is extracted. From the Drude model, it is gathered that our measurements are performed close to the plasma resonance of the material, which explains the increase in absorption as a function of the pump intensity. Probe intensity dependence measurements demonstrate that all material are linear in equilibrium and becomes nonlinear when pumped. A unique solution is found for the nonlinear refractive coefficient $n_2 = 1.8 \cdot 10^{-3} cm^2/GW$ and nonlinear absorption coefficient $\beta = -6.5\, cm/GW$ respectively, suggesting that self-focusing action and induced transparency are taking place for our materials when pumped at $800\, nm$ and probed at $2.5\, \mu m$. Although the gold doesn't participate in the nonlinear behaviour of the nanocomposite, it amplifies the linear optical response and accelerates the relaxation process. In order to gain precision in the quantification of the linear and nonlinear constants of such nanocomposites, we suggest in the future to develop a technique in which metal is introduced in porous silicon membranes so that ultrafast time-resolved pump-probe spectroscopy measurements can be done in reflection and transmission simultaneously. Thin films would also allow z-scan measurements. Indeed, z-scan is widely used for the determination of both nonlinear refraction and absorption coefficients. However, the advantage of our thin supported layers is that they could be considered in our models as uniform and evenly excited when pumped.

References

[1] W. D. Knight, K. Clemenger, W. A. de Heer, W. A. Saunders, M. Y. Chou, and M. L. Cohen, “Electronic Shell Structure and Abundances of Sodium Clusters,” *Phys. Rev. Lett.*, vol. 52, pp. 2141–2143, June 1984.

[2] T. P. Martin, T. Bergmann, H. Göhlich, and T. Lange, “Observation of electronic shells and shells of atoms in large Na clusters,” *Chemical Physics Letters*, vol. 172, pp. 209–213, Sept. 1990.

[3] B. Baguenard, M. Pellarin, J. Lermé, J. L. Vialle, and M. Broyer, “Competition between atomic shell and electronic shell structures in aluminum clusters,” *The Journal of Chemical Physics*, vol. 100, pp. 754–755, Jan. 1994.

[4] O. Echt, K. Sattler, and E. Recknagel, “Magic Numbers for Sphere Packings: Experimental Verification in Free Xenon Clusters,” *Phys. Rev. Lett.*, vol. 47, pp. 1121–1124, Oct. 1981.

[5] B. von Issendorff and R. E. Palmer, “A new high transmission infinite range mass selector for cluster and nanoparticle beams,” *Review of Scientific Instruments*, vol. 70, no. 12, p. 4497, 1999.

[6] U. Heiz, A. Sanchez, S. Abbet, and W.-D. Schneider, “Catalytic Oxidation of Carbon Monoxide on Monodispersed Platinum Clusters: Each Atom Counts,” *J. Am. Chem. Soc.*, vol. 121, no. 13, pp. 3214–3217, 1999.

[7] P. R. Ellis, C. M. Brown, P. T. Bishop, J. Yin, K. Cooke, W. D. Terry, J. Liu, F. Yin, and R. E. Palmer, “The cluster beam route to model catalysts and beyond,” vol. 188, pp. 39–56, July 2016.

[8] G. J. Hutchings, “Metal-cluster catalysts: Access granted,” *Nature Chemistry*, vol. 2, pp. 1005–1006, Dec. 2010.

[9] I. N. Remediakis, N. Lopez, and J. K. Nørskov, “CO oxidation on gold nanoparticles: Theoretical studies,” *Applied Catalysis A: General*, vol. 291, pp. 13–20, Sept. 2005.

[10] M. Mavrikakis, P. Stoltze, and J. K. Nørskov, “Making gold less noble,” *Catalysis Letters*, vol. 64, pp. 101–106, Feb. 2000.

[11] A. Sanchez, S. Abbet, U. Heiz, W.-D. Schneider, H. Hakkinen, R. N. Barnett, and U. Landman, “When Gold Is Not Noble: Nanoscale Gold Catalysts,” *J. Phys. Chem. A*, vol. 103, pp. 9573–9578, Dec. 1999.

[12] M. M. Schubert, S. Hackenberg, A. C. van Veen, M. Muhler, V. Plzak, and R. J. Behm, "CO Oxidation over Supported Gold Catalysts—"Inert" and "Active" Support Materials and Their Role for the Oxygen Supply during Reaction," *Journal of Catalysis*, vol. 197, pp. 113–122, Jan. 2001.

[13] M. M. Schubert, V. Plzak, J. Garche, and R. J. Behm, "Activity, Selectivity, and Long-Term Stability of Different Metal Oxide Supported Gold Catalysts for the Preferential CO Oxidation in H2-Rich Gas," *Catalysis Letters*, vol. 76, pp. 143–150, Oct. 2001.

[14] M. Haruta, S. Tsubota, T. Kobayashi, H. Kageyama, M. J. Genet, and B. Delmon, "Low-Temperature Oxidation of CO over Gold Supported on TiO2, Fe2o3, and Co3o4," *Journal of Catalysis*, vol. 144, pp. 175–192, Nov. 1993.

[15] K. Frey, V. Iablokov, G. Melaet, L. Guczi, and N. Kruse, "CO Oxidation Activity of Ag/TiO2 Catalysts Prepared via Oxalate Co-precipitation," *Catal Lett*, vol. 124, pp. 74–79, Aug. 2008.

[16] M. Valden, X. Lai, and D. W. Goodman, "Onset of Catalytic Activity of Gold Clusters on Titania with the Appearance of Nonmetallic Properties," *Science*, vol. 281, pp. 1647–1650, Sept. 1998.

[17] M. S. Chen and D. W. Goodman, "The Structure of Catalytically Active Gold on Titania," *Science*, vol. 306, pp. 252–255, Oct. 2004.

[18] T. Jiang, D. J. Mowbray, S. Dobrin, H. Falsig, B. Hvolbæk, T. Bligaard, and J. K. Nørskov, "Trends in CO Oxidation Rates for Metal Nanoparticles and Close-Packed, Stepped, and Kinked Surfaces," *J. Phys. Chem. C*, vol. 113, pp. 10548–10553, June 2009.

[19] T. V. W. Janssens, B. S. Clausen, B. Hvolbæk, H. Falsig, C. H. Christensen, T. Bligaard, and J. K. Nørskov, "Insights into the reactivity of supported Au nanoparticles: combining theory and experiments," *Top Catal*, vol. 44, p. 15, June 2007.

[20] J.-X. Liu, I. A. W. Filot, Y. Su, B. Zijlstra, and E. J. M. Hensen, "Optimum Particle Size for Gold-Catalyzed CO Oxidation," *J. Phys. Chem. C*, vol. 122, pp. 8327–8340, Apr. 2018.

[21] I. Stará, V. Nehasil, and V. Matolín, "The influence of particle size on CO oxidation on Pd alumina model catalyst," *Surface Science*, vol. 331-333, pp. 173–177, July 1995.

[22] X. Zhang, Z. Qu, X. Li, M. Wen, X. Quan, D. Ma, and J. Wu, "Studies of silver species for low-temperature CO oxidation on Ag/SiO2 catalysts," *Separation and Purification Technology*, vol. 72, pp. 395–400, May 2010.

[23] W. de Heer, W. Knight, M. Y. Chou, and M. L. Cohen, "Electronic shell structure and metal clusters," *Solid State Physics*, vol. 40, p. 93, 1987.

[24] M. M. Kappes, R. W. Kunz, and E. Schumacher, "Production of large sodium clusters (Nax,.x \leqslant 65) by seeded beam expansions," *Chemical Physics Letters*, vol. 91, pp. 413–418, Oct. 1982.

[25] W. A. de Heer, “The physics of simple metal clusters: experimental aspects and simple models,” *Rev. Mod. Phys.*, vol. 65, pp. 611–676, July 1993.

[26] J. Pedersen, S. Bjørnholm, J. Borggreen, K. Hansen, T. P. Martin, and H. D. Rasmussen, “Observation of quantum supershells in clusters of sodium atoms,” *Nature*, vol. 353, pp. 733–735, Oct. 1991.

[27] C. Binns, “Nanoclusters deposited on surfaces,” *Surface Science Reports*, vol. 44, pp. 1–49, Oct. 2001.

[28] K. Sattler, J. Mühlbach, and E. Recknagel, “Generation of Metal Clusters Containing from 2 to 500 Atoms,” *Phys. Rev. Lett.*, vol. 45, pp. 821–824, Sept. 1980.

[29] S. H. Baker, S. C. Thornton, A. M. Keen, T. I. Preston, C. Norris, K. W. Edmonds, and C. Binns, “The construction of a gas aggregation source for the preparation of mass-selected ultrasmall metal particles,” *Review of Scientific Instruments*, vol. 68, pp. 1853–1857, Apr. 1997.

[30] M. A. Duncan, “Invited Review Article: Laser vaporization cluster sourcesa),” *Review of Scientific Instruments*, vol. 83, p. 041101, Apr. 2012.

[31] T. G. Dietz, M. A. Duncan, D. E. Powers, and R. E. Smalley, “Laser production of supersonic metal cluster beams,” *The Journal of Chemical Physics*, vol. 74, pp. 6511–6512, June 1981.

[32] R. Streubel, G. Bendt, and B. Gökce, “Pilot-scale synthesis of metal nanoparticles by high-speed pulsed laser ablation in liquids,” *Nanotechnology*, vol. 27, no. 20, p. 205602, 2016.

[33] C. Xirouchaki and R. E. Palmer, “Deposition of size-selected metal clusters generated by magnetron sputtering and gas condensation: a progress review,” *Philosophical Transactions of the Royal Society of London A: Mathematical, Physical and Engineering Sciences*, vol. 362, pp. 117–124, Jan. 2004.

[34] H. Haberland, M. Karrais, and M. Mall, “A new type of cluster and cluster ion source,” *Z Phys D - Atoms, Molecules and Clusters*, vol. 20, pp. 413–415, Mar. 1991.

[35] S. Pratontep, S. J. Carroll, C. Xirouchaki, M. Streun, and R. E. Palmer, “Size-selected cluster beam source based on radio frequency magnetron plasma sputtering and gas condensation,” *Review of Scientific Instruments*, vol. 76, no. 4, p. 045103, 2005.

[36] H. Hartmann, V. N. Popok, I. Barke, V. v. Oeynhausen, and K.-H. Meiwes-Broer, “Design and capabilities of an experimental setup based on magnetron sputtering for formation and deposition of size-selected metal clusters on ultra-clean surfaces,” *Review of Scientific Instruments*, vol. 83, p. 073304, July 2012.

[37] L. Cao, *Deposition of size-selected nanoclusters*. PhD thesis, University of Birmingham, Sept. 2015.

[38] W. Terry, *Cluster Production in the Matrix Assembly Cluster Source*. PhD thesis, University of Birmingham, Oct. 2016.

[39] R. E. Palmer, L. Cao, and F. Yin, “Note: Proof of principle of a new type of cluster beam source with potential for scale-up,” *Review of Scientific Instruments*, vol. 87, p. 046103, Apr. 2016.

[40] T. Irawan, D. Boecker, F. Ghaleh, C. Yin, B. V. Issendorff, and H. Hövel, “Metal clusters on rare gas layers – growth and spectroscopy,” *Appl. Phys. A*, vol. 82, pp. 81–86, Jan. 2006.

[41] I. Rabin, W. Schulze, and G. Ertl, “Light emission during the agglomeration of silver clusters in noble gas matrices,” *The Journal of Chemical Physics*, vol. 108, pp. 5137–5142, Mar. 1998.

[42] H. M. Urbassek and K. T. Waldeer, “Spikes in condensed rare gases induced by keV-atom bombardment,” *Phys. Rev. Lett.*, vol. 67, pp. 105–108, July 1991.

[43] T. Tachibana, K. Fukai, T. Koizumi, and T. Hirayama, “Desorption of cluster ions from solid Ne by low-energy ion impact,” *J. Phys.: Condens. Matter*, vol. 22, no. 47, p. 475002, 2010.

[44] V. Balaji, D. E. David, T. F. Magnera, J. Michl, and H. M. Urbassek, “Sputtering yields of condensed rare gases,” *Nuclear Instruments and Methods in Physics Research Section B: Beam Interactions with Materials and Atoms*, vol. 46, pp. 435–440, Feb. 1990.

[45] J. W. Christiansen, D. D. Carpini, and I. S. T. Tsong, “Sputtering of ices by keV ions,” *Nuclear Instruments and Methods in Physics Research Section B: Beam Interactions with Materials and Atoms*, vol. 15, pp. 218–221, Apr. 1986.

[46] J. E. Mayer, *Statistical mechanics / Joseph Edward Mayer and Maria Goeppert Mayer.* New York ; London: JWiley & Sons, inc : Chapman & Hall,, 1940.

[47] D. G. Henshaw, “Atomic Distribution in Liquid and Solid Neon and Solid Argon by Neutron Diffraction,” *Phys. Rev.*, vol. 111, pp. 1470–1475, Sept. 1958.

[48] A. E. Curzon, “A comment on the lattice parameter of solid carbon dioxide at -190°C,” *Physica*, vol. 59, p. 733, June 1972.

[49] G. Sauerbrey, “Verwendung von Schwingquarzen zur Wägung dünner Schichten und zur Mikrowägung,” *Z. Physik*, vol. 155, no. 2, pp. 206–222.

[50] D. Reynolds and B. Vollmer, “STM-1 Manual from Sycon Instruments, Inc.,” June 2003.

[51] S. J. Pennycook, M. Varela, C. J. D. Hetherington, and A. I. Kirkland, “Materials Advances through Aberration-Corrected Electron Microscopy,” *MRS Bulletin*, vol. 31, pp. 36–43, Jan. 2006.

[52] D. B. Williams and C. B. Carter, *Transmission electron microscopy: A Textbook for Materials Science*. Springer, 2009.

[53] Z. W. Wang and R. E. Palmer, “Intensity calibration and atomic imaging of size-selected Au and Pd clusters in aberration-corrected HAADF-STEM,” *J. Phys.: Conf. Ser.*, vol. 371, no. 1, p. 012010, 2012.

[54] H. Eugene, *Optics*. Addison-Wesley, 4th edition ed., 2002.

[55] H. Fujiwara, *Spectroscopic Ellipsometry: Principles and Applications*. Wiley, 2003.

[56] J. D. Jackson, *Classical electrodynamics*. New York ; London : John Wiley, 1962.

[57] W. He, *Ultrafast Dynamics of Photoexcited Carriers in Semiconducting Nano Materials*. PhD thesis, University of Birmingham, Birmingham, 2015.

[58] J. C. M. Garnett, "XII. Colours in metal glasses and in metallic films," *Phil. Trans. R. Soc. Lond. A*, vol. 203, pp. 385–420, Jan. 1904.

[59] C. A. Foss, G. L. Hornyak, J. A. Stockert, and C. R. Martin, "Template-Synthesized Nanoscopic Gold Particles: Optical Spectra and the Effects of Particle Size and Shape," *J. Phys. Chem.*, vol. 98, pp. 2963–2971, Mar. 1994.

[60] A. Sihvola, *Electromagnetic Mixing Formulas and Applications*. IET Digital Library, Jan. 1999.

[61] A. Othonos, "Probing ultrafast carrier and phonon dynamics in semiconductors," *Journal of Applied Physics*, vol. 83, pp. 1789–1830, Feb. 1998.

[62] S. K. Sundaram and E. Mazur, "Inducing and probing non-thermal transitions in semiconductors using femtosecond laser pulses," *Nature Materials; London*, vol. 1, pp. 217–24, Dec. 2002.

[63] J. Singh, *Electronic and Optoelectronic Properties of Semiconductor Structures*. Cambridge University Press, Mar. 2007. Google-Books-ID: RcdljTlEv6IC.

[64] A. M. Fox, *Optical Properties of Solids*. Oxford University Press, 2001.

[65] J. M. Ziman, *Principles of the Theory of Solids*. Cambridge University Press, Nov. 1979.

[66] C. Kittel, *Introduction to Solid State Physics*. Wiley, Nov. 2004. Google-Books-ID: kym4QgAACAAJ.

[67] C. V. Shank, R. Yen, and C. Hirlimann, "Time-Resolved Reflectivity Measurements of Femtosecond-Optical-Pulse-Induced Phase Transitions in Silicon," *Phys. Rev. Lett.*, vol. 50, pp. 454–457, Feb. 1983.

[68] K. Sokolowski-Tinten and D. von der Linde, "Generation of dense electron-hole plasmas in silicon," *Phys. Rev. B*, vol. 61, pp. 2643–2650, Jan. 2000.

[69] J. Shah, R. F. Leheny, and C. Lin, "Dynamic Burstein shift in GaAs," *Solid State Communications*, vol. 18, pp. 1035–1037, Jan. 1976.

[70] A. J. Sabbah and D. M. Riffe, "Femtosecond pump-probe reflectivity study of silicon carrier dynamics," *Phys. Rev. B*, vol. 66, p. 165217, Oct. 2002.

[71] R. W. Boyd, *Nonlinear Optics*. Elsevier, May 2008. Google-Books-ID: uoRUi1Yb7ooC.

[72] G. Amato, C. Delerue, and H. J. VonBardeleben, *Structural and Optical Properties of Porous Silicon Nanostructures*. CRC Press, Feb. 1998. Google-Books-ID: BT3lwOtnSfoC.

[73] X. Liu, Q. Guo, and J. Qiu, "Emerging Low-Dimensional Materials for Nonlinear Optics and Ultrafast Photonics," *Advanced Materials*, vol. 29, p. 1605886, Apr. 2017.

[74] A. D. Neira, N. Olivier, M. E. Nasir, W. Dickson, G. A. Wurtz, and A. V. Zayats, "Eliminating material constraints for nonlinearity with plasmonic metamaterials," *Nature Communications*, vol. 6, p. 7757, July 2015.

[75] W. S. Martins, H. L. D. de S. Cavalcante, T. Passerat de Silans, M. Oriá, and M. Chevrollier, "Two-beam nonlinear Kerr effect to stabilize laser frequency with sub-Doppler resolution," *Applied Optics*, vol. 51, p. 5080, July 2012.

[76] J. Heald and R. F. Brown, "Measurements of condensation and evaporation of carbon dioxide, nitrogen, and argon at cryogenic temperatures using a molecular beam," tech. rep., Sept. 1968.

[77] L. Cao, "Matrix Assembly Cluster Source," mid Course Assessment, 2012.

[78] D. M. Wells, R. Ferrando, G. Rossi, and R. E. Palmer, "Metastability of the atomic structures of size-selected gold nanoparticles," *Nanoscale*, 2015.

[79] N. Young, Z. Li, Y. Chen, S. Palomba, M. Di Vece, and R. Palmer, "Weighing Supported Nanoparticles: Size-Selected Clusters as Mass Standards in Nanometrology," *Physical Review Letters*, vol. 101, Dec. 2008.

[80] Z. Y. Li, N. P. Young, M. Di Vece, S. Palomba, R. E. Palmer, A. L. Bleloch, B. C. Curley, R. L. Johnston, J. Jiang, and J. Yuan, "Three-dimensional atomic-scale structure of size-selected gold nanoclusters," *Nature*, vol. 451, pp. 46–48, Jan. 2008.

[81] V. N. Popok, I. Barke, E. E. B. Campbell, and K.-H. Meiwes-Broer, "Cluster–surface interaction: From soft landing to implantation," *Surface Science Reports*, vol. 66, pp. 347–377, Oct. 2011.

[82] M. Schmidt, P. Cahuzac, C. Bréchignac, and H.-P. Cheng, "The stability of free and oxidized silver clusters," *The Journal of Chemical Physics*, vol. 118, pp. 10956–10962, June 2003.

[83] J. Aitchison and J. A. C. Brown, *The lognormal distribution*. Cambridge University Press, 1957. Google-Books-ID: Kus8AAAAIAAJ.

[84] C. G. Granqvist and R. A. Buhrman, "Ultrafine metal particles," *Journal of Applied Physics*, vol. 47, pp. 2200–2219, May 1976.

[85] I. Pócsik, "Lognormal distribution as the natural statistics of cluster systems," *Z Phys D - Atoms, Molecules and Clusters*, vol. 20, pp. 395–397, Mar. 1991.

[86] C.-R. Wang, R.-B. Huang, Z.-Y. Liu, and L.-S. Zheng, "Lognormal size distributions of elemental clusters," *Chemical Physics Letters*, vol. 227, pp. 103–108, Sept. 1994.

[87] R. Espiau de Lamaëstre and H. Bernas, “Significance of lognormal nanocrystal size distributions,” *Phys. Rev. B*, vol. 73, p. 125317, Mar. 2006.

[88] S. Redner, “Random multiplicative processes: An elementary tutorial,” vol. 58, pp. 267–273, Mar. 1990.

[89] M. Villarica, M. J. Casey, J. Goodisman, and J. Chaiken, “Application of fractals and kinetic equations to cluster formation,” *The Journal of Chemical Physics*, vol. 98, pp. 4610–4625, Mar. 1993.

[90] Q. Ran, R. W. Schmude, K. A. Gingerich, D. W. Wilhite, and J. E. Kingcade, “Dissociation energy and enthalpy of formation of gaseous silver dimer,” *J. Phys. Chem.*, vol. 97, pp. 8535–8540, Aug. 1993.

[91] C. J. Evans, T. G. Wright, and A. M. Gardner, “Geometries and Bond Energies of the He-MX, Ne-MX, and Ar-MX (M = Cu, Ag, Au; X = F, Cl) Complexes,” *J. Phys. Chem. A*, vol. 114, pp. 4446–4454, Apr. 2010.

[92] A. Shayeghi, R. L. Johnston, D. M. Rayner, R. Schäfer, and A. Fielicke, “The Nature of Bonding between Argon and Mixed Gold–Silver Trimers,” *Angew. Chem. Int. Ed.*, vol. 54, pp. 10675–10680, Sept. 2015.

[93] A. W. Czanderna and J. R. Biegen, “Activation Energy for the Desorption of Carbon Dioxide from Oxygen-Covered Silver,” *Journal of Vacuum Science & Technology*, vol. 8, pp. 594–598, July 1971.

[94] C. E. Bryson, V. Cazcarra, and L. L. Levenson, “Sublimation rates and vapor pressures of water, carbon dioxide, nitrous oxide, and xenon,” *J. Chem. Eng. Data*, vol. 19, pp. 107–110, Apr. 1974.

[95] A. G. M. Ferreira and L. Q. Lobo, “The sublimation of argon, krypton, and xenon,” *The Journal of Chemical Thermodynamics*, vol. 40, pp. 1621–1626, Dec. 2008.

[96] V. F. Lotrich and K. Szalewicz, “Three-Body Contribution to Binding Energy of Solid Argon and Analysis of Crystal Structure,” *Phys. Rev. Lett.*, vol. 79, pp. 1301–1304, Aug. 1997.

[97] W. L. Brown, W. M. Augustyniak, E. Simmons, K. J. Marcantonio, L. J. Lanzerotti, R. E. Johnson, J. W. Boring, C. T. Reimann, G. Foti, and V. Pirronello, “Erosion and molecule formation in condensed gas films by electronic energy loss of fast ions,” *Nuclear Instruments and Methods in Physics Research*, vol. 198, pp. 1–8, July 1982.

[98] V. Habibpour, M. Y. Song, Z. W. Wang, J. Cookson, C. M. Brown, P. T. Bishop, and R. E. Palmer, “Novel Powder-Supported Size-Selected Clusters for Heterogeneous Catalysis under Realistic Reaction Conditions,” *J. Phys. Chem. C*, vol. 116, pp. 26295–26299, Dec. 2012.

[99] R. M. Nielsen, S. Murphy, C. Strebel, M. Johansson, J. H. Nielsen, and I. Chorkendorff, “A comparative STM study of Ru nanoparticles deposited on HOPG by mass-selected gas aggregation versus thermal evaporation,” *Surface Science*, vol. 603, pp. 3420–3430, Dec. 2009.

[100] F. Yin, S. Lee, A. Abdela, S. Vajda, and R. E. Palmer, “Communication: Suppression of sintering of size-selected Pd clusters under realistic reaction conditions for catalysis,” *The Journal of Chemical Physics*, vol. 134, p. 141101, Apr. 2011.

[101] T. Mori and T. Hegmann, “Determining the composition of gold nanoparticles: a compilation of shapes, sizes, and calculations using geometric considerations,” *J Nanopart Res*, vol. 18, p. 295, Oct. 2016.

[102] I. M. Goldby, L. Kuipers, B. von Issendorff, and R. E. Palmer, “Diffusion and aggregation of size-selected silver clusters on a graphite surface,” *Appl. Phys. Lett.*, vol. 69, pp. 2819–2821, Nov. 1996.

[103] D. M. Foster, *Production and characterisation by scanning transmission electron microscopy of size-selected noble metal nanoclusters*. PhD thesis, University of Birmingham, Dec. 2017.

[104] K.-J. Hu, S. R. Plant, P. R. Ellis, C. M. Brown, P. T. Bishop, and R. E. Palmer, “Atomic Resolution Observation of a Size-Dependent Change in the Ripening Modes of Mass-Selected Au Nanoclusters Involved in CO Oxidation,” *J. Am. Chem. Soc.*, vol. 137, pp. 15161–15168, Dec. 2015.

[105] L. T. Canham, “Silicon quantum wire array fabrication by electrochemical and chemical dissolution of wafers,” *Appl. Phys. Lett.*, vol. 57, pp. 1046–1048, Sept. 1990.

[106] L. Canham, ed., *Handbook of Porous Silicon*. Springer International Publishing, 2014.

[107] S. Strehlke, S. Bastide, and C. Lévy-Clément, “Optimization of porous silicon reflectance for silicon photovoltaic cells,” *Solar Energy Materials and Solar Cells*, vol. 58, pp. 399–409, Aug. 1999.

[108] L. T. Canham, “Bioactive silicon structure fabrication through nanoetching techniques,” *Advanced Materials*, vol. 7, pp. 1033–1037, Dec. 1995.

[109] V. S.-Y. Lin, K. Motesharei, K.-P. S. Dancil, M. J. Sailor, and M. R. Ghadiri, “A Porous Silicon-Based Optical Interferometric Biosensor,” *Science*, vol. 278, pp. 840–843, Oct. 1997.

[110] S. J. Park, A. Zakar, V. L. Zerova, D. Chekulaev, L. T. Canham, and A. Kaplan, “All-optical modulation in Mid-Wavelength Infrared using porous Si membranes,” *Scientific Reports*, vol. 6, p. 30211, July 2016.

[111] V. R. Almeida, C. A. Barrios, R. R. Panepucci, and M. Lipson, “All-optical control of light on a silicon chip,” *Nature*, vol. 431, pp. 1081–1084, Oct. 2004.

[112] D. M. Beggs, T. P. White, L. O’Faolain, and T. F. Krauss, “Ultracompact and low-power optical switch based on silicon photonic crystals,” *Opt. Lett., OL*, vol. 33, pp. 147–149, Jan. 2008.

[113] G. T. Reed, G. Mashanovich, F. Y. Gardes, and D. J. Thomson, “Silicon optical modulators,” *Nature Photonics*, vol. 4, pp. 518–526, Aug. 2010.

[114] G. T. Reed, "Device physics: The optical age of silicon," *Nature*, vol. 427, pp. 595–596, Feb. 2004.

[115] L. Fekete, J. Y. Hlinka, F. Kadlec, P. Kužel, and P. Mounaix, "Active optical control of the terahertz reflectivity of high-resistivity semiconductors," *Opt. Lett., OL*, vol. 30, pp. 1992–1994, Aug. 2005.

[116] M. W. Geis, S. J. Spector, R. C. Williamson, and T. M. Lyszczarz, "Submicrosecond submilliwatt silicon-on-insulator thermooptic switch," *IEEE Photonics Technology Letters*, vol. 16, pp. 2514–2516, Nov. 2004.

[117] R. W. Boyd, R. J. Gehr, G. L. Fischer, and J. E. Sipe, "Nonlinear optical properties of nanocomposite materials," *Pure and Applied Optics: Journal of the European Optical Society Part A*, vol. 5, pp. 505–512, Sept. 1996.

[118] J. E. Sipe and R. W. Boyd, "Nonlinear susceptibility of composite optical materials in the Maxwell Garnett model," *Physical Review A*, vol. 46, pp. 1614–1629, Aug. 1992.

[119] R. J. Gehr, G. L. Fischer, and R. W. Boyd, "Nonlinear-optical response of porous-glass-based composite materials," *J. Opt. Soc. Am. B, JOSAB*, vol. 14, pp. 2310–2314, Sept. 1997.

[120] E. J. Heilweil and R. M. Hochstrasser, "Nonlinear spectroscopy and picosecond transient grating study of colloidal gold," *The Journal of Chemical Physics*, vol. 82, pp. 4762–4770, June 1985.

[121] C. A. Foss, G. L. Hornyak, J. A. Stockert, and C. R. Martin, "Optical properties of composite membranes containing arrays of nanoscopic gold cylinders," *J. Phys. Chem.*, vol. 96, pp. 7497–7499, Sept. 1992.

[122] G. L. Hornyak, C. J. Patrissi, and C. R. Martin, "Fabrication, Characterization, and Optical Properties of Gold Nanoparticle/Porous Alumina Composites: The Nonscattering Maxwell-Garnett Limit," *J. Phys. Chem. B*, vol. 101, pp. 1548–1555, Feb. 1997.

[123] S. Link and M. A. El-Sayed, "Spectral Properties and Relaxation Dynamics of Surface Plasmon Electronic Oscillations in Gold and Silver Nanodots and Nanorods," *J. Phys. Chem. B*, vol. 103, pp. 8410–8426, Oct. 1999.

[124] R. Atkinson, W. R. Hendren, G. A. Wurtz, W. Dickson, A. V. Zayats, P. Evans, and R. J. Pollard, "Anisotropic optical properties of arrays of gold nanorods embedded in alumina," *Phys. Rev. B*, vol. 73, p. 235402, June 2006.

[125] T. S. Ahmadi, S. L. Logunov, and M. A. El-Sayed, "Picosecond Dynamics of Colloidal Gold Nanoparticles," *J. Phys. Chem.*, vol. 100, pp. 8053–8056, Jan. 1996.

[126] H. Inouye, K. Tanaka, I. Tanahashi, and K. Hirao, "Ultrafast dynamics of nonequilibrium electrons in a gold nanoparticle system," *Phys. Rev. B*, vol. 57, pp. 11334–11340, May 1998.

[127] B. A. Smith, J. Z. Zhang, U. Giebel, and G. Schmid, "Direct probe of size-dependent electronic relaxation in single-sized Au and nearly monodisperse Pt colloidal nanoparticles," *Chemical Physics Letters*, vol. 270, pp. 139–144, May 1997.

[128] F. Z. Henari and A. A. Dakhel, “Linear and nonlinear optical properties of gold nanoparticle-Eu oxide composite thin films,” *Journal of Applied Physics*, vol. 104, p. 033110, Aug. 2008.

[129] R. Philip, P. Chantharasupawong, H. Qian, R. Jin, and J. Thomas, “Evolution of Nonlinear Optical Properties: From Gold Atomic Clusters to Plasmonic Nanocrystals,” *Nano Lett.*, vol. 12, pp. 4661–4667, Sept. 2012.

[130] A. G. Cullis, L. T. Canham, and P. D. J. Calcott, “The structural and luminescence properties of porous silicon,” *Journal of Applied Physics*, vol. 82, pp. 909–965, Aug. 1997.

[131] M. V. Wolkin, J. Jorne, P. M. Fauchet, G. Allan, and C. Delerue, “Electronic States and Luminescence in Porous Silicon Quantum Dots: The Role of Oxygen,” *Physical Review Letters*, vol. 82, pp. 197–200, Jan. 1999.

[132] C. Pickering, M. I. J. Beale, D. J. Robbins, P. J. Pearson, and R. Greef, “Optical properties of porous silicon films,” *Thin Solid Films*, vol. 125, pp. 157–163, Mar. 1985.

[133] A. Wolf, B. Terheiden, and R. Brendel, “Light scattering and diffuse light propagation in sintered porous silicon,” *Journal of Applied Physics*, vol. 104, p. 033106, Aug. 2008.

[134] A. Zakar, R. Wu, D. Chekulaev, V. Zerova, W. He, L. Canham, and A. Kaplan, “Carrier dynamics and surface vibration-assisted Auger recombination in porous silicon,” *Phys. Rev. B*, vol. 97, p. 155203, Apr. 2018.

[135] F. Z. Henari, K. Morgenstern, W. J. Blau, V. A. Karavanskii, and V. S. Dneprovskii, “Third-order optical nonlinearity and all-optical switching in porous silicon,” *Appl. Phys. Lett.*, vol. 67, pp. 323–325, July 1995.

[136] A. D. Bristow, N. Rotenberg, and H. M. van Driel, “Two-photon absorption and Kerr coefficients of silicon for 850–2200nm,” *Applied Physics Letters*, vol. 90, p. 191104, May 2007.

[137] R. J. Suess, M. M. Jadidi, K. Kim, and T. E. Murphy, “Characterization of optical nonlinearities in nanoporous silicon waveguides via pump-probe heterodyning technique,” *Opt. Express, OE*, vol. 22, pp. 17466–17477, July 2014.

[138] P. Apiratikul, A. M. Rossi, and T. E. Murphy, “Nonlinearities in porous silicon optical waveguides at 1550 nm,” *Opt. Express, OE*, vol. 17, pp. 3396–3406, Mar. 2009.

[139] A. S. Lenshin, V. M. Kashkarov, E. P. Domashevskaya, P. V. Seredin, S. V. Ryabtsev, A. N. Bel’tyukov, and F. Z. Gil’mutdinov, “Composition of nanocomposites based on thin layers of tin on porous silicon formed by magnetron sputtering,” *Physica B: Condensed Matter*, vol. 504, pp. 1–8, Jan. 2017.

[140] M. L. Chourou, K. Fukami, T. Sakka, and Y. H. Ogata, “Gold electrodeposition into porous silicon: Comparison between meso- and macroporous silicon,” *physica status solidi c*, vol. 8, pp. 1783–1786, June 2011.

[141] C. Fang, E. Foca, S. Xu, J. Carstensen, and H. Föll, "Deep Silicon Macropores Filled with Copper by Electrodeposition," *J. Electrochem. Soc.*, vol. 154, pp. D45–D49, Jan. 2007.

[142] E. Nativ-Roth, K. Rechav, and Z. Porat, "Deposition of gold and silver on porous silicon and inside the pores," *Thin Solid Films*, vol. 603, pp. 88–96, Mar. 2016.

[143] S. Babar and J. H. Weaver, "Optical constants of Cu, Ag, and Au revisited," *Appl. Opt., AO*, vol. 54, pp. 477–481, Jan. 2015.

[144] R. Ruppin, "Validity Range of the Maxwell-Garnett Theory," *Physica Status Solidi (b)*, vol. 87, pp. 619–624, June 1978.

[145] A. A. Bugayev, A. Khakhaev, and A. S. Zubrilov, "Picosecond time-resolved reflectivity of porous silicon," *Optics Communications*, vol. 106, pp. 65–68, Mar. 1994.

[146] P. B. Johnson and R. W. Christy, "Optical Constants of the Noble Metals," *Phys. Rev. B*, vol. 6, pp. 4370–4379, Dec. 1972.

[147] L. J. Mendoza Herrera, D. M. Arboleda, D. C. Schinca, and L. B. Scaffardi, "Determination of plasma frequency, damping constant, and size distribution from the complex dielectric function of noble metal nanoparticles," *Journal of Applied Physics*, vol. 116, p. 233105, Dec. 2014.

[148] T. W. Roger, W. He, I. V. Yurkevich, and A. Kaplan, "Enhanced carrier-carrier interaction in optically pumped hydrogenated nanocrystalline silicon," *Appl. Phys. Lett.*, vol. 101, p. 141904, Oct. 2012.

[149] M. V. Fischetti, "Monte Carlo simulation of transport in technologically significant semiconductors of the diamond and zinc-blende structures. I. Homogeneous transport," *IEEE Transactions on Electron Devices*, vol. 38, pp. 634–649, Mar. 1991.

Appendix A

Maxwell's equations

The first law (Gauss's law) states that the electric flux[1] leaving a closed surface is proportional to the charge ρ contained within the surface:

$$\vec{\nabla} \cdot \vec{E} = \frac{\rho}{\varepsilon_0} \tag{A.1}$$

The second law (Gauss's law for magnetism) stipulates that the magnetic flux[2] $\vec{B}$ leaving the north pole of a magnetic source must re-enter a closed surface surrounding it to reach its south pole, i.e. monopoles don't exist, an therefore:

$$\vec{\nabla} \cdot \vec{B} = 0 \tag{A.2}$$

In the third law (Faraday's law), one understands that a time-varying magnetic flux induces a spatially-varying electric field and vice-versa:

$$\vec{\nabla} \wedge \vec{E} = -\frac{\partial \vec{B}}{\partial t} \tag{A.3}$$

---

[1] The electric flux is noted $\vec{D}$ and equals to $\varepsilon_0 \vec{E}$ in vacuum with ε_0 the permittivity of free space.

[2] The magnetic flux is noted $\vec{B}$ and equals to $\mu_0 \vec{H}$ in vacuum, where $\vec{H}$ is the magnetic field and μ_0 is called the permeability of free space.

The fourth equation is a modification of Ampere's law by Maxwell as he was looking for a complementary relation to the third law. Both a current $\vec{J}$ passing through a wire and a time-varying electric field (such as the one existing inside a charging capacitor), induce a magnetic field circling around them:

$$\vec{\nabla} \wedge \vec{B} = \mu_0 \left(\vec{J} + \varepsilon_0 \frac{\partial \vec{E}}{\partial t} \right) \tag{A.4}$$

These four equations are called Maxwell's equations and can be re-written in the case of a region free from charges and currents (i.e. $\rho = 0$ and $\vec{J} = 0$) as:

$$\begin{cases} \vec{\nabla} \cdot \vec{E} = 0 & \vec{\nabla} \wedge \vec{E} \quad = -\dfrac{\partial \vec{B}}{\partial t} \\ \vec{\nabla} \cdot \vec{B} = 0 & \vec{\nabla} \wedge \vec{B} \quad = \varepsilon_0 \mu_0 \dfrac{\partial \vec{E}}{\partial t} \end{cases} \tag{A.5}$$

Taking the curl of the third and fourth equations and using the curl of curl identity[3] leads to :

$$\begin{cases} -\vec{\nabla}^2 \cdot \vec{E} = \vec{\nabla} \wedge \left(\dfrac{\partial \vec{B}}{\partial t} \right) \\ -\vec{\nabla}^2 \cdot \vec{B} = \vec{\nabla} \wedge \left(\varepsilon_0 \mu_0 \dfrac{\partial \vec{E}}{\partial t} \right) \end{cases} \Rightarrow \begin{cases} \vec{\nabla}^2 \cdot \vec{E} = \varepsilon_0 \mu_0 \dfrac{\partial^2 \vec{E}}{\partial t^2} \\ \vec{\nabla}^2 \cdot \vec{B} = \varepsilon_0 \mu_0 \dfrac{\partial^2 \vec{B}}{\partial t^2} \end{cases} \tag{A.6}$$

On the left part of the above set of equations, we note that a change in electric field induces a change in magnetic, which in turn generates a change in electric field. A cycle is created. The right part of the above set of equations shows that both the electric and magnetic fields behave as coupled space and time dependent fields. When compared to propagating waves[4], the corresponding propagation speed equals to $c = \frac{1}{\sqrt{\varepsilon_0 \mu_0}}$ in vacuum.

---

[3] $\vec{\nabla} \wedge (\vec{\nabla} \wedge \vec{a}) = \vec{\nabla} \cdot (\vec{\nabla} \cdot \vec{a}) - \vec{\nabla}^2 \cdot \vec{a}$

[4] $\vec{\nabla}^2 \cdot \vec{\Psi} = \frac{1}{v^2} \frac{\partial^2 \vec{\Psi}}{\partial t^2}$

Appendix B

Boundary conditions

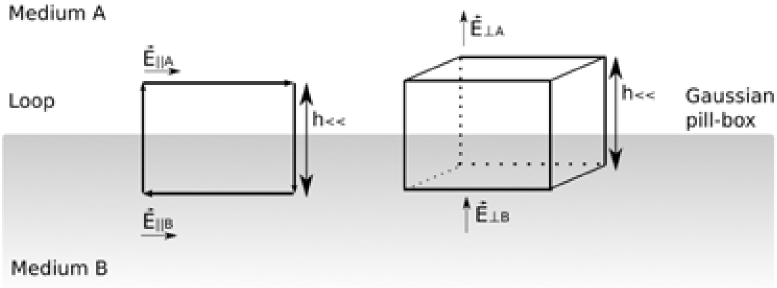

Fig. B.1 Here are represented a closed loop and a Gaussian pill-box passing through the interface between two media *A* and *B*. This diagram is useful to visualise the boundaries conditions detailed below.)

When passing through an interface, the electric field and the magnetic field must respect certain conditions imposed by Maxwell's equations (see section A). The conditions satisfied at the interface between two media *A* and *B* as seen in the figure B.1 for the electric field are given by the first, third and fourth Maxwell's equations. Gauss' law says that the electric flux passing through a surface is proportional to the total charge it encloses. Let's consider a Gaussian pill-box surrounding the interface with a very small height such as the electric flux passing through the surfaces of the volume has only a perpendicular component. The electric flux, is noted $\vec{D}$ and equals to $\varepsilon\vec{E}$ with ε the permittivity of the material. We have:

$$\oint_S \vec{D} ds = \rho$$
$$\Leftrightarrow D_{\perp A} - D_{\perp B} = \rho$$

If no accumulation of charge is present on the surface, $\rho = 0$ and:

$$\oint_S \vec{D} ds = 0$$
$$\Leftrightarrow \varepsilon_A E_{\perp A} = \varepsilon_B E_{\perp B} \quad (Condition I)$$

In the absence of a time-varying magnetic flux, the third law describing the integration of the electric field over a closed loop is zero such as:

$$\oint_C \vec{E} d\vec{l} = 0$$
$$\Leftrightarrow (E_{\parallel A} - E_{\parallel b}) \cdot l = 0$$
$$\Leftrightarrow E_{\parallel A} = E_{\parallel b} \quad (Condition II)$$

The condition *II* implies that there is no discontinuity of the parallel component of the electric field across the interface. Using Ampere-Maxwell law, one can easily demonstrate, as previously done for condition *II*, that in the absence of an electric current and a time-varying electric field, the parallel component of the magnetic field is continuous across the interface, given:

$$H_{\parallel A} = H_{\parallel b} \quad (Condition III)$$